

**Deterministic prediction of waves and wave induced vessel motions
Future telling by using nautical radar as a remote wave sensor**

Naaijen, Peter

DOI

[10.4233/uuid:49bf7c26-e260-448a-b94a-5fcb038fa602](https://doi.org/10.4233/uuid:49bf7c26-e260-448a-b94a-5fcb038fa602)

Publication date

2017

Document Version

Final published version

Citation (APA)

Naaijen, P. (2017). *Deterministic prediction of waves and wave induced vessel motions: Future telling by using nautical radar as a remote wave sensor*. [Dissertation (TU Delft), Delft University of Technology]. <https://doi.org/10.4233/uuid:49bf7c26-e260-448a-b94a-5fcb038fa602>

Important note

To cite this publication, please use the final published version (if applicable).
Please check the document version above.

Copyright

Other than for strictly personal use, it is not permitted to download, forward or distribute the text or part of it, without the consent of the author(s) and/or copyright holder(s), unless the work is under an open content license such as Creative Commons.

Takedown policy

Please contact us and provide details if you believe this document breaches copyrights.
We will remove access to the work immediately and investigate your claim.

DETERMINISTIC PREDICTION OF WAVES AND WAVE INDUCED VESSEL MOTIONS

**FUTURE TELLING BY USING NAUTICAL RADAR AS A REMOTE
WAVE SENSOR**

DETERMINISTIC PREDICTION OF WAVES AND WAVE INDUCED VESSEL MOTIONS

**FUTURE TELLING BY USING NAUTICAL RADAR AS A REMOTE
WAVE SENSOR**



Proefschrift

ter verkrijging van de graad van doctor
aan de Technische Universiteit Delft,
op gezag van de Rector Magnificus prof. ir. K. C. A. M. Luyben,
voorzitter van het College voor Promoties,
in het openbaar te verdedigen op vrijdag 6 Oktober 2017 om 10:00 uur

door

Peter NAAIJEN

scheepsbouwkundig ingenieur
geboren te Giessen, Nederland.

This dissertation has been approved by the promotor:

Prof. dr. R.H.M. Huijsmans
Prof. dr. E.W.C. Van Groesen

Composition of the doctoral committee:

Rector Magnificus,	voorzitter
Prof. dr. R.H.M. Huijsmans,	Technische Universiteit Delft, promotor
Prof. dr. E.W.C. Van Groesen,	Technische Universiteit Twente, promotor

Independent members:

Prof. dr. K. Trulsen,	University of Oslo
Prof. dr. P. Ferrant,	Ecole Centrale de Nantes
Prof. dr. A.J.H.M. Reniers,	Technische Universiteit Delft
Dr. G. Klopman,	Witteveen & Bos
Prof. J.J. Hopman,	Technische Universiteit Delft, reservelid

This research has been carried out within the research project 'PROMISED Operations' (PRediction Of wave induced Motions and forces In Ship, offshorE and Dredging Operations), funded by 'Agentschap NL', a department of the Dutch Ministry of Economic Affairs, Agriculture and Innovation and co-funded by Delft University of Technology, University of Twente, Maritime Research Institute Netherlands, Ocean Waves GMBH, Allseas, Heerema Marine Contractors and IHC.

Keywords: wave prediction, decision support, wave radar, deterministic ship motion prediction

Cover illustration: Jort van der Jagt & Peter Naaijen.

Copyright © 2017 by P. Naaijen

ISBN 978-94-6233-754-1

CONTENTS

Summary	ix
Samenvatting	xi
1 Introduction	1
1.1 Operability: statistical vs deterministic approach	2
1.2 Research into Deterministic Prediction of Ship Motions Using Remote Wave Sensing	3
1.3 Objective of the research	6
1.4 Outline of the Thesis	7
2 Limits to the extent of the spatio-temporal domain for deterministic wave prediction	9
2.1 Summary	10
2.2 Introduction	11
2.3 Approach	12
2.4 A linear model for propagation of long-crested waves.	13
2.5 Predictability	14
2.5.1 Predictable zone	14
2.5.2 Method of stationary phase	16
2.6 Simulations	19
2.6.1 Procedure	19
2.6.2 Simulations using synthetic waves data	20
2.6.3 Simulations using experimental wave data.	21
2.7 Prediction horizon and optimal prediction distance in practical application of deterministic wave prediction	27
2.8 Conclusion	28
2.9 Acknowledgments	29
3 Dynamic Averaging and Evolution	31
3.1 summary	32
3.2 Introduction	33
3.2.1 A brief history of wave observation and prediction using non-coherent nautical radar	33
3.2.2 Wave model initialization using inaccurate observation data: data assimilation	35
3.3 Approach	36
3.3.1 Observation data and domain	36
3.3.2 Technical approach	37

3.4	Synthetic data.	38
3.4.1	Synthetic surface elevation.	38
3.4.2	Synthetic Images.	38
3.5	Dynamic Averaging-Evolution Scenario.	41
3.5.1	Spatial reconstruction from synthetic images	41
3.5.2	Evolution of a single image.	41
3.5.3	Updates from dynamic averaging	43
3.5.4	Evolution, prediction and predictability	44
3.6	3DFFT	48
3.7	Case studies.	51
3.7.1	Parameters of the studied cases	51
3.7.2	Simulation Results	52
3.7.3	Prediction	57
3.8	Discussion of results	58
3.8.1	Reconstruction method	58
3.8.2	Predictability.	60
3.8.3	DAES vs 3D FFT	61
3.8.4	Scaling.	61
3.8.5	MED and bimodal sea state	62
3.9	Conclusions and recommendations	62
4	Modeling and inversion of Normalized Radar Cross Section	63
4.1	Summary	64
4.2	Introduction	65
4.3	Modeling imaging of surface waves by non coherent radar	67
4.4	Inversion methods for radar clutter	70
4.4.1	detection of directional wave spectrum and current	71
4.4.2	2D FFT preceded by beam-wise spectral integration ('2DFFT')	73
4.4.3	Least squares approach	74
4.5	Simulations with synthetic data.	76
4.5.1	Wave conditions and synthetic radar data	76
4.5.2	Simulation settings	77
4.5.3	Results and discussion deterministic prediction	79
4.5.4	Results and discussion wave spectrum estimation	88
4.6	Conclusions and recommendations	93
5	Application and validation with field data	95
5.1	Summary	96
5.2	Introduction	97
5.3	Vessel and trial location.	98
5.4	Used sensor data	99
5.4.1	Radar data	99
5.4.2	Motion sensor data	104
5.5	Simulations	106
5.5.1	Procedure and settings of spectrum and current detection.	106
5.5.2	Procedure and settings LSQ	107

5.6	Results and discussion	109
5.6.1	15 minutes spectra and scaling factors	109
5.6.2	Nowcast accuracy	110
5.6.3	Prediction accuracy	113
5.7	Conclusions.	115
6	Conclusions and recommendations	117
	References	121
A	Appendix	127
B	Appendix	131
C	Appendix	133
D	Appendix	135
E	Appendix	137
F	Appendix	141
G	Appendix	143
H	Appendix	145
I	Appendix	147
J	Appendix	151
K	Appendix	155
L	Appendix	159
M	Appendix	163
	Curriculum Vitae	167

SUMMARY

With many operations at sea carried out by ships or other floating vessels, risks are involved because of the waves and resulting motions of the ships. Examples are the landing of helicopters on ships, transferring crew from a ship to a wind turbine, or working on the deck of an anchor handling tug. It is common practice to assess the workability of a certain operation by statistical criteria. The rationale behind such criteria is in general that the probability of some phenomenon (e.g. the vertical motion of a helicopter landing deck) exceeding a certain threshold value has to be less than a chosen acceptable level. Operability analysis usually qualify a given wave condition as workable or not workable based on such statistical criteria, assuming that no information is available about *when* critical wave induced events occur. In this thesis, the feasibility is investigated to obtain a short term, 'deterministic', i.e. time-specific prediction of the critical response: making available a short term prediction of approaching waves and vessel response real time, on-board, would give crew the opportunity to *anticipate* and chose the optimal moment to perform a critical operation. The research is motivated by two possible advantages of such a deterministic prediction:

1. It further enhances safety in conditions that were considered as workable from a statistical point of view.
2. It possibly increases workability by pointing out windows of opportunity in conditions that were considered as unworkable from a statistical point of view.

The chosen approach to obtain the mentioned deterministic prediction of waves and induced motion response, is to use the ship's navigation radar as a remote wave sensor.

The spatial domain that can be covered by a navigation radar to observe the sea surface is of course limited: both its minimum and maximum range is limited. Besides it is obvious that the wave observation will only be available in the past, and by no means in the future. Therefore, the first chapter answers the theoretical question where in the spatio-temporal domain waves can be accurately predicted, given a perfect spatio-temporal observation of the waves. An indicator is proposed that specifies predictability in space and time based on the spatio-temporal observation and based on a given wave condition. It is confirmed that the *group* velocity of the waves is governing concerning this question.

This so-called predictability indicator is considered for the 1 dimensional case in space in chapter 2 and extended to 2D in chapter 3.

Chapter 3 addresses the issue that a wave observation obtained from a navigation radar is by no means a 'perfect' observation. An approach is proposed with the aim to minimize the effect of imperfect observations by means of an assimilation procedure referred to as dynamic averaging and evolution. Using synthetic radar data, it is shown that the approach leads to an accuracy of wave predictions that is significantly

higher than the accuracy of the synthesized observation and that for the purpose of deterministic prediction it outperforms the more traditional kind of assimilation used for sea wave observation by radar, based on three-dimensional Fourier Transformation (3D FFT) techniques. The imperfection of the observation is included in the synthetic data by modelling the phenomenon known as 'shadowing': waves block the view of the radar behind them, resulting in missing data in the shadowed regions.

Chapter 4 mainly addresses the issue that the reflection of the transmitted electromagnetic pulse from the sea surface received by a radar antenna, the so-called back-scatter, is more likely to be associated with the *steepness* of the waves, rather than their *elevation*: a model is proposed to relate back-scatter to a linear representation of the wave surface. Based on this model, two alternatives are considered to find the parameters (being the component amplitudes) of this linear wave representation from the observed back-scatter. One is based on a 2D FFT approach, preceded by a beam-wise integration of the back-scatter in order to relate it to the wave steepness instead of the wave elevation. The other is based on solving the component amplitudes of the linear wave representation more directly by solving a least squares problem that minimizes the difference between the representation and the observation. Advantages of the latter approach (referred to LSQ) are that it is more suitable to deal with multi-modal sea states with counter-propagating waves and it does not involve any difficulties related to the fact that a navigation radar is a *scanning* sensor, meaning that each observation beam (and not each recorded *image*) is recorded at a distinct time instant. Its main draw-back is its high computational cost, making its real time application challenging. In order to minimize the computational burden of the LSQ approach, it involves two stages: during the first stage, the region(s) of high wave energy within the 2-dimensional wave number space is/are located by means of the much less computationally expensive 3D FFT method. This enables the selection of a limited number of wave modes whose amplitudes are to be solved using the expensive LSQ approach in the second stage.

In order to strengthen the proof of principle of the approach proposed in the preceding chapters, it is applied to actual field data, reported on in chapter 5. During an off-shore field campaign of a well-intervention vessel, both raw navigation radar data and the corresponding vessel motion data was acquired and stored. No reliable deterministic wave data was recorded during the trials which is why a comparison of predicted ship motions was aimed for. Therefore an additional analysis step is introduced aiming to obtain a prediction of the ship motion response, based on the wave prediction derived from the radar images. For this purpose, a simple linear frequency domain motion transfer function approach is applied.

Results are shown of ship motion predictions obtained by applying the developed methodology to the recorded radar data and a comparison with the actual measurement of the ship motions is presented. Correlations between these predicted and recorded ship motions reveal a very significant match. Obtained heave motion correlation based on time traces of at least 1 hour amount to 0.77 - 0.86.

The main conclusion is that the developed approach has led to a convincing proof of principle for deterministic ship motion prediction based on wave observation from navigation radar.

SAMENVATTING

Voor veel operaties op zee vormen golven en de resulterende bewegingen van de betrokken schepen een groot risico. Voorbeelden zijn het landen van helikopters op schepen, het overzetten van bemanning van een schip naar een windturbine voor onderhoud of het werk op een open dek van een ankerinstallatie schip. Het is gebruikelijk om de werkbaarheid van dergelijk operaties te baseren op statistische criteria. Het idee achter dergelijke criteria is over het algemeen dat de kans dat een bepaald verschijnsel (bijv. de verticale beweging van het helikopterdek) een gekozen kritische grens overschrijdt onder een aanvaardbaar geacht niveau is. Werkbaarheidsanalyses beoordelen een gegeven golftoestand als werkbaar of onwerkbaar, gebaseerd op dit soort statistische criteria, aannemende dat geen informatie beschikbaar zal zijn over *wanneer precies* een kritisch golfgerelateerd event zal optreden.

In dit proefschrift wordt de technische haalbaarheid onderzocht van een systeem dat real-time aan boord een 'deterministische', dwz tijdsspecifieke voorspelling van de golven en het resulterende bewegingsgedrag voor de korte termijn voorspelt en op deze manier de bemanning de gelegenheid geeft hierop te anticiperen. De motivatie voor de ontwikkeling van een dergelijk voorspellingsysteem is tweeledig:

1. Het zal de risico's verder verkleinen voor operaties waarbij die sowieso, ook vanuit traditioneel statistisch oogpunt al acceptabel zijn.
2. Het maakt het eventueel mogelijk om de werkbaarheid te vergroten door in vanuit statistisch oogpunt onwerkbare condities vooraf tijdsvensters aan te wijzen waarbinnen een operatie toch veilig uitgevoerd kan worden.

De gekozen aanpak voor het realiseren van een dergelijk voorspellingsysteem is door de scheepsnavigatieradar te gebruiken als een golfmeet sensor.

Het spatiale domein waarbinnen de navigatieradar het golfoppervlak kan waarnemen is uiteraard beperkt: er zitten grenzen aan zowel de minimale als de maximale range van de radar. Daarnaast is het evident dat een observatie alleen het verleden betreft en niet de toekomst. Derhalve is het eerste hoofdstuk gewijd aan de theoretische vraag waar in het spatio-temporale domein golven accuraat voorspeld kunnen worden, gegeven een spatio-temporale perfecte observatie van de golven. Een indicator is voorgesteld en onderzocht die de voorspelbaarheid in plaats en tijd specificeert, gebaseerd op een gegeven observatie in plaats en tijd en een gegeven golfconditie. Dit deel van het onderzoek bevestigt dat voor het beantwoorden van deze vraag de groepsnelheid van de golven leidend is, en niet hun fase snelheid.

De zogenaamde voorspelbaarheidsindicator is onderzocht voor het geval van eendimensionale golven in hoofdstuk 2 en uitgebreid naar de tweedimensionale situatie in hoofdstuk 3.

In hoofdstuk 3 wordt aandacht besteed aan het feit dat een golfobservatie door een scheepsradar nooit een perfecte waarneming zal zijn. Er wordt een assimilatiemethode voorgesteld die er op gericht is het effect van meetonauwkeurigheden te minimaliseren. Met synthetische radar data wordt aangetoond dat de methode leidt tot een voorspellingsnauwkeurigheid die aanzienlijk hoger is dan de nauwkeurigheid van de gesynthetiseerde observatie en tevens veel nauwkeuriger dan voorspellingen op basis van de meer traditionele 3D FFT aanpak. De imperfectie in de synthetische radar data is afkomstig van het modeleren van een verschijnsel wat 'shadowing' wordt genoemd: golven blokkeren het zicht van de radar op het achterliggende zee oppervlak, resulterend in missende data op die plekken.

Hoofdstuk 4 richt zich op de aanname dat de door de radar antenne ontvangen reflectie terugkaatsend van het golfoppervlak eerder gerelateerd is aan de in de kijk-richting geprojecteerde steilheid van de golven dan aan de elevatie van de golven. Een model wordt op deze aanname gebaseerd wat het ontvangen radar signaal relateert aan een lineaire representatie van de golven. Twee alternatieve methoden worden onderzocht om de parameters van de lineaire golfrepresentatie (te weten de complexe amplitudes van de harmonische golfcomponenten) op te lossen uit de gemeten radar data. De eerste maakt gebruik van twee-dimensionale Fourier transformaties (2D FFT), vooraf gegaan door een spectrale integratie van het ontvangen radar signaal per beam, ten einde het signaal te relateren aan golfsteilheid in plaats van elevatie. Het alternatief betreft een meer directe aanpak waarbij de amplitudes van de harmonische golfcomponenten gevonden worden door het oplossen van een least-squares probleem wat het verschil minimaliseert tussen de observatie en de representatie ervan. Voordelen van deze tweede aanpak (LSQ genoemd) zijn dat ze geschikter is in gecombineerde golfcondities waarbij meerdere golfsystemen deels een tegengestelde voortplantingsrichting hebben en dat op eenvoudigere wijze wordt omgegaan met het feit dat navigatieradar een scannende sensor betreft, waarbij de data per omwenteling niet op één en het zelfde moment is waargenomen, maar elke beam gerelateerd is aan zijn eigen observatie tijd. Het belangrijkste nadeel van de LSQ methode is dat ze rekenintensief is, hetgeen de real-time toepassing ervan zeer uitdagend maakt. Om de benodigde rekentijd te beperken bestaat de LSQ methode uit twee fases: tijdens de eerste fase wordt d.m.v. een 3D FFT analyse in kaart gebracht in welk deel van de twee-dimensionale golfgetal ruimte zich de golfcomponenten bevinden die de meeste energie vertegenwoordigen. Op basis hiervan wordt een beperkt aantal harmonische golfcomponenten gekozen waarvan de complexe amplitudes worden opgelost in de tweede fase. Simulaties met synthetische radar data illustreren de kenmerkende aspecten van de prestaties van de twee onderzochte methodes.

Met een overtuigender proof of principle als doel wordt hoofdstuk 5 gewijd aan het toepassen van de ontwikkelde methodiek op werkelijke velddata. Tijdens een offshore campagne van een onderhoudsschip werden zowel ruwe radar data als bijbehorende data van een aan boord geïnstalleerde bewegingssensor geregistreerd. Aangezien geen betrouwbare golfmeting in de buurt van het schip werd gedaan, richten de analyses in hoofdstuk 5 zich op een vergelijking tussen de gemeten en voorspelde scheepsbewegingen. Dit vereist een extra stap in de ontwikkelde methodiek die de bewegingsresponse van het schip berekent op basis van de uit de radar data afgeleide golfvoorspelling. Hiervoor is gebruik gemaakt van lineaire overdrachtsfuncties in het frequentie domein.

De resultaten van voorspellingen van de scheepsbewegingen worden gepresenteerd en vergeleken met gemeten scheepsbewegingen waarbij een zeer significante overeenkomst tussen beiden wordt aangetoond. De correlatie tussen gemeten en voorspelde heave beweging bijvoorbeeld, gebaseerd op tijdreeksen met een minimale lengte van 1 uur, bedraagt tussen de 0.77 en 0.86.

De algemene conclusie luidt dat de ontwikkelde methodiek heeft geleid tot een overtuigend proof of concept voor deterministische voorspelling van scheepsbewegingen op basis van golfobservaties met navigatieradar.

1

INTRODUCTION

1.1. OPERABILITY: STATISTICAL VS DETERMINISTIC APPROACH

A common factor involved with Maritime, Offshore and Naval operations and transport is the surface waves on the ocean. More specifically, it's the random and 'unpredictable' nature of ocean waves and the resulting loads and motions of floating structures that turns them into a potential thread or at least complicating factor for many activities at sea. Examples of such activities are the landing of helicopters on floating landing platforms, lifting operations with a floating crane, the transfer of people between, from or to ships. For many such operations, a relatively short time interval can be identified as being the actual 'bottle neck'-phase during which the highest risk occurs of e.g. a too high-impact touch down of the helicopter on the deck, a collision of a lifted load with the platform from or onto which it is lifted or put down.

It has been common practice for many years to assess operability of offshore operations, critical with regard to vessel motions in waves, by considering statistical properties like significant wave height, significant response amplitudes or most probable maximum values. These are typical properties related to the sea surface elevation described as a *stochastic* process. Especially (but not exclusively) in cases where the response that is considered to be limiting the operability is non-linear, operability analysis are done offline: Beforehand, for different environmental conditions possibly occurring in a certain area and season, the response is computed and tested for the criteria which have been laid down for the considered operation. A more real time and empirical type of determining operability, yet still relying on stochastic grounds, is applied in e.g. helicopter aviation. Here, the relevant response is measured real time and tested against predetermined criteria. In countries around the North Sea, Civil Aviation Authorities (CAA) and helicopter operators are operating under a strict regime; for "small" vessels helicopters are only allowed to land and remain on deck if pitch and roll angles are less than 2 degrees and the 'average heave rate of the largest wave is less than 1 m/s for the last 20 minutes. (Zeilstra et al. [2015], CAA [2008]) Certified Heli-deck Monitoring Systems are used that measure heli-deck motions and provide on-board real time information that enables the landing officer to check if safety criteria are satisfied.

With the development of various ways to remotely observe the sea surface elevation using sensors like LIDAR, incoherent pulse radar and coherent frequency modulated wave (FMCW) radar, there has been recent interest in considering the (prediction of the) surface elevation and resulting floating structure motions from a *deterministic* point of view. This would allow for a different approach to operability: a glance into the future of the deterministic vessel motions or related properties could enable optimal timing of the critical phase of an operation or provide the rationale to adapt course or speed in order to avoid a critical event. This way, instead of just *assessing* the operational risk, *decreasing* it becomes possible. Moreover, indicating a window of opportunity or save course/speed *in advance* by means of an on board prediction system, could enable safe execution of an operation that would have to be considered not feasible without having this prediction available, thus increasing operability.

A generalized approach to assess the potential of on-board prediction of workable windows could be to assume workability for a given operation is related to a maximum allowed instantaneous wave height (herewith for the sake of generalization neglecting the fact that it is much more likely the *response* to the maximum wave than the max-

imum wave itself that will govern the operability). Assuming the critical phase of the operation under consideration has a duration of D_c , then one could consider the total percentage of time that the wave height is part of a time window with a minimum length D_c , during which the wave height does not exceed this maximum allowed wave height as a 'deterministic measure' for operability. Some statistical analysis of linear synthetic wave traces lead to Table 1.1 which presents these percentages for a chosen allowed maximum wave height of 3.0 m, for three different wave conditions and 4 different window lengths (D_c).

sea state	H_s	T_p	$D_c=30$ s	$D_c=60$ s	$D_c=90$ s	$D_c=120$ s
3	1,0	5,1	100%	100%	100%	100%
4	2,0	7,1	99%	98%	96%	93%
5	3,4	9,2	52%	22%	7%	3%

Table 1.1: Percentage of time wave height is part of a window with minimum duration of D_c s, during which the wave height does not exceed 3.0 m

As can be seen, a 100% workability is found in sea state 3, for which the most probable maximum is well below the chosen 3 m maximum allowed wave height. In sea state 4 however, the general rule of thumb would yield 4 m for the most probable maximum wave height, meaning that the chosen 3.0 m allowed maximum is likely to be exceeded, possibly leading to considering this sea state as not workable. However, as can be seen, a very large percentage of time, the wave height belongs to windows with the indicated lengths D_c where this maximum is *not* exceeded and even in sea state 5 considerable workable time windows occur. The percentages indicate that, being able to predict *when* these workable windows occur sufficiently in advance, a considerable amount of time can be considered as 'workable'.

1.2. RESEARCH INTO DETERMINISTIC PREDICTION OF SHIP MOTIONS USING REMOTE WAVE SENSING

It has been shown that in principle, for time scales in the order of tens of seconds, it is feasible to accurately predict wave elevation and related behavior like vessel motions in a deterministic way from a remote wave observation:

For long-crested waves [Morris et al. \[1998\]](#) and [Edgar et al. \[2000\]](#) reported on prediction accuracy of wave elevation computed with a linear wave model. They showed the effect of optimal truncation of input data for the initialization of the model and the effect of the shape of the wave spectrum and water depth on the prediction horizon. Also using a linear wave model for long-crested waves, [Naaijen and Huijsmans \[2008\]](#) considered the prediction accuracy using experimental data. E.g. [Trulsen and Stansberg \[2001\]](#), [Trulsen \[2005\]](#), [Blondel et al. \[2008\]](#) and [Shemer et al. \[2010\]](#) showed results using nonlinear wave models with experimental data of bi-chromatic and irregular long-crested waves.

Successful prediction of wave elevation and wave induced ship motions in short crested seas from experimental data was reported by [Naaijen et al. \[2009\]](#) and extended to the prediction of wave drift forces by [Naaijen and Huijsmans \[2010\]](#). For both studies the two-dimensional representation of the wave field was obtained by correlating a rather

limited number of input time traces of the wave elevation, recorded at a sparse set of locations, as suggested by Zhang et al. [1999] and Janssen et al. [2001]. Clauss et al. [2015] presented an approach on deterministic wave and ship motion prediction meant to be initialized by spatial snap shots of the wave elevation obtained by radar. The work focused on non-linearity in the wave evolution by using a Higher Order Spectral wave model.

The above mentioned references all have in common that for the initialization of the wave propagation, the wave elevation was exactly known in some spatial, temporal or spatio-temporal observation domain, be it by numerically synthesizing this observation or measuring it in a controlled environment. Measuring waves offshore, with no earth-fixed anchor point or reference available however, is not a trivial task. The necessity of a spatial observation domain that exceeds one single point, relevant since in nature waves are subject to directional spreading, and the wish for *remote* wave sensing in order to enable wave *prediction*, increases the challenge of wave observation in the field. At the time the research for this thesis started, no evidence for a feasible phase resolved remote wave observation method providing sufficient accuracy and spatial coverage was reported. An attractive candidate was identified though: nautical radar, the pulse radar operating in X-band that is part of every ship's standard navigation equipment. Under the condition that the sea surface roughness is sufficient, which is the case at sufficiently high wind speed, the electro-magnetic (EM) waves in the X-band, their length being in the range of 2.5-3.75 cm, interact with the sea surface according to a mechanism known as Bragg-scattering. As a result of this, a radar return is received from the sea surface and its modulation due to the longer gravity waves reveals valuable information about these gravity waves. The oldest reference reporting on current and wave observation by radar is Oudshoorn [1960]. It reports on current measuring by tracking of buoy reflectors visible on subsequent photographs of the radar screen and on visual inspection of wave directions from radar images near the entrance to the Rotterdam harbor and the estuaries in the South-West of the Netherlands. Until the early eighties, several publications report on visual wave observations from radar images. Hoogeboom and Rosenthal [1982] and Ziemer et al. [1983] are among the first who apply digital processing to radar images and show that the spectra of radar images, obtained by 2D FFT, are very similar to wave spectra obtained from conventional directional wave buoy measurements. Young et al. [1985] introduces the 3D FFT approach to radar images, which for many years has remained the basis for most efforts into wave spectrum, current and water depth retrieval from radar images.

Although the majority of publications using radar as a wave sensor has been focusing the retrieval of statistical wave properties (and surface current and water depth), especially last decade, various research efforts aiming for *deterministic* wave sensing and wave and wave induced motion prediction have been initiated:

In 2006, the joint industry program On-board Wave and Motion Estimator (OWME) was initiated by the Maritime Research Institute in the Netherlands (MARIN). The aim of the project was to develop a proof of concept for an on-board decision support system that would be capable of predicting quiescent motion periods on board of stationary vessels by using non-coherent nautical radar data as basis for a remote wave observation. (Dannenberg et al. [2010])

In 2009 the Dutch Ministry of Defense granted subsidy for the Small Business Innovation Research (SBIR) project 'Short-term motion prediction of navy vessels in heavy weather', its aim being the development of a demonstrator for a short-term motion prediction system, capable to predict the motion of a fast moving vessel (up to 25kn) in heavy seas with sufficient accuracy to support critical operations such as helicopter launches or landings. (Adegeest [2013])

Clauss et al. [2012] report on the German 'Loads on Ships in Seaway' (LaSse) project's result: a decision support system referred to as 'CASH' (Computer Aided Ship Handling) aims to detect incoming wave sequences possibly arousing critical ship motions in advance, thus providing operational support to avoid dangerous situations during both transit and static operations.

In 2007, the Office of Naval Research launched a Multidisciplinary University Research Initiative (MURI) titled 'Optimum Vessel Performance in Evolving Nonlinear Wave Fields'. The aim of this 5-year, 5 M\$ program was to develop a real time system for adaptive path optimization for minimizing wave induced vessel motions. Its technical approach was to use radar (both coherent and non-coherent were considered) for remote wave field sensing, predict the wave field using a non-linear wave model, compute non-linear ship motions and optimize the path to be followed. (Beck [2012]) One of the research topics in the MURI program also addressed what can be considered to be the main topic of this thesis: the coupling between radar images and a wave propagation model. As reported by Aragh et al. [2008], the chosen approach was to use a variational data assimilation scheme with a pseudo spectral non-linear wave model to obtain a wave observation from the radar images which can be evolved to obtain the predicted wave field. The project evolved towards the use of coherent and coherent on-receive¹ radar and resulted in the first reported evidence for fairly successful deterministic wave observation: Lyzenga et al. [2010] shows time traces of wave elevation obtained from a coherent and a coherent-on-receive radar which both compare fairly well with in-situ measurements.

Within the NATO Submarine Rescue System (NSRS) program, an initiative by the U.K. Ministry of Defense, deterministic wave prediction for the safe deployment or recovery of a rescue submarine from or onto a mother ship was addressed: Belmont et al. [2014] also used surface wave observations from nautical pulse radar based on 3D FFT analysis, but, as opposed to the above mentioned references, applied additional analysis to use these observations to initialize a linear wave propagation model. No validation against an independent reference observation is presented however: predictions are compared to the surface elevation provided by the wave radar itself, thus merely possibly giving evidence for the self-consistency of the combined sensor and analysis method, rather than validating its actual accuracy.

In 2010, the US Navy Office of Naval Research (ONR) issued a call for proposals for research and development of 'Environmental and Ship Motion Forecasting' (ESMF) as part of the so-called Enabling Capability 'Connectors and the Sea Base'. The Sea Base is

¹'Coherent' radar is capable of recording the phase shift between the transmitted and received EM signal, thus enabling Doppler processing to retrieve the velocity in the look direction of the reflector, in this case being the radial velocity component of the sea surface. With the 'coherent-on-receive' concept, a low cost non-coherent marine radar can be modified in order to enable Doppler processing. (See e.g. Smith et al. [2013])

a concept, developed in order to enable “Operational Maneuver from the Sea (OMFTS), the Marine Corps’ warfare doctrine where all logistics support will come from the sea, rather than from supply points ashore.” Next to motion-mitigating ramp and crane systems currently in development by ONR, the 23 M\$ ESMF program aims to mitigate delays in material transfer caused by excessive ship motion. (ONR [2010])

Alford et al. [2015] and Connell et al. [2015], report on fairly successful deterministic ship motion prediction achieved within the ESMF program, both applying coherent(-on-receive) radar.

It can be concluded that successes have been reported in various areas involved in the problem of deterministic wave and ship motion prediction, like e.g. the initialization of wave models from synthetic wave/radar data or the fast computation of non-linear wave fields and ship motions. However, despite the above mentioned research efforts, until the start of the research leading to this thesis, no evidence for successful (i.e. significantly accurate) prediction of deterministic wave elevation from *real* field data was reported, not even for conditions/situations where a linear approximation of the waves could be expected to be sufficient. This observation leads to the research objective as formulated in the next section.

1.3. OBJECTIVE OF THE RESEARCH

The objective of this research is to develop an alternative method for the analysis of data from non-coherent nautical radar, with the aim of using the extracted wave information to initialize a wave propagation model. Essentially, a method specifically tailored for *deterministic* (i.e. phase resolved) prediction is pursued which will be part of an overall processing chain which computes a deterministic prediction of ship motions.

The emphasis of the research will be on what has been identified as the ‘missing link’ or at least the link that lacks evidence from past efforts towards real time ship motion prediction: the deterministic detection and prediction of waves from (non-coherent) radar data. In order to limit the scope of the research and enable a focus on this crucial link in the processing chain, some simplifying boundary conditions to the problem are imposed:

- the used wave model will be linear
- the used ship motion response model will be linear

The main consequence of both simplifications will be that use can be made of fully established approaches for wave propagation and ship motion modeling, at the cost of the fact that successful application of the approach to be developed will be limited to relatively benign sea states. However, apart from the mentioned desired research focus, this limitation is justified by the intended application: since the deterministic ship motion prediction approach to be developed is the key component of a decision support system for offshore *operations*, it will have to suit the associated operational conditions, which in many cases are benign.

Further more, the research will be restricted to the case that the radar antenna position is fixed, which is the case for many offshore operations carried out with stationary

vessels; however, the approach to be developed will preferably require merely some obvious adaptations in order to be applied to the case of radar images taken from a ship with forward speed. It should be noted though that the intended applications are significantly different from the ones aimed for by e.g. (??), who investigated the option of active automated control of fast crafts based on real time remote wave observations. The latter application comes with rather different requirements to the wave observation, mainly being higher accuracy, and a much smaller range.

1.4. OUTLINE OF THE THESIS

Chapter 2 will address wave model initialization by means of FFT and the spatio-temporal domain within which waves can be predicted deterministically, based on a supposedly perfect wave observation given in a temporal or spatial observation domain. Understanding predictability in this sense is essential to assess maximum achievable prediction horizons for specific wave conditions and observation set-ups. The problem will extensively be discussed for 1D waves under the assumption that the wave direction is known.

Chapter 3 will consider the prediction of 2D waves (as opposed to 1D waves in Chapter 2) and non-perfect observation data (as opposed to the (as good as) perfect observation data used in Chapter 2). Based on the 2D FFT approach for wave model initialization (analogue to the 1D FFT used in chapter 2), this chapter will describe so-called dynamic averaging and evolution. This is a procedure with the objective of:

1. enhancing accuracy of the prediction in case of non-perfect observations
2. enabling a *continuous* prediction, i.e. *from 0 sec* into the future, at the center of the observation domain (which is in practice the radar antenna of the ship), despite the fact that no (reliable) observation data is available in the near range around this antenna (which is indeed the case for nautical radars on ships).

The theory of predictability presented for 1D in Chapter 2 will be extended to the 2D situation in this chapter.

An approach is presented to detect the 'main' wave direction in order to deal with the real life situation where the main wave direction cannot be known a priori, an issue that was left unaddressed in chapter 2.

Chapter 2 and 3 address spatio-temporal predictability and an approach for continuous data assimilation, assuming an actual (be it non-perfect) *wave observation*.

Chapter 4 specifically aims to pursue the question how to deal with the situation where it is not an actual *wave observation* that is available, but merely an observation of something which is supposedly related to the wave observation, being the radar back scatter. A simple physical model is provided for the back scatter which is obtained when observing ocean waves with nautical radar and 2 different methods are presented to invert radar images into wave elevation observations. The proposed methods are validated by applying them to synthetically generated radar images.

In Chapter 5, the most successful method resulting from the investigation in chapter 4 is applied to field data: Radar images recorded from a stationary vessel are used

to predict the vessel's motions which are compared to the recorded vessel motions for validation.

Conclusions and recommendations will finally be presented in Chapter 6

2

LIMITS TO THE EXTENT OF THE SPATIO-TEMPORAL DOMAIN FOR DETERMINISTIC WAVE PREDICTION

This chapter has been published by [Naaijen et al. \[2014\]](#).

2.1. SUMMARY

We discuss the spatio-temporal domain, here referred to as the predictable zone, in which waves can be predicted deterministically based on an observation in a limited spatial or temporal domain. A key issue is whether the group or phase speed of the observed waves governs the extent of the predictable zone. We have addressed this issue again using linear wave theory on both computer-generated synthetic wave fields and laboratory experimental observations. We find that the group speed adequately indicates the predictable zone for forecasting horizons relevant for offshore and maritime applications.

2.2. INTRODUCTION

When applying deterministic prediction, it is crucial to be well aware of its limitations. Concerning these limitations, the following distinction can be made:

1. Given an observation of the wave elevation in a limited domain in space or time, the associated spatio-temporal zone where an accurate prediction can be made is limited and will depend on the wave spectrum. This zone will be referred to as the theoretical predictable zone and will be explained in detail hereafter. A good understanding of this limitation is important to enable an efficient wave sensor positioning with regard to the target location and an adequate interpretation of predictions.
2. Depending on the applied wave model and the method of initialization using available observation data, the accuracy of the prediction itself will be limited.

The first issue has been raised in various publications. In [Morris et al. \[1998\]](#), [Edgar et al. \[2000\]](#) and [Naaijen and Huijsmans \[2008\]](#) the phase speed was assumed to govern the predictable zone. [Abusedra and Belmont \[2011\]](#) specifically explain why they believe the phase speed governs the predictable zone. On the other hand [Blondel et al. \[2010a\]](#), [Naaijen and Huijsmans \[2010\]](#), [Dannenberg et al. \[2010\]](#) and [Blondel and Naaijen \[2012\]](#) use the group velocity as the governing velocity concerning predictability. More specific explanations and observations that support this latter point of view can be found in [Wu \[2004\]](#) and [Naaijen et al. \[2009\]](#).

The aim of this chapter is to address this topic again and provide further explanation of predictability in space and time, supported by numerical simulations and experimental data, thus providing clarity on which wave speed governs predictability. In order to do this, irregular long-crested waves are considered.

The second issue is not addressed in this chapter.

2.3. APPROACH

An observation of the sea surface in a limited spatial, temporal or spatio-temporal domain is not sufficient to predict the sea surface elevation in the entire ocean for all time. The limited domain where a prediction can be expected to correlate well with the true surface elevation will be referred to here as the 'theoretical predictable zone'. The concept of theoretical predictable zone will be explained in detail in the section on predictability, following a brief description of a linear, long-crested wave model and its initialization from an observed time trace of the surface elevation. The section on predictability employs the method of stationary phase to explain the relevant wave speed governing the theoretical predictable zone. This theory will then be verified by means of numerical simulations, using both synthetic and experimental data, using the following approach:

Long-crested linear irregular waves with a given wave spectrum are synthesized in a spatio-temporal domain (x, t) . A time trace of these synthesized waves at one specific location x is then used to initialize a linear wave model as described in the next section. With the wave model, the surface elevation is computed in the entire domain (x, t) and compared to the synthesized waves. The difference between the computed (predicted) and the synthesized wave elevation will be quantified and referred to as the 'practical' prediction error. Additionally, a similar procedure is followed using experimental data: long-crested waves are generated in a basin, and measured by a number of probes. The wave elevation at one probe is used to initialize the wave model which will then compute the wave elevation at the remaining probes. At each of these remaining probes the 'practical' prediction error can be determined. The theoretical predictable zone indicates where in space and time an 'accurate' prediction is possible. Comparing this to the practical prediction error obtained from the actual simulations will provide insight in the adequacy of the chosen definition of the theoretical predictability.

2.4. A LINEAR MODEL FOR PROPAGATION OF LONG-CRESTED WAVES

In the following it is assumed that all waves are long-crested and traveling in the same direction and that this direction is known. Under these assumptions, prediction of the wave elevation with a linear wave model is straightforward and has been addressed several times (Morris et al. [1998], Trulsen and Stansberg [2001], Blondel et al. [2010b], Clauss et al. [2009], Naaijen and Huijsmans [2008] to name a few). We will consider the case where the measurement used as input for the prediction is a time trace of the surface elevation observed at a fixed location. Then the linear wave model used can be expressed as

$$\eta(x, t) = \text{Re} \left\{ \int_0^{\infty} \hat{\eta}(\omega) e^{i(k(\omega)x - \omega t)} d\omega \right\} \quad (2.1)$$

where η is the wave elevation, ω is the angular frequency, $\hat{\eta}(\omega)$ is the Fourier transform of the time series of surface elevation at a reference location, and $k(\omega)$ is the wavenumber related to ω according to the linear dispersion relation.

A discrete form of this integral can be written

$$\eta(x, t) = \text{Re} \left\{ \sum_{m=0}^{M/2} \tilde{\eta}_m e^{i(k_m x - \omega_m t)} \right\} \quad (2.2)$$

where the complex amplitudes $\tilde{\eta}_m$ can be obtained from a Discrete Fourier Transform (DFT) of a time trace of duration T . Here $\omega_m = \frac{2\pi m}{T}$, k_m is related to ω_m through the linear dispersion relation, and M is the number of samples in the time trace. Having obtained the discrete complex amplitudes, they can be used in equation (2.2) to compute the prediction for the surface elevation at any required location and time (x, t) .

2.5. PREDICTABILITY

2.5.1. PREDICTABLE ZONE

The limited predictable zone afforded by equations (2.1) or (2.2) has been discussed before (e.g. Morris et al. [1998], Wu [2004], Naaijen and Huijsmans [2008], Blondel et al. [2010a], Naaijen and Huijsmans [2010], Dannenberg et al. [2010], Blondel and Naaijen [2012], Abusedra and Belmont [2011]). This theory is briefly revisited here, see figure 2.1.

Suppose the wave elevation is measured during the time interval from O to T at location x_0 . T is the duration of the measurement. The question is where in space and time this measurement is useful for prediction of the surface elevation. To address this question, we first make the trivial observation that each individual term in equation (2.2) is a sinusoidal oscillation uniform throughout space and time, with crests and troughs propagating with the phase speed, but with no otherwise localizable information in space or time. Localizable information appears through the superposition of terms in equation (2.2), in the form of nonuniformities that we shall call wave packets and that propagate with the group velocity. The ability to give a prediction is therefore a matter of predicting the propagation of wave packets, which is given by classical ray theory, or which is captured by the method of stationary phase applied to the integral in equation (2.1). A wave packet within the interval OT , propagating with one particular group velocity, will contribute to the wave elevation between sloped lines OA and TB whose slope equals that particular group velocity, thus contributing to a prediction between t_{1a} and t_{1b} at location x_1 . A second wave packet with a higher group velocity, equal to the slope of line TA , can contribute to a prediction between t_{2a} and t_{2b} at x_1 . If the mentioned group velocities are the highest and the lowest associated with the wave spectrum, this leads to a triangular 'predictable' zone (OTA) indicated in dark gray in figure 2.1.

In a real-time application of wave prediction, obviously the trace OT has to be acquired before it can be processed. So in the ideal case, neglecting computational time, only the part of OTA on the right-hand side of T can be considered as 'prediction'. The remainder of OTA should be referred to as 'hindcast'. However, this distinction will not be made in the rest of this paper.

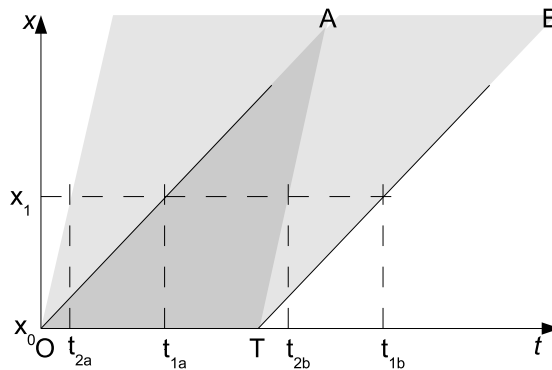


Figure 2.1: Construction of predictable zone

For any time t at any location x we can sum up the relative amount of energy in wave packets arriving from the time interval OT at x_0 . The result of the summation can be interpreted as a predictability indicator

$$P(x, t) = \frac{\int_{\omega_l}^{\omega_h} S(\omega) d\omega}{\int_0^{\infty} S(\omega) d\omega} \quad (2.3)$$

where $S(\omega)$ is the energy density spectrum of the wave elevation. ω_l and ω_h are the lowest and the highest possible frequencies, respectively, for which energy of wave packets could be propagated from OT at x_0 to the target time and location x, t . Frequencies ω_l and ω_h follow from the highest and lowest possible group velocities respectively for which this is the case. These group velocities are given by

$$c_{gl} = \frac{x - x_0}{t - T} \quad (2.4)$$

$$c_{gh} = \frac{x - x_0}{t} \quad (2.5)$$

and can be interpreted as follows: a wave packet within the interval OT at x_0 with a group velocity higher than c_{gl} will have passed location x already at time t , while a wave packet within the interval OT at x_0 with a group velocity lower than c_{gh} won't have arrived at location x yet at time t .

We have assumed that, since we are dealing with gravity waves, the group velocity is a strictly decreasing function of frequency, and we have $c_{gl} > c_{gh}$. P depends on x and t due to the dependence on c_{gl} and c_{gh} and the integration boundaries ω_l and ω_h .

The predictability indicator P proposed here is based on the wave spectrum S within linear wave theory for a uniform and stationary medium, thus S itself is assumed to be independent of x and t . In reality, these assumptions will not hold, and the spectrum will evolve in space and time.

Following Wu [2004], $1 - P$ can be interpreted as a prediction error indicator, quantifying the relative amount of wave energy represented by the 'unpredictable' frequencies. (Wu [2004] uses $\sqrt{1 - P}$, we use $1 - P$ instead.)

A question that has been raised several times (Wu [2004], Naaijen et al. [2009], Abusedra and Belmont [2011]) is whether the slope of the lines bounding the predictable zone is given by the group or the phase speed. For gravity waves the phase speed exceeds group speed, meaning that the prediction horizon (the furthest point in the future that can be predicted) would reach further into the future for group speed. An answer to this question can be found from the method of stationary phase as indicated by Abusedra and Belmont [2011] and briefly discussed in the next paragraph, or it can be found from simulations as those presented in section 2.6.

Figure 2.2 shows contour lines with intervals of 0.2 of $1 - P$ based on the wave spectrum observed during one of the basin experiments carried out for this study and assuming the group velocity determines ω_l and ω_h . The slopes of the contour lines depend on the contour level for $1 - P$. This can be explained by considering figure 2.1 again, where it was assumed that there exist a fastest and a slowest propagation speed. It was assumed

that the line TA bounds the dark gray area with 100% predictability (where $1 - P = 0$). On the right-hand side of TA fast propagating wave packets originating from x_0 for $t > T$ will contribute to the surface elevation, and $1 - P > 0$. On the right-hand side of the line TB, even the slowest propagating wave packets from x_0 for $t > T$ will contribute to the surface elevation, and $1 - P = 1$. Therefore a fixed value of $1 - P$ between 0 and 1 should result in a contour line with a slope between those of lines TA and TB. Defining the theoretical predictable zone as $1 - P$ being smaller than a threshold value, it is obvious that the size and shape of the predictable zone will depend on the chosen threshold value. As shown below, contour plots of the practical prediction error from simulations show the same behavior, the contour plots of the practical prediction error show different slopes for different contour levels.

Similar simulations as described in section 2.6.2 have been carried out by [Abusedra and Belmont \[2011\]](#), who examine plots in the (x, t) -plane indicating whether at a certain point (x, t) , the maximum error obtained from 1000 realizations is less than a given value. Observing the slopes of the area where this is the case, as done in [Abusedra and Belmont \[2011\]](#), is equivalent to observing the slopes of contour lines of the practical prediction error Err in equation (2.11) at a certain contour level. The slopes that will be found to be bounding the zone where the *practical* prediction error Err (or the equivalent practical error as defined by [Abusedra and Belmont \[2011\]](#)) is less than a threshold value will depend on the threshold, as is the case for the slopes of contour lines of the *theoretical* prediction error indicator $1 - P$ as explained above. This is confirmed by simulation results described in section 2.6, figure 2.6(b).

Further insight about the relevance of group or phase speed is provided by considering a cross section of a contour plot instead of the slope of the contours, see figure 2.3. Schematic theoretical prediction zones, defined as domains within which $1 - P$ is less than an arbitrary threshold value, are drawn for the case of group and phase speed, indicated by OTA_g and OTA_p respectively. Plotting the practical prediction error found from simulations together with the two versions of the theoretical error indicator $1 - P$ and examining a cross section at the position indicated by the dashed line would reveal clearly whether it is $1 - P$ based on group or phase speed that better matches the obtained simulation results for the practical prediction error. Such figures are presented in section 2.6.

2.5.2. METHOD OF STATIONARY PHASE

The method of stationary phase provides an approximate evaluation of the integral in equation (2.1) and suggests an answer to the question raised here. An explanation of the method related to linear dispersive waves can be found in e.g. [Murray \[1974\]](#), and was also given by [Abusedra and Belmont \[2011\]](#) and is summarized here.

Equation (2.1) describes the surface elevation $\eta(x, t)$ as a superposition of linear modes with wave numbers k and frequencies ω related by the linear dispersion relation $\omega = \omega(k)$. Assuming a fixed ratio x/t and examining the properties of the wave field as x and t become large, it is convenient to rewrite the complex exponential in equation (2.1) as

$$e^{i(kx - \omega t)} = e^{it(kx/t - \omega)} = e^{it\chi(k, x/t)} \tag{2.6}$$

where χ is the so-called phase function. For large values of t , this exponential represents

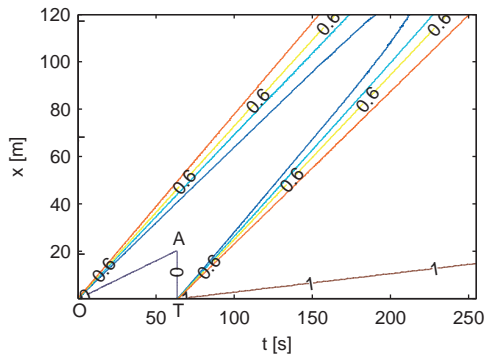


Figure 2.2: Contour plot of theoretical predictability $1 - P(x, t)$ in spatio-temporal domain.

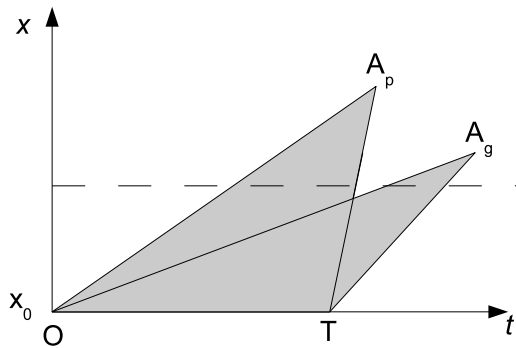


Figure 2.3: Schematic $1 - P(x, t)$ in spatio-temporal domain for group and phase speed.

rapid oscillations that are such that in the integration in equation (2.1), the positive and negative parts effectively cancel each other out, except in the vicinity of k_0 and ω_0 , where the derivative of the phase function χ with respect to k is zero

$$\frac{\partial \chi}{\partial k}(k_0, x/t) = 0 \quad (2.7)$$

and consequently we have the group velocity

$$c_g(k_0) \equiv \frac{\partial \omega}{\partial k}(k_0) = x/t \quad (2.8)$$

The meaning of this is that in the limiting case of large x and t , for an observer moving at constant velocity x/t , only wave packets whose group velocity equals x/t will significantly contribute to equations (2.1) or (2.2). For a point (x_1, t) in figure 2.1 to be predictable, based on an observation at location x_0 between O and T, all lines that can be drawn through the point, with slopes corresponding to energetic frequencies in the wave spectrum, should cross the observation OT. This results in a predictable subset of points (x, t) indicated by the dark gray triangle OTA in figure 2.1, with the slopes of lines OA and TA being equal to the group velocities associated with the highest and lowest frequency, respectively, at which significant energy is present in the observation.

With c_{gl} and c_{gh} in equation (2.4) and (2.5) being group velocities, the associated frequencies are related by

$$c_{gl} = \left(\frac{1}{2} + \frac{k_l h}{\sinh(2k_l h)} \right) \frac{\omega_l}{k_l} \quad (2.9)$$

and

$$c_{gh} = \left(\frac{1}{2} + \frac{k_h h}{\sinh(2k_h h)} \right) \frac{\omega_h}{k_h} \quad (2.10)$$

where h is the water depth.

As rightfully pointed out by [Abusedra and Belmont \[2011\]](#), it is not obvious that for any point in the triangle OTA, the magnitudes of x and t are sufficiently 'large'. In order to assess the required magnitudes of x and t for the above analysis to be valid, we will resort to numerical simulations and laboratory experiments.

2.6. SIMULATIONS

2.6.1. PROCEDURE

We have employed Monte–Carlo simulations to verify the theory on predictability using the model outlined in section 2.4: a DFT of a time trace of length T of the wave elevation observed at one specific location, which could be the first probe for simulations of the experimental data, is used according to equation (2.2) to make predictions of the wave elevation at other locations. The result can be compared with synthetic waves and with measurements from experiments.

Figure 2.4 shows a sample time trace of predicted and true wave elevation in a time window around $t = t_{1a}$ and at $x = x_1$ as indicated in figure 2.1. The prediction is based on the observed time trace OT at $x = x_0$. As can be seen, the agreement is less good at the left-hand side of the figure, as expected, since at earlier times we are outside the predictable zone where $1 - P$ is increasing.

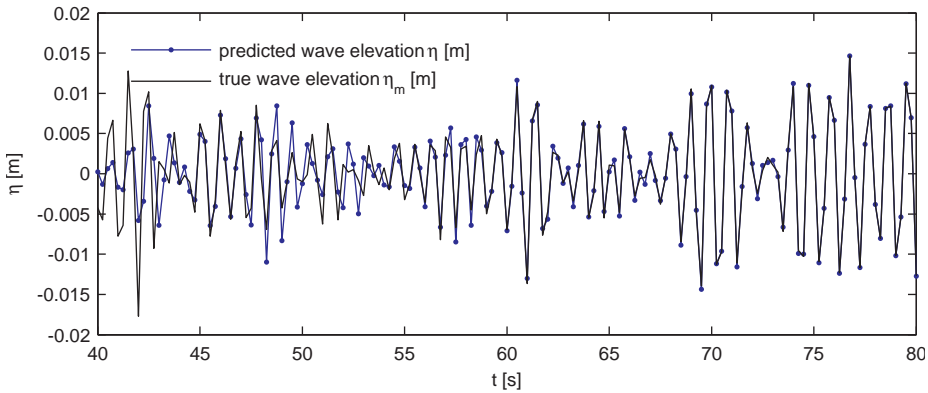


Figure 2.4: Predicted and true wave elevation around left boundary of predictable zone.

We define the mismatch between prediction η and true wave elevation η_m as

$$Err(x, t) = \frac{\langle (\eta(x, t) - \eta_m(x, t))^2 \rangle}{2\sigma^2} \quad (2.11)$$

where η is the predicted surface elevation, η_m is the measured or synthesized surface elevation, σ^2 is the variance of the measured or synthesized wave elevation averaged over all probes, $\langle \cdot \rangle$ denotes ensemble average.

We notice that $Err = 0.5$ in the case that we predict a flat surface $\eta(x, t) = 0$. Also $Err = 1$ if the prediction η has the same variance but is otherwise uncorrelated with the measured or synthesized wave elevation η_m . For values $Err \geq 0.5$ we may consider the prediction as useless.

For experimental data we achieve an 'ensemble' by using partly overlapping time traces, separated by Δt , see figure 2.5. The interval Δt was chosen to optimise convergence of the practical prediction error, this is discussed in appendix A.

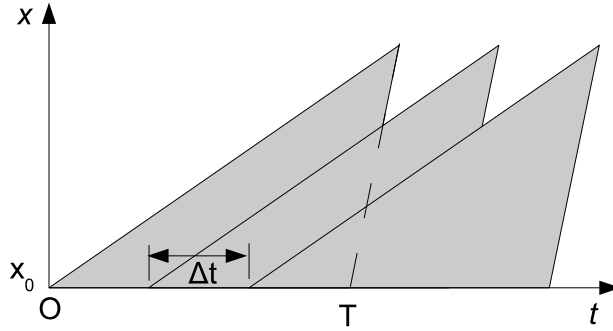


Figure 2.5: Obtaining multiple realizations by partially overlapping time traces.

From a time trace of length T at the reference location x_0 , we obtain a prediction which is expected to be accurate within the theoretical predictable zone. The theoretical predictable zone, which is the domain where $1 - P$ is less than a chosen threshold, can be determined based on group or phase speed. In case of phase speed, the propagation velocities in equations (2.4) and (2.5) would have to be substituted by the phase speeds

$$c_{pl} = \frac{\omega_l}{k_l} \tag{2.12}$$

and

$$c_{ph} = \frac{\omega_h}{k_h} \tag{2.13}$$

Both options are indicated by the triangles in figure 2.3. The practical prediction error Err is computed for large $x - x_0$, such that both of these theoretical prediction zones become clearly discernible. This in order to observe whether the practical prediction error Err confirms the assumed theoretical predictable zone based on group or phase speed.

2.6.2. SIMULATIONS USING SYNTHETIC WAVES DATA

SYNTHETIZATION OF WAVE DATA

A linear wave model has been used to synthesize the wave data. In order to avoid any systematic coincidence between the frequencies used in the generation of the synthetic waves and the ones that are used in its analysis by means of a DFT, generation has been carried out using non-equidistantly spaced frequencies: the waves are composed of N components, each representing an equal amount of wave energy. $N = 2000$ has been used in this study. Consequently the discrete frequencies are spaced closer together near the peak of the spectrum and further apart at the low and high frequency ends of the spectrum. Each realization of the wave field is generated using a different set of random phase angles, thus assuring independence between the different realizations.

RESULTS

Figure 2.6 shows contour plots of both the theoretical prediction error indicator, $1 - P$ based on group velocity, and the practical prediction error as defined in equation (2.11) from simulations averaged over an ensemble of size 5000. The wave spectrum S was chosen identical with the spectrum observed during one of the basin experiments mentioned in the next section, a JONSWAP spectrum with a significant wave height $H_s = 0.024$ m and mean zero crossing period $T_2 = 0.87$ s. Although the result for Err has converged, as shown in the appendix in figure A.1, still an apparently random variation of the error Err is observed. For this reason $Err(x, t)$ has been smoothed by a two dimensional filter in space and time before constructing the contour lines of Err in figure 2.6(b).

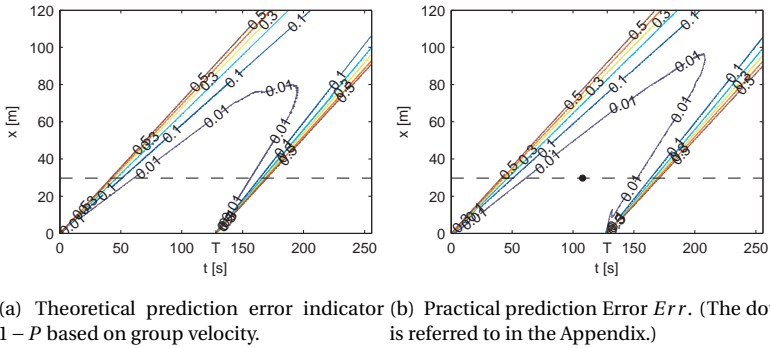


Figure 2.6: Contour plots of theoretical error indicator $1 - P$ based on group velocity and practical prediction error Err from simulations with synthetic wave data.

Although $1 - P$ is not directly comparable to Err , we do observe that the two regions outlined in figures 2.6(a) and 2.6(b) are both qualitatively and quantitatively quite similar.

Figure 2.7 shows the practical prediction error Err against time at $x = 30$ m, which is a cross-section in time at the location indicated by the dashed horizontal line in figure 2.6(b). Figure 2.7 also contains the theoretical prediction error indicator $1 - P$ for the location indicated by the dashed lines in figure 2.6. Two versions of $1 - P$ are shown, based on the group and phase speeds.

It is seen that $1 - P$ based on group velocity quite accurately matches the practical prediction error Err while poor agreement is found for $1 - P$ based on phase speed. The simulation results clearly indicate that it is the group velocity that governs the predictable zone.

2.6.3. SIMULATIONS USING EXPERIMENTAL WAVE DATA

EXPERIMENTS

We employ data of experiments in two different towing tanks, at the Ship Hydromechanics Department at Delft University of Technology, The Netherlands (TUD), and at Ecole Centrale Nantes, France (ECN). During these experiments, irregular waves were gener-

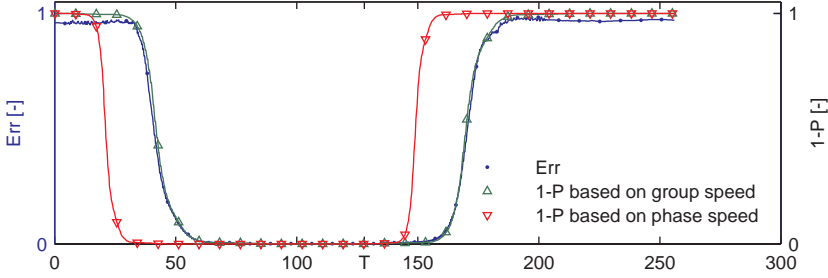


Figure 2.7: Prediction error against time at $x = 30$ m.

ated and measured by an array of probes. Using the measurement at the first probe positioned closest to the wave maker, the amplitudes and phase angles of the terms in equation (2.2) are obtained by DFT. Using the same formula enables calculation of the wave elevation at the remaining probe locations at any required moment in time, which then can be compared to the measurements at these probes, enabling computation of the practical prediction error Err . Figure 2.8 schematically depicts the experimental set up with the numbered dots indicating the probes. The positions of the probes, which are not exactly equidistant, are listed in table 2.1. The water depth during the experiments amounts to 2.13 and 2.81 m for the TUD and the ECN towing tank respectively.

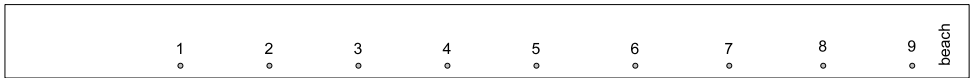


Figure 2.8: Layout of probes in basin. The wavemaker (WM) is to the left.

probe nr	position from WM flap, TUD	position from WM flap, ECN
[-]	[m]	[m]
1	41.02	18.48
2	53.42	24.43
3	65.92	30.26
4	79.35	36.11
5	90.06	42.29
6	102.33	48.23
7	115.03	54.11
8	127.50	60.29
9	-	66.14

Table 2.1: Probe positions for TU Delft and EC Nantes experiments.

Characteristics for the experiments are listed in table 2.2 where H_s is the significant wave height, T_p is the peak period, T_2 is the mean zero crossing period, and ϵ is average

wave steepness

$$\varepsilon = \sqrt{2}k_p\sigma \quad (2.14)$$

where k_p is the peak wave number of the spectrum, and σ is the standard deviation of the surface elevation.

facility	H_s	T_p	T_2	ε
[-]	[m]	[s]	[s]	[-]
TUD	0.025	0.923	0.885	0.040
ECN	0.031	2.008	1.523	0.011

Table 2.2: Summary of characteristics of wave conditions.

Both experiments are supposed to correspond to a JONSWAP wave spectrum having a peakedness factor $\gamma = 3.3$.

The data in table 2.2 corresponds to the values observed at the first probe, i.e. the reference probe that was used as input for the predictions. The main difference between the two experiments is the order of magnitude of the probe distances: for the experiments carried out at TUD this is in the order of 10 peak wavelengths, while for the ones conducted at ECN, the probes are positioned approximately 1 peak wavelength apart.

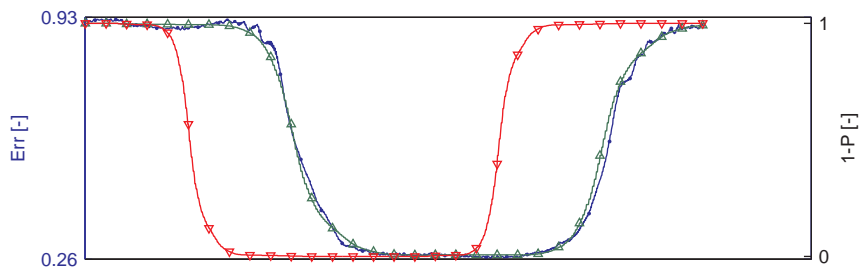
RESULTS

The error indicator $1 - P$ and the actual error Err from simulations with the TUD data are shown in figure 2.9. As was done for the simulations with synthetic data, cross sections of the contours of Err and $1 - P$, i.e. time traces of the practical prediction error Err (left y -axis) and the theoretical error indicator $1 - P$ (right y -axis), based on group and phase speeds, are presented for probes 1 (observation probe), 2, 4 and 6. The bottom figure represents the observation probe (probe 1) where an observation of length 128 s was used as input for prediction at the remaining probes.

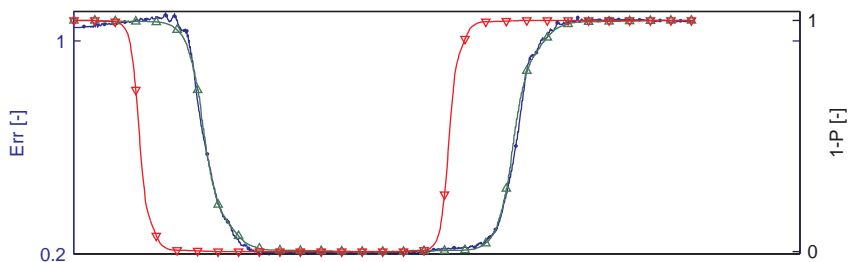
In order to make a visual inspection of the match between Err and $1 - P$ easier, the left y -axis corresponding to Err has been scaled such that the minimum and maximum values of Err correspond to values of 0 and 1 for $1 - P$, respectively. This axis scaling is justified by the fact that $1 - P$ only gives a qualitative indication of the expected prediction. $1 - P$ has been determined according to a numerical computation of equation (2.3) using the spectrum S observed at the observation probe. The limiting value for Err is not exactly equal to 1 at each probe due to the fact that a slightly different variance σ^2 was observed at different probes in the basin.

It is seen that the curves representing Err and $1 - P$ based on group velocity coincide well, while the assumption of phase speed governing the predictable domain is quite inadequate. From these figures we conclude that, at least for the propagation distances employed in the TUD experiment, the boundaries of the predictable zone are governed by the group velocity.

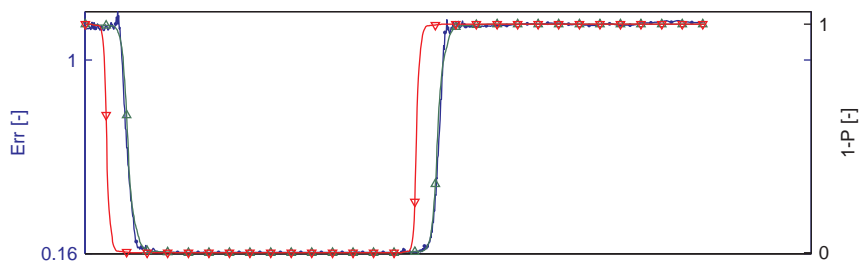
Recall that the method of stationary phase requires the propagation time and distance to be large. As indicated in figure 2.9 the smallest propagation distance, the distance from probe 1 to probe 2, amounts to 9.3 peak wave lengths. The presented results using data from the TUD experiment do not indicate what conclusions could be drawn



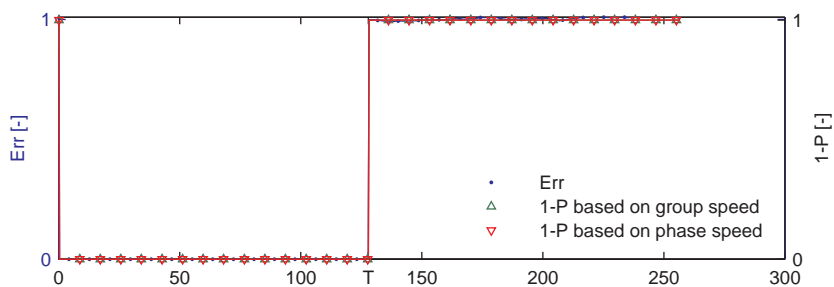
(a) Probe 6, $x/\lambda_p = 46.1$



(b) Probe 4, $x/\lambda_p = 28.8$



(c) Probe 2, $x/\lambda_p = 9.3$



(d) Probe 1, $x/\lambda_p = 0.0$

Figure 2.9: Prediction error and error indicator from TUD data.

for the *minimum* required propagation time and distance for the method of stationary phase to be useful.

In order to conclude about smaller propagation distances, data from the ECN experiment is considered. Here the distances between the probes, see table 2.1, amounts to approximately one peak wavelength only. Results are shown in figure 2.10. Again, the bottom figure represents the observation probe (probe 1). An observation of length 76.8 s was used. Also for these rather limited propagation distances, it is seen that the theoretical prediction error indicator based on group velocity shows significantly better agreement with the practical prediction error than the theoretical prediction error indicator based on phase speed.

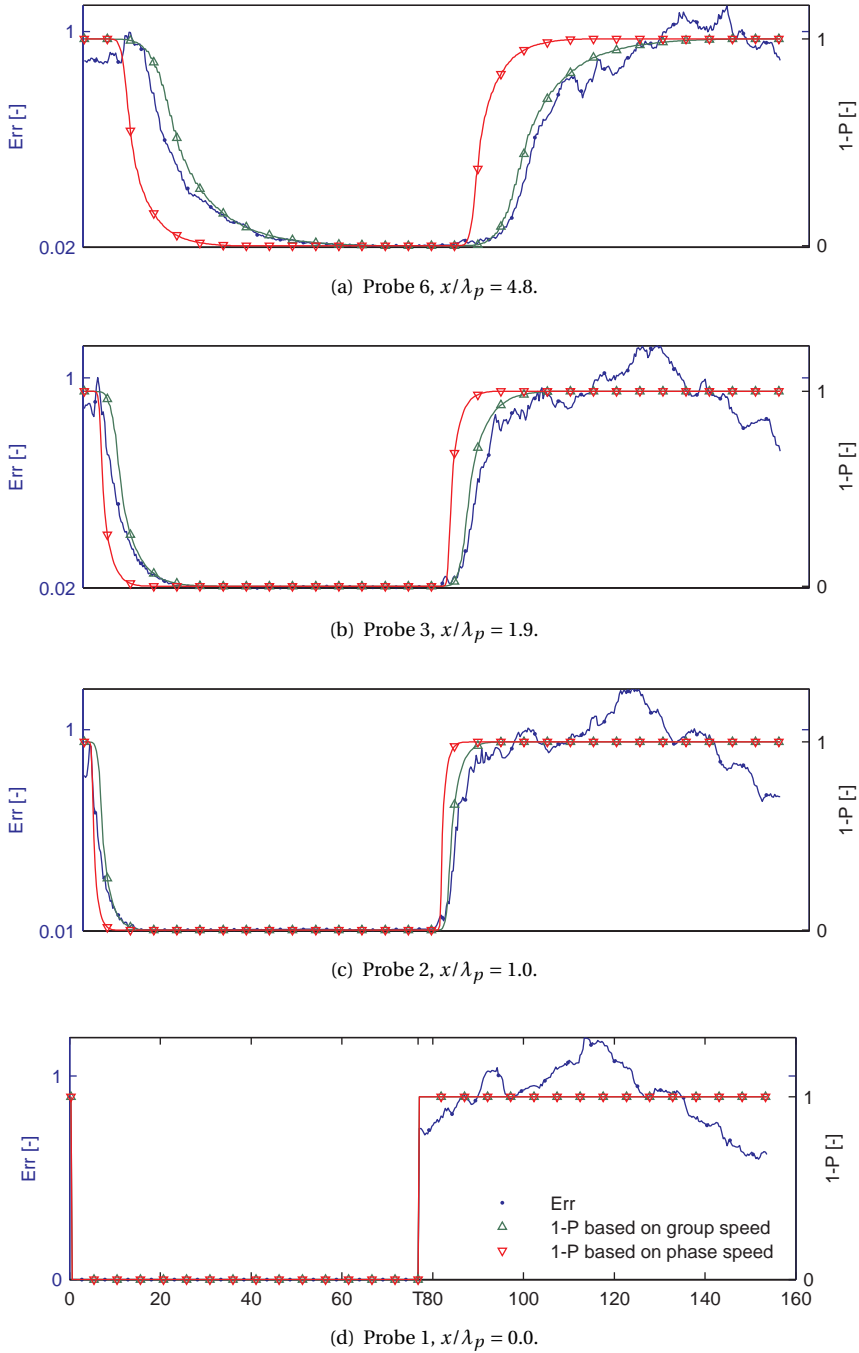


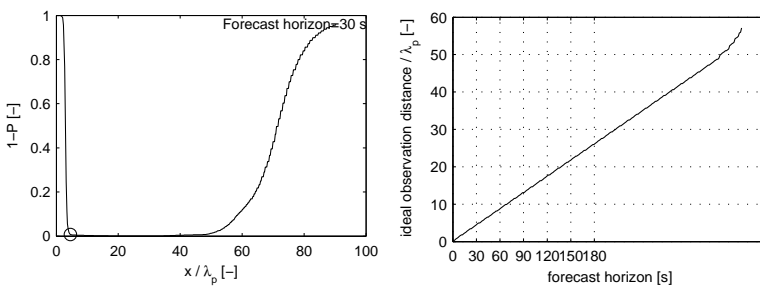
Figure 2.10: Prediction error and error indicator from ECN data.

2.7. PREDICTION HORIZON AND OPTIMAL PREDICTION DISTANCE IN PRACTICAL APPLICATION OF DETERMINISTIC WAVE PREDICTION

In order to relate the above results to the practical application of deterministic wave prediction in maritime and offshore operations, we will here estimate the minimum required distance between observation site and prediction site for typical prediction horizons of 30–120 seconds (Dannenberg et al. [2010]). Therefore, the contour plots of the theoretical predictability in figure 2.6 are considered again. On full-scale this figure corresponds to a JONSWAP spectrum with a peak period of 5.0 seconds. The ideal distance between observation and prediction site would be such that:

- it is large enough for the prediction site to be inside the predictable zone implied by the observation, and allowing a prediction some time into the future,
- it is not so large that the accumulation of errors ruins the prediction.

In order to identify these ideal distances, vertical cross sections of the contour plots of the theoretical predictability in figure 2.6(a) are considered: for a given required prediction horizon, the ideal distance between observation and prediction is defined here as the distance from the observation to the closest point where $1 - P$ is smaller than a chosen threshold value of 0.01. Figure 2.11(a) shows a vertical cross-section of the contour plot of $1 - P$ for a value of t that corresponds to a 30 s forecast on full-scale. The above defined ideal distance is indicated by the circle in figure 2.11(a). The distance x is normalized by the peak wavelength in this figure. The observation site is at $x = 0$. Figure 2.11(b) shows the ideal observation distance for a range of forecast horizons between 0 and 180 s. As can be seen, a forecast horizon of 30 seconds requires an observation distance between 4 and 5 peak wavelengths, for which it has been shown from the experiments in figure 2.10 that it is indeed the group velocity that governs the predictable zone.



(a) $1 - P$ against distance for Forecast horizon = 30 s. (b) Ideal distance against forecast horizon.

Figure 2.11: Ideal distance and forecast horizon.

2.8. CONCLUSION

We have shown that for deterministic wave prediction applied on propagation distances and forecasting horizons of practical interest to offshore operations, the predictable zone is governed by the group velocity of the waves.

2.9. ACKNOWLEDGMENTS

This research has been carried out within the research project 'PROMISED Operations' (Prediction Of wave induced Motions and forces In Ship, offshorE and Dredging Operations), funded by 'Agency NL', a department of the Dutch Ministry of Economic Affairs, Agriculture and Innovation and co-funded by Delft University of Technology, University of Twente, Maritime Research Institute Netherlands, Ocean Waves GMBH, Allseas, Heerema Marine Contractors, IHC. KT was funded by the University of Oslo (UiO) and the Research Council of Norway (RCN) through grants 177464/V30 and 214556/F20.

3

DYNAMIC AVERAGING AND EVOLUTION

Parts of this chapter have been published in [Wijaya et al. \[2015\]](#).

3.1. SUMMARY

This chapter presents a scenario that *integrates* both the initialization of a 2D wave model using an observation domain similar to what can be provided by nautical radars on ships (a 2D ring-shaped observation domain), and the propagation of the waves itself, into a continuously updated procedure.

This integration, which is achieved by a dynamic averaging-evolution procedure will be shown to provide:

1. a prediction accuracy which is significantly higher than the accuracy of the observation itself.
2. the ability to provide a *continuous* prediction, i.e. *from 0 sec (which will be called 'now-cast')* into the future, at the center of the observation domain (which is in practice the radar antenna of the ship), despite the fact that no (reliable) observation data is available in the near range around this antenna (which is indeed the case for nautical radars on ships).

The method uses multiple subsequent observations of the waves (radar images) in a different way than the more conventional 3D FFT and will be shown to be superior to 3D FFT for *deterministic* prediction purposes.

Verification will be done using synthetic radar images, taking into account only one of the modulation mechanisms known to play a role in radar observation of ocean waves, being so-called shadowing.

The presented scenario is not able to deal with counter propagating waves. A separate step is proposed to detect the main propagation direction of the waves which needs to be known.

(Chapter 4 will present the model that can cope with counter propagating wave systems and does take into account a more realistic interpretation of radar data.)

The theory on predictability presented in Chapter 2 will be extended to the 2D situation.

3.2. INTRODUCTION

3.2.1. A BRIEF HISTORY OF WAVE OBSERVATION AND PREDICTION USING NON-COHERENT NAUTICAL RADAR

Starting with [Hoogeboom and Rosenthal \[1982\]](#) and [Ziemer et al. \[1983\]](#), who both applied 2D FFT analysis to reveal qualitative wave phenomena from radar images and [Young et al. \[1985\]](#), who extended to 3D FFT, enabling detection of surface current, the vast majority of the efforts so far to use the nautical radar as a wave sensor has been based on spectral methods dedicated to retrieve statistical wave parameters such as mean wave period, wave direction, non-phase-resolved directional wave spectra and properties that could be derived from the surface elevation like water depth and surface current speed and direction.

The magnitude of the back scatter from the ocean surface received by a radar antenna is not only related to the physical properties of this wave surface. It is affected by many factors such as transmitted power, (logarithmic) signal amplification and mean sea surface Radar Cross Section (RCS), whose precise effects in practice cannot be quantified. Therefore, the question how the absolute magnitude of the (analyzed) radar signal relates to the absolute wave elevation cannot easily be answered. For the detection of wave directions and lengths, as well as water depth and surface current, this question is not necessarily relevant. This is different for problems where we are interested in e.g. wave energy density spectra or actual deterministic surface elevation. So regardless whether it is a statistical or a deterministic wave observation that is pursued, when using non-coherent radar, which only provides the magnitude of the back scatter, there is the remaining challenge of the scaling problem: how does the actual magnitude of the radar signal relate to the wave elevation. This problem has been addressed extensively. [Ziemer and Rosenthal \[1987\]](#) proposed the use of a parametrized modulation transfer function to derive surface elevation from radar images. [Borge et al. \[1999\]](#) propose an approximate relation for the significant wave height with two parameters that have to be calibrated. Both references make use of the so-called signal-to-noise ratio (SNR), being the ratio between those components resulting from the 3D FFT that represent actual waves and those that are considered as noise. This kind of approach for the scaling problem is also applied by [Borge et al. \[2004\]](#), and [Dannenberg et al. \[2010\]](#) in their pursuit for the measurement of deterministic surface elevation detection from radar images. A different approach was presented by [Dankert and Rosenthal \[2004\]](#) who introduced an empirical scaling method not requiring any reference observation: assuming that the back scatter intensity is related to the local incidence angle of the EM wave with the sea surface, this relation was mapped onto the time-averaged back scatter values which, under the same assumption, would be related to the local averaged incidence angle, the latter being known by the distance from the antenna and antenna height above the surface. The question how to reveal the scaling between back scatter data from non-coherent radar and wave height has been subject to many more publications, see e.g. [Buckley and Aler \[1998\]](#), [Gangeskar \[2014\]](#) and [Wijaya and van Groesen \[2014\]](#).

Based on the 3D FFT approach by [Young et al. \[1985\]](#), various efforts were done to retrieve the actual surface elevation deterministically, all basically applying the following procedure (which will be explained in detail in the proceeding of this chapter): a 3D

FFT is applied to a sequence of radar images after which components that do not map to (a certain band width around) the dispersion relation are considered as non-wave-related noise. This will be referred to as 'dispersion filtering'. For the inverse transformation, only those components that sufficiently satisfy the dispersion relation are used, thus eliminating noise.

Borge et al. [2004], Dankert and Rosenthal [2004] and Hilmer and Thornhill [2014] used this approach to address the possibility for wave *observation*, while Dannenberg et al. [2010], Adegeest [2013] and Clauss et al. [2012] extended to *prediction*. The predictions in these references were obtained by simply applying an appropriate phase shift to the wave components resulting from the 3D FFT and dispersion filtering, corresponding to the space shift and time delay associated with the prediction. However, as was shown by Naaijen and Blondel [2012] and Blondel and Naaijen [2012], and as will be shown again in this chapter, the predicting capabilities of a linear wave model based on a 3D FFT analysis is rather limited: the accuracy of a phase resolved wave *prediction*, (i.e. the evolution into future time outside the spatial area of observation) decreases very fast with increasing evolution time/distance and it should be concluded that coefficients of a linear wave representation obtained by 3D FFT do not suit the purpose of deterministic evolution/prediction. For this, and possibly additional reasons, no (statistically significant) evidence for successful deterministic wave or ship motion prediction was reported in these references.

The fact that the accuracy of a sea surface *observation* based on 3D FFT and dispersion filtering could be significant is shown by Hilmer and Thornhill [2014] who report on experiments during which buoy measurements are compared to deterministic reconstruction of wave elevation obtained from navigation radar.

Belmont et al. [2014] used surface wave observations from incoherent radar, also based on 3D FFT analysis. Instead of directly propagating the wave components resulting from the 3D FFT analysis, they added an additional analysis step: the 3D FFT approach was used to construct a wave observation as mentioned above. Then they applied an additional analysis to use these observations to initialize a linear wave propagation model in a similar way as was done by Zhang et al. [1999], Janssen et al. [2001] and Naaijen et al. [2009], meaning that a series of time traces at a limited number of observation points was used to solve the coefficients of a linear wave field representation existing of a limited number of directional wave components. As an alternative, the same reference reports on a 2-FFT based approach, using the full spatial coverage offered by wave radar instead of selecting a limited number of point observations. No validation against an independent reference observation is presented however: predictions are compared to the surface elevation provided by the wave radar itself, thus merely possibly giving evidence for the self-consistency of the method, rather than validating its actual accuracy. Besides, the reported results themselves are unconvincing.

Another attempt, for deterministic wave observation, not relying on the classical 3D FFT approach, was reported by Aragh et al. [2008]. They used a variational assimilation scheme to match the obtained radar data with a pseudo spectral wave model and used the above mentioned approach by Dankert and Rosenthal [2004] to solve the scaling issue.

As mentioned in chapter 1 however, despite the mentioned research efforts, until the

start of the research leading to this thesis, no evidence for successful (i.e. significantly accurate) deterministic observation nor prediction of wave elevation (and resulting ship motions) from non-coherent radar was reported.

3.2.2. WAVE MODEL INITIALIZATION USING INACCURATE OBSERVATION DATA: DATA ASSIMILATION

As a first step towards a successful deterministic ship motion prediction approach, this chapter will isolate the following aspect of the overall problem:

How to initialize a linear wave propagation model using a highly inaccurate remote observation of the sea surface?

A key feature to the proposed answer to this question is a continuous assimilation between observations and model. Data assimilation is a procedure which “attempts to combine a physics-based model with observational data to provide an improved estimate of the state of a system that is better than what could be obtained by just using either observations or numerical models alone.” (Aragh [2007]) As a matter of fact, the mentioned combined 3D FFT - dispersion filtering approach for sea surface reconstruction is in essence also an assimilation method which acknowledges the fact that the observed data does not accurately represent the surface elevation. Aragh et al. [2008] uses a different assimilation scheme where a cost function, which is defined as the difference between radar observations and predictions from a nonlinear wave evolution model over a limited time interval, is minimized. The limited time interval is referred to as the assimilation interval. An adjoint method is used to calculate the gradient of the cost function.

Paalvast et al. [2014] applied a direct approach to feed simulated wave observations by radar into a 3D panel model using a frequency domain Green's function, allowing for direct integration with a computation of vessel exciting forces and resulting motions. Also here, the physics of the wave propagation behavior introduced by the Green's function, results in an improved observed and evolved wave field, whose accuracy is higher than the actual observation.

The main aim of this chapter is to present an alternative assimilation scenario that *integrates* both the initialization and the propagation into a *continuously* updated procedure, as opposed to the above mentioned assimilation approaches which all use a limited assimilation interval.

3.3. APPROACH

3.3.1. OBSERVATION DATA AND DOMAIN

Verification of the assimilation scenario to be proposed is done by using synthetically generated input data. This input data will resemble some aspects of actual radar images of the sea surface, nevertheless ignoring various aspects of actual nautical radar data:

From the synthetic sea surface elevation, synthetic radar-like images are constructed by only taking into account the geometric effect of so-called shadowing, which is the phenomenon that parts of the sea are invisible for the radar since the electro-magnetic (EM) radar waves are being blocked by other waves. In work by [Plant and Farquharson \[2012\]](#), investigated radar data do not support the hypothesis that geometric shadowing plays a significant role at low-grazing-angle. Indications are found that shadowing rather occurs as so-called partial shadowing. Yet in this study we have chosen to model the effect of shadowing by complete geometric shadowing.

Hydrodynamic and tilt modulation effects and other hardware specific properties that determine the real radar images, are ignored. Hydrodynamic modulation describes the modulation of the energy of the (wind induced) ripples by the interaction with the longer gravity waves and tilt modulation of the received signal occurs due to the changes of the effective incidence angle of the EM waves along the long wave slope. Apart from the fact that these effects are irrelevant for demonstrating the main contribution of the averaging and evolution scenario as presented in this chapter, this choice can be justified by the fact that hydrodynamic modulation is believed to be negligible in various publications considering observation of waves by radar at low grazing angles ([Dankert and Rosenthal \[2004\]](#), [Borge et al. \[2004\]](#), [Seemann et al. \[1997\]](#), [Lee et al. \[1995\]](#)). Besides, tilt modulation is an effect that can be inverted without significant loss of accuracy as will be shown in chapter 4.

Aspects introduced by specific sensor-related properties of a radar system, such as the mean contribution to the radar cross section, signal amplification and range dependency of the received signal are neglected here. These are in fact effects associated with the scaling issue, mentioned in previous section. One of the consequences of the chosen linear approximation for the wave modeling, is that the modeled evolution of the waves is independent of their amplitude. This allows us to propagate the received radar signal as is, postponing the scaling problem to a later stage of the processing chain. The scaling issue can therefore be ignored for the time being which is why it is not modeled in the synthetic radar data either. The scaling issue will be addressed in chapter 5.

In fact for the presented method, the source of the imperfections of the observed data is not relevant here: it does not affect its relevance nor applicability.

Common nautical x-band radars are pulse radars, alternately transmitting an EM pulse and receiving the return, unable to transmit and receive simultaneously. The short time between transmitting the pulse and the start of the receiver results in a near antenna blind range for which no return signal is available. Besides this absolute lack of data within this blind range, received near range back scatter can be too high to distinguish wave related effects and/or suffers from interaction effects with the ship's hull. For this reason, the range from which no actual useful data is available can be larger than the blind range. In general a ring shaped observation can be assumed to be available with an inner radius within which no (useful) data is available and an outer radius which is

determined by the pulse repetition frequency PRF of the radar. Consequently, a propagation model has to evolve the information inwards from the ring shaped observation area towards the radar position. Using a ring shaped observation domain surrounding the target location enables prediction in both uni- and multi-modal seas with wind waves and swell(s) coming from possibly substantially different directions. Specific attention will be paid to the question how to treat multi-modal seas in the proposed scenario.

3.3.2. TECHNICAL APPROACH

The approach followed in this chapter is as follows: sets of subsequent images of short crested waves are created by synthesizing the waves and adding the geometric shadowing effect. Using only a ring-shaped spatial domain (that corresponds to the range capabilities of nautical X-band radar) a first attempt is made to reconstruct the shadowed parts in this ring-shaped observation domain for each created image separately. Thus reconstructed ring-shaped observations of the surface elevation are used as input for the dynamic averaging-evolution scenario to be described. Surface elevation obtained after this averaging-evolution scenario can be compared to the originally synthesized wave elevation in both the ring-shaped observation domain and the near antenna area (including the target location, i.e. the antenna position) surrounded by the ring-shaped observation.

The chapter is arranged according to the successive steps in the approach of the investigations: section 3.4 will describe in detail how the synthetic radar images are created that will be used to verify the proposed method. Section 3.5, will cover the dynamic averaging-evolution scenario (DAES) which aims to reconstruct/predict the wave elevation at the position of the radar using the synthesized radar images. Separate subsections will be dedicated to the following aspects:

1. 2 different methods that aim to 'repair', i.e. reconstruct the shadowed parts of each of the separate observed images before using them as input of the averaging-evolution scenario.
2. evolution of single observations, including a description of how to deal with multi modal sea states
3. dynamic averaging of multiple observations
4. evolution and prediction at the radar location

In order to make a comparison between the proposed DAES and more conventional 3D-FFT approach, the theory of 3D-FFT and dispersion filtering will be addressed in section 3.6. Section 3.7 will present the investigated case studies and the corresponding simulation results. A discussion of the results and conclusive remarks will be given in section 3.8.

3.4. SYNTHETIC DATA

In the first subsection we describe the construction of the synthetic surface elevation maps. These will be used to generate the synthetic radar images as described in the following subsection, and later to quantify the quality of the simulated surface elevation.

3.4.1. SYNTHETIC SURFACE ELEVATION

The synthetization of the surface elevation will be based on a chosen 2D wave spectrum $S(\omega, \theta)$, defined by a 1D spectrum $S_\eta(\omega)$ and a directional spreading function $D(\theta)$:

$$S(\omega, \theta) = S_\eta(\omega) \cdot D(\theta) \quad (3.1)$$

In the actual simulations addressed in section 3.7, the well known Jonswap spectral shape is used for S_η , further specified in paragraph 3.7.1 The directional spreading function with exponent s and main propagation direction θ_{main} as a function of wave propagation direction θ is given by:

$$D(\theta) = \beta \cos^{2s}(\theta - \theta_{main}) \text{ for } |\theta - \theta_{main}| < \pi/2, = 0 \text{ else} \quad (3.2)$$

with normalization β such that $\int D(\theta) d\theta = 1$

To synthesize a sea, we use a linear superposition of N regular wave components each having a distinct frequency and propagation direction. Equally spaced discrete frequencies ω_n are chosen by dividing the frequency band of the 1D spectrum ($S_\eta(\omega)$) containing significant energy by the number of desired components N . In order to assure that the sea is ergodic (Jefferys [1987]), it is required that only a single direction corresponds to each frequency.

A propagation direction is assigned to each wave component by randomly drawing from the directional spreading function $D(\theta)$ which is used as a probability density function, as proposed by Goda [2010].

With N the number of wave components used, k_n the wave vector corresponding to the frequency ω_n , and with ϕ_n phases that are randomly chosen with uniform distribution in $[-\pi, \pi]$, the sea is then given at polar spatial co-ordinates by:

$$\eta(\varphi, r, t) = \frac{\sum_n \sqrt{2S_\eta(\omega_n)} d\omega \cos(k_n r \cos(\varphi) \cos(\theta_n) + k_n r \sin(\varphi) \sin(\theta_n) - \omega_n t + \phi_n)}{\quad} \quad (3.3)$$

where $\sqrt{2S_\eta(\omega_n)} d\omega$ is the amplitude of each wave component and S_η is the wave spectrum.

Circular snapshots of the surface elevation with a radius of 2025 m are synthesized at a polar spatial grid with radial resolution 7.5 m and angular resolution 0.5 deg and at times which are multiples of $dt = 2sec$, corresponding to a realistic radar antenna rotation time.

3.4.2. SYNTHETIC IMAGES

With 'synthetic images' we refer to the synthesized radar observation of the surface elevation. When the sea will be scanned by the radar, parts of it will be hidden for the

electro-magnetic radar waves since they are blocked by other waves. In general, besides shadowing, tilt (slope of the sea surface relative to the look-direction of the radar) is considered to be an important modulation mechanism for wave observations by radar (Dankert and Rosenthal [2004], Borge et al. [2004]). (As Dankert and Rosenthal [2004], we neglect so-called hydromechanic modulation as described by e.g. Alpers et al. [1981].) However, in this paper we will consider only shadowing: our main aim is to show the capability of the proposed averaging-evolution scenario to cope with imperfect observation data for which the shadowing is most relevant. The question how the wave elevation can be obtained if it is the tilt that is supposed to be observed has been addressed by e.g. Dankert and Rosenthal [2004] and will be covered in chapter 4. It is briefly explained here how the shadowing effect is applied to the synthetic wave data which is according to Borge et al. [2004]:

With the radar at the origin $\mathbf{x} = (0, 0)$, we take a ray in a specific direction, starting at the radar position towards the outer boundary, using r to indicate the distance from the radar. We write $s(r)$ for the elevation along the ray, and Λ for the height of the radar. The straight line to the radar from a point $(r, s(r))$ at the sea surface at position r is given for $\rho < r$ by $z = \ell(\rho, r) = s(r) + a(r - \rho)$ with $a = (\Lambda - s(r)) / r$. The point $(r, s(r))$ at the sea surface is visible if $\ell(\rho, r) > s(\rho)$ for all $\rho < r$, i.e. if $\min_{\rho} (\ell(\rho, r) - s(\rho)) > 0$. At the boundary of such intervals the value is zero, and so the visible and invisible intervals are characterized by $\text{sign} \min_{\rho} (\ell(\rho, r) - s(\rho)) = 0$ and $= -1$ respectively. This leads to the definition of the characteristic visibility function as

$$\chi(r) = 1 + \text{sign} \left[\text{Min}_{\rho} \{ \Gamma(r - \rho) \Gamma(\rho) (\ell(\rho, r) - s(\rho)) \} \right] \quad (3.4)$$

where Γ is the Heaviside function, equal to one for positive arguments and zero for negative arguments. The visibility function equals 0 and 1 in invisible and visible intervals respectively. The shadowed wave ray, as seen by the radar, is then given by

$$s_{\text{shad}}(r) = s(r) \chi(r) \quad (3.5)$$

which defines the spatial shadow operator along the chosen ray. In figure 3.1 an example is visualized in which the visibility function χ is zero between r_1 and r_2

Repeating this process on rays through the radar for each direction, leads to the shadowed sea, $S_{\text{shad}}(\mathbf{x})$.

The synthetic image is obtained by removing information in a circular area around the radar position with a radius of r_0 . Then the ring-shaped synthetic image is described by

$$I(\mathbf{x}) = S_{\text{shad}}(\mathbf{x}) \cdot \Gamma(|\mathbf{x}| - r_0) \quad (3.6)$$

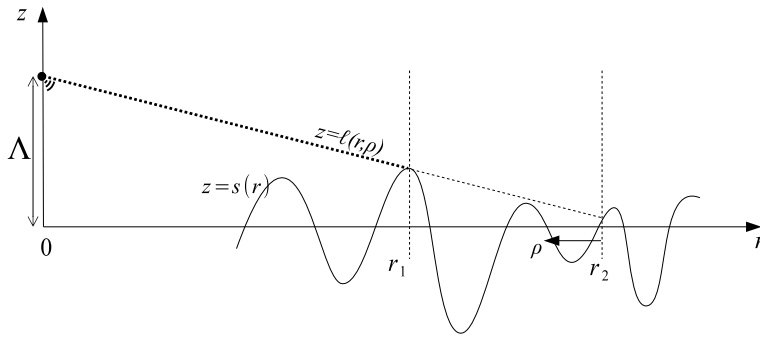


Figure 3.1: Shadowing: the visibility function is 0 between r_1 and r_2

3.5. DYNAMIC AVERAGING-EVOLUTION SCENARIO

This section presents the dynamic averaging-evolution scenario (DAES) which aims to provide (a prediction of) the surface elevation at the radar position using the disturbed (by shadowing) ring-shaped observation of the sea given by the synthetic images described in section 3.4.2. The first subsection deals with two simple ways to improve the quality of each individual synthetic image by attempting to fill in the gaps caused by the shadowing. These reconstructed surface elevation maps are then used in the dynamic averaging method to prepare updates that will be assimilated in a dynamic evolution or used as initial state for a prediction.

3.5.1. SPATIAL RECONSTRUCTION FROM SYNTHETIC IMAGES

In the following, two methods will be presented for a first attempt to reconstruct the synthetic images in regions where the observation is shadowed.

1. vertical shifting

The image data is interpolated to a Cartesian spatial grid (\mathbf{x}) and shifted vertically such that the spatial average (over the observation area) vanishes. With a scaling factor α to obtain the correct variance, this will produce the reconstructions R_n^0 as

$$R_n^1(\mathbf{x}) = \alpha (I_n(\mathbf{x}) - \text{mean}(I_n)) \quad (3.7)$$

As mentioned in the introduction, it is assumed that the true variance of the waves (or significant wave height) is known (from either additional analysis and/or a reference measurement) so α can be determined.

2. horizontal shifting

The second proposed method is described as

$$R_n^2(\mathbf{x}) = \alpha (I_n(\mathbf{x}) - E(I_n, -T_p/2)) \quad (3.8)$$

Here $E(I_n, -T_p/2)$ evolves the sea, again first interpolated to Cartesian co-ordinates, backwards in time over half of the peak period, for which in multi-modal seas we will take the peak period of the wind waves. The evolution itself indicated here with the operator E will be explained in detail in the next subsection. Note that for harmonic long crested waves with period T_p of which negative elevations have been set to zero elevation (to roughly resemble the effect of shadowing), reconstruction R^2 leads to the exactly correct harmonic wave.

3.5.2. EVOLUTION OF A SINGLE IMAGE

Let the reconstructed synthetic image, denoted by R , defined at Cartesian co-ordinates \mathbf{x} and obtained by either reconstruction method described in the previous subsection, be given by its 2D Fourier description as:

$$R(\mathbf{x}) = \sum_{\mathbf{k}} a(\mathbf{k}) e^{i\mathbf{k}\cdot\mathbf{x}} \quad (3.9)$$

where \mathbf{k} is the 2D wave vector. Coefficients a can be obtained by applying a 2D FFT on R . It should be noted that in the following the coefficient a representing the average is taken 0, i.e. $a(\mathbf{k} = (0, 0)) = 0$.

For given direction vector \mathbf{e} , define the forward evolution in the direction of \mathbf{e} as:

$$E_{\mathbf{e}}(R, t) = \Sigma_{\mathbf{k}} a(\mathbf{k}) \exp i [\mathbf{k} \cdot \mathbf{x} - \text{sign}(\mathbf{k} \cdot \mathbf{e}) \Omega(k) t] \quad (3.10)$$

where $k = |\mathbf{k}|$ and $\Omega(k) = \sqrt{gk \tanh(kh)}$ is the exact dispersion above depth h .

Changing the minus-sign into a plus-sign in the phase factor, the backward propagating evolution in direction $-\mathbf{e}$ is obtained.

For uni-modal sea states, such as wind waves or swell, there will be a main propagation direction \mathbf{e}_{prop} , the direction of propagation of the most energetic waves. Other waves in such wave fields will usually propagate in nearby directions, less than $\pi/2$ different from the main direction. In such cases we can take \mathbf{e}_{prop} as the direction to define the evolution. Actually, any direction from the half space of wave vectors can be chosen which has positive inner product with all wave modes that contain significant energy.

In multi-modal sea states, in most practical cases a combination of wind waves and swell, the situation will be different if the waves may a wider directional spreading than the $\pi/2$ difference from the main direction that was assumed for the uni-modal sea states. When the wave directions are spread out over more than a half space, one evolution direction so that all waves are propagated correctly cannot be found anymore. If only low-energy waves are outside a half space, one may still use a forward propagating evolution operator. Then an optimal choice for the evolution direction is the one for which the maximum portion of the total wave energy is evolved correctly. A way to identify this optimal direction is discussed now. Practically, we use a second (or more) 'control' image, and look for which vector \mathbf{e} the evolution of the first image according to equation (3.10) corresponds with the control image as good as possible in least-square norm; this then determines the *main evolution direction* (MED). Explicitly, given two successive images of the wave field, say R_1 and R_2 a small time dt apart, we compare R_2 with the forward evolution in the direction \mathbf{e} of R_1 and minimize the difference over all directions \mathbf{e} , defining the MED as the optimal value:

$$\mathbf{e}_{MED} \in \min_{\mathbf{e}} |E_{\mathbf{e}}(R_1) - R_2|. \quad (3.11)$$

Instead of minimizing a norm of the difference, one can also take the maximum of the correlation. For fields with limited directional spreading there will be a broad interval of optimal directions, in which case the average of the optimal directions can be chosen. For cases of multi modal sea states where the main propagation direction of the different modes deviate very much there is likely to be one distinct optimal MED. It is possible that with this method using the MED, a significant amount of wave energy is evolved in the wrong direction, depending on how much the main directions of the different modes differ. In the following we will use a simplified notation when evolving over one time step dt , namely

$$\mathcal{E}(R) = E_{\mathbf{e}_{MED}}(R, dt) \quad (3.12)$$

Evolving over several time steps, say $l \cdot dt$, is then written as a power (succession of evolutions) \mathcal{E}^l .

3.5.3. UPDATES FROM DYNAMIC AVERAGING

The reconstruction process described in subsection 3.5.1 gives approximate surface elevation maps R_n . The study cases will show that these reconstructions are still rather poor when compared to the exact synthetic surface elevation maps. In order to reduce the effect of this reconstruction error and thereby to improve the accuracy of the elevation prediction near the radar, we propose an averaging procedure in physical space. This procedure will involve three successive reconstructed images and the simulated wave field at the instant of the last image.

To set notation, the *simulated* sea (the simulation process will be detailed below) at time t will be referred to as $\zeta(\mathbf{x}, t)$; at discrete times $l \cdot dt$ we write $\zeta_l(\mathbf{x}) = \zeta(\mathbf{x}, l \cdot dt)$.

The simulation is initialized by taking for the first N_t time steps the N_t successive reconstructed images:

$$\zeta_l(\mathbf{x}) = R_l(\mathbf{x}) \text{ for } l = 1, 2, \dots, N_t \quad (3.13)$$

For the sake of notation simplicity, N_t will be taken 3 in the following. It should be noted though that N_t can be any positive integer. For the continuation, updates will be used to assimilate the evolution. We describe the update process at a certain time t_0 , which is a multiple of $3dt$. Available at that time are the simulated wave field at t_0 , to be denoted by $\zeta_0(\mathbf{x}) = \zeta(\mathbf{x}, t_0)$, the reconstructed image at time t_0 , and 2 previous images at times $t_{-1} = t_0 - dt$, $t_{-2} = t_0 - 2dt$; these reconstructed images will be denoted by $R_{0,-1,-2}$ respectively. Since these images R have substantial inaccuracies despite the reconstruction, it can be expected that an averaging procedure improves the quality. This averaging has to be done in a dynamic way to compensate for the fact that the images are available at different instants in time. Therefore the images R_{-1} and R_{-2} have to be evolved over one, respectively two, time steps dt . This produces $\mathcal{E}(R_{-1})$ and $\mathcal{E}^2(R_{-2})$, each representing, just as R_0 , an approximation of the wave field at time t_0 . But the information will be different, partly complementary, because the information at different time steps shows somewhat different parts of the wave because of the shadowing effect. Therefore an arithmetic mean will contain more information, and may also reduce incidental errors and noise. The ongoing simulation ζ_0 also gives an approximation of the sea at t_0 , and additionally in the near-radar area where R does not contain information. Choosing a weight factor w for the ongoing simulation ζ_0 , we take as update at time t_0 the following combination:

$$U_0(\mathbf{x}) = \left((1-w) \cdot \frac{1}{3} (R_0 + \mathcal{E}(R_{-1}) + \mathcal{E}^2(R_{-2})) + w \cdot \zeta_0 \right) (1 - \chi_{rad}) + \zeta_0 \chi_{rad} \quad (3.14)$$

where $\chi_{rad}(\mathbf{x})$ is the characteristic function (or a smoothed version) of the near-radar area: it indicates the near radar zone where no waves can be observed by $\chi_{rad} = 1$ and the remaining spatial domain by $\chi_{rad} = 0$ (possibly with a smooth transition over some chosen distance from 0 to 1). As mentioned, the number of reconstructed images to be

taken in the update, N_t , can be more or less than 3. (Moreover each of them could be given a different weight which has not been investigated.) The weight factor w has been chosen 0.5 resulting in equal weight for the ongoing simulation ζ and newly observed images R in the averaging.

3.5.4. EVOLUTION, PREDICTION AND PREDICTABILITY

EVOLUTION AND PREDICTION

The updates defined above will be used as assimilation data to continue the simulation. In detail, after the construction of an update, say U_{3m} , the simulation continues with this wave field as initial elevation field for three consecutive time steps:

$$\zeta_{3m+j} = \mathcal{E}^j(U_{3m}) \text{ for } j = 1, 2, 3. \quad (3.15)$$

This defines the full evolution in time steps dt , which is repeatedly fed with new information from the reconstructed images through the updates. This scenario can run in real time in pace with incoming real radar images.

A prediction can be defined, starting at any time $t_0 = l \cdot dt$ for a certain time interval ahead, without using any information of synthetic images later than t_0 . The prediction, say for a future time of $t \in [t_0, t_0 + \Pi]$, where Π is the prediction horizon, is then defined as:

$$P(t_0, \tau) = E(U_0(t_0), \tau) \text{ for } \tau \in [0, \Pi]. \quad (3.16)$$

PREDICTABILITY

It has been shown in chapter 2 that the prediction horizon is mainly governed by the group velocity of the observed waves and the size of the observation domain. The theory of predictability, covered for 1D waves in chapter 2, will be extended to the 2D case now. In case of a nautical radar, the spatial observation domain will be the ring-shaped area, previously indicated by $\chi_{rad} = 0$. As a consequence, the domain in which we can expect a reliable prediction is limited in space and time. See figure 3.2 which depicts a simplified (still 1D) schematic representation of the spatio-temporal observation and prediction domain. The radar position is indicated by B. OB can be considered as the latest available update, say U_0 . OA is the observable zone where $\chi_{rad} = 0$. The update in this zone originates from the averaging of R_0, R_{0-1}, R_{0-2} and the evolution of the previous update $\mathcal{E}^3(U_{0-3})$. AB is the near radar zone where $\chi_{rad} = 1$ for which the update U_0 originates from $\mathcal{E}^3(U_{0-3})$ only. The horizontal axis refers to the prediction time τ .

When initializing the above described DAES scenario, no simulation result ζ is available yet so no information can be provided in AB. With the slope of the line through A being equal to the group speed of the shortest waves observed, using the observation at OA only, no good prediction can be expected at target location B before $\tau = \tau_1$ since the (shorter) waves observed in OA at $\tau = 0$ haven't arrived yet at location B. The predictable zone in this case is indicated by the dark gray area. The sloped line originating from O has a slope equal to the group speed of the longest waves observed. For predictions at location B beyond time τ_2 inaccuracies will be introduced mainly by the fact that the longer waves observed at $\tau = 0$ have passed location B already. DAES as presented in this paper uses the evolution of the past observations and assimilates it with updated

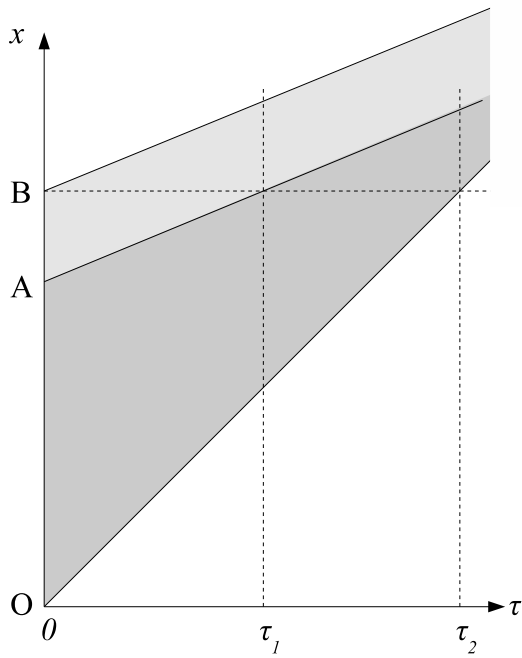


Figure 3.2: predictable zone

observations. As a result of this, after the scenario has been run for a while, evolved wave elevation will be available at AB. Together with the evolution of the wave elevation at OA and an updated observation at OA, the predictable zone will eventually be increased as indicated by the light gray area.

As an upper bound for the prediction horizon Π at B, τ_2 can be used: After τ_2 the prediction accuracy will certainly drop since the longer waves arriving at B were not part of the observation, as was shown in chapter 2. However, specifying the accuracy that is desired for the prediction, may reduce the prediction horizon Π compared to the above suggested upper bound: the prediction accuracy possibly decreases with increasing propagation distance/time, also before τ_2 .

Knowing the energy density spectrum of the waves, it is possible to define a qualitative indicator for the predictability and consequently the upper bound for the prediction horizon, based on the observation in a specified spatial domain. In chapter 2 this was done for a temporal observation domain. Analogously, a spatial observation can be used. Such an indication is very useful from a practical point of view: it can e.g. define the workability for a certain offshore operation if a minimum prediction horizon is required. In case of a spatial observation at OA and prediction available from the past up to location B, for any chosen prediction time τ , a sloped line can be constructed from O to (τ, B) . For $\tau > \tau_2$, waves with a group speed larger than the slope of the constructed sloped line are occurring, which have not been observed at OB. From the spectrum the relative amount of energy represented by these waves can be determined. This way the so-called predictability indicator *P.I.* for the antenna location can be constructed yielding a similar formulation as was given by equation (2.3):

$$P.I.(\tau) = \frac{\int_{\omega_l(\tau)}^{\infty} S(\omega) d\omega}{\int_0^{\infty} S(\omega) d\omega} \quad (3.17)$$

Please note that the predictability indicator was referred to as *P* in chapter 2 and will be labeled *P.I.* from here in order to distinguish from *P* as defined in equation 3.16.

where ω_l is the wave frequency corresponding to a group velocity which is equal to the steepness of the line connecting O to (τ, B) .

Assuming a linear representation of a 2D field, which can simply be interpreted as a summation of many 1D wave fields, each having a different propagation direction, the extension of *P.I.* to the 2-D situation can be based on the same interpretation:

$$P.I.(\tau) = \frac{\int_0^{\omega_l(\tau)} \int_0^{2\pi} S(\omega, \theta) d\omega d\theta}{\int_0^{\infty} \int_0^{2\pi} S(\omega, \theta) d\omega d\theta} \quad (3.18)$$

It has to be noted though that this straightforward extension towards to the 2D situation only holds for a circular observation domain: only then, the distance from the edge to the center, projected in the considered propagation direction, will be equal for

each possible propagation direction, and as a consequence $\omega_l(\tau)$ will not depend on propagation direction θ .

3.6. 3DFFT

As mentioned in the introduction, the majority of the attempts to retrieve the actual deterministic wave surface elevation from radar images reported in literature, has been based on 3D FFT techniques. This section addresses some relevant aspects of the 3D FFT approach. In order to demonstrate the superiority of the proposed DAES method, results of simulations using 3D FFT approach will also be presented in the following sections.

Let the discrete 3D Fourier transform of a series of N_t input images R_{ijl} , whose discrete points are defined at a Cartesian grid of points with intermediate distances dx and dy and time intervals dt , be given by:

$$F(\mathbf{k}_{mn}, \omega_q) = \sum_{i=0}^{N_x-1} \sum_{j=0}^{N_y-1} \sum_{l=0}^{N_t-1} R(\mathbf{x}_{ij}, t_l) e^{-i(\mathbf{k}_{mn}\mathbf{x}_{ij} - \omega_q t_l)} \quad (3.19)$$

where:

$$\mathbf{k}_{mn} = \left(m \frac{2\pi}{N_x dx}, n \frac{2\pi}{N_y dy} \right), \quad \omega_q = q \frac{2\pi}{N_t dt}$$

with $m \in [-N_x/2 + 1, N_x/2]$ and $n \in [-N_y/2 + 1, N_y/2]$, $q \in [-N_t/2 + 1, N_t/2]$

Since R is a real-valued function, the following relation yields:

$$F(\mathbf{k}_{mn}, \omega_q) = F^*(-\mathbf{k}_{mn}, -\omega_q) = F^*(\mathbf{k}_{-m-n}, \omega_{-q}) \quad (3.20)$$

where $*$ indicates the complex conjugate

The amplitude spectrum, one-sided with respect to the ω -axis can be defined as:

$$a(\mathbf{k}_{mn}, \omega_q) = p N_x^{-1} N_y^{-1} N_t^{-1} F(\mathbf{k}_{mn}, \omega_q) \quad (3.21)$$

where:

$$q \in [0, \frac{N_t}{2}], \quad p = 2 \forall q \in [1, \frac{N_t}{2} - 1], \quad p = 1 \forall q \in \left\{0, \frac{N_t}{2}\right\}$$

Using these amplitudes, which are not only a function of \mathbf{k} but also of ω , as opposed to the 2D inverse FFT given by equation (3.9), the loss-less inversion back to R yields:

$$R_{inv}(\mathbf{x}, t) = \text{Re} \left[\sum_{m=-N_x/2+1}^{N_x/2} \sum_{n=-N_y/2+1}^{N_y/2} \sum_{q=0}^{N_t/2} a(\mathbf{k}_{mn}, \omega_q) e^{i(\mathbf{k}_{mn}\mathbf{x} - \omega_q t)} \right] \quad (3.22)$$

The argument of vector \mathbf{k} equals the phase speed direction.

Suppose that t_0 indicates the time associated with the last image in the series of N_t input images, $R_{inv}(\mathbf{x}, t)$ will be an exact reconstruction of each input image R at any time used in the 3D FFT, i.e. any time $t = t_0 - l \cdot dt$, with $l \in [0, N_t - 1]$.

The surface elevation obtained this way is not evolving. This means that in order to obtain the wave elevation at the location of the antenna (which is surrounded by a zone where there is no observation available) and/or future times ($t > t_0$), some manipulation is required regarding equation (3.22). Maintaining the analogy with the described DAES we again use P to refer to the predicted wave elevation. In order to have an evolving wave field in accordance with the linear dispersion relation, we replace the explicit ω by the implicit $\Omega(\mathbf{k})$ to obtain prediction P :

$$P(t_0, \tau) = \text{Re} \left[\sum_{m=-N_x/2+1}^{N_x/2} \sum_{n=-N_y/2+1}^{N_y/2} \sum_{q=0}^{N_t/2} a(\mathbf{k}_{mn}, \omega_q) e^{i(\mathbf{k}_{mn}\mathbf{x} - \Omega(\mathbf{k}_{mn})(N_t dt + \tau))} \right] \quad (3.23)$$

with a still being the coefficients resulting from a 3D FFT on N_t images, the last of which taken at t_0 . An actual prediction ($\tau > 0$) can be obtained using equation (3.23), while due to the periodicity in space and time involved with equation (3.22), the wave elevation obtained from (3.22) when substituting a value $t > N_t dt$ would merely yield a repetition of the used observations.

The 3DFFT approach is often used in combination with a dispersion filter f in order to decrease any effects and disturbance that do not relate to the ocean waves: only coefficients a are used for the reconstruction/prediction for which \mathbf{k} and ω sufficiently closely satisfy the dispersion relation:

$$P(t_0, \tau) = \text{Re} \left[\sum_{m=-N_x/2+1}^{N_x/2} \sum_{n=-N_y/2+1}^{N_y/2} \sum_{q=0}^{N_t/2} f(\mathbf{k}, \omega) a(\mathbf{k}_{mn}, \omega_q) e^{i(\mathbf{k}_{mn}\mathbf{x} - \Omega(\mathbf{k}_{mn})(N_t dt + \tau))} \right] \quad (3.24)$$

E.g. [Aragh et al. \[2008\]](#) propose the use of a Gaussian filter for f and [Borge et al. \[2004\]](#) applies a Dirac Delta function. A simple 'triangular' filter is used here:

$$f(\omega, \mathbf{k}) = \max\left(0, \left(1 - \frac{|\omega - \Omega(\mathbf{k})|}{d\omega \cdot w_f}\right)\right) w_f^{-1} \quad (3.25)$$

in which ω is again the frequency associated with the 3D FFT, $d\omega$ is the frequency resolution in the 3D FFT ($d\omega = \frac{2\pi}{N_t dt}$) and w_f is a parameter defining the filter width. This way, f is defined such that its sum over ω equals 1 and its value tapers from its maximum value at ω equals (or is nearest to) Ω , to zero at ω deviates w_f steps of $d\omega$ from Ω . See figure 3.3 in which f is plotted for different w_f values for the case of $\Omega = 0.9$ (left) and $\Omega = 0.84$ (right), for $d\omega = 0.1$.

In the following, results for the prediction of the wave elevation obtained from the 3D FFT approach according to equation 3.24 will be presented using $w_f = 1$: some variations concerning the filter width w_f have been tried resulting in $w = 1$ to be optimal. This prediction will be used to compare with the result obtained from DAES given by equation 2.3. During the simulation, this 3D FFT process will be repeated using subsequent and overlapping series of images, without any averaging. Whether the wave elevation at the radar position will be available at $\tau = 0$, will therefore depend on the number of images N_t used for the 3D FFT: for small N_t , a significant portion of the total wave energy represented by the shorter wave components will not be able to cover distance AB in figure 3.2 within time $N_t dt$.

For all simulations using 3D FFT, $N_t = 64$ is used.

Concerning the predictability, discussed in paragraph 3.5.4, there are two additional aspects that need to be considered with regard to the application of $P.I.$ in the described 3D FFT approach:

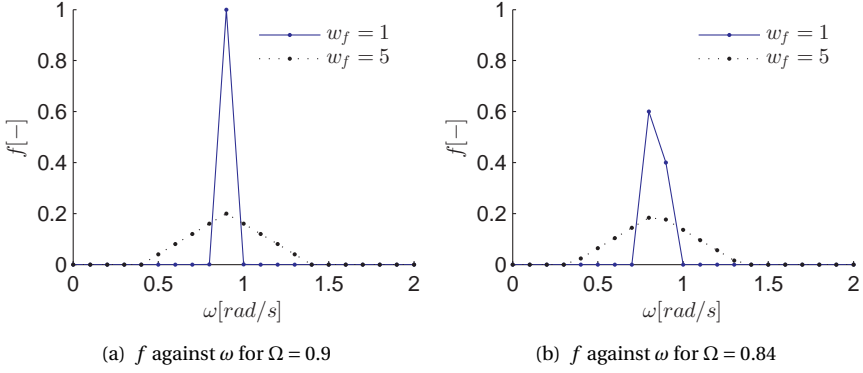


Figure 3.3: dispersion filter f for different filter widths w_f

1. No averaging with evolutions from the past is used: contrary to the DAES approach this 3D FFT approach represents an assimilation with a limited assimilation interval. As a result of this, the near antenna zone ($r < r_0$) indicated in figure 3.2 by AB will not contain information at any given time t_0 . For that reason, we have to take into account that not all (shorter) wave components observed in OA have arrived at B before τ_1 . This can be expressed in the predictability indicator $P.I.$ by adapting equation (3.18) as follows:

$$P.I.(\tau) = \frac{\int_0^{2\pi} \int_{\omega_l(\tau)}^{\omega_h(\tau)} S(\omega, \theta) d\omega d\theta}{\int_0^{2\pi} \int_0^{\infty} S(\omega, \theta) d\omega d\theta} \quad (3.26)$$

where ω_h is the wave frequency corresponding to a group velocity which is equal to the steepness of the line connecting A to (τ, B) .

2. It should be bared in mind that in case of a 3D FFT, the obtained wave component amplitudes a are not only based on the observation OA, but also on the $N_t - 1$ preceding observations. This makes the definition of the predictability less straightforward. In an attempt to take into account the fact that for certain τ the predictability should not be considered to be dependent on the observation OA at $\tau = 0$ only, but also on previous observations, a combined predictability indicator $P.I._{av}$ is defined as the average of all $P.I.$'s associated with each of the N_t used observations:

$$P.I._{av}(\tau) = \frac{1}{N_t} \sum_{n=0}^{N_t-1} P.I.(\tau + n \cdot dt) \quad (3.27)$$

3.7. CASE STUDIES

In this section we present the results for two study cases: one for wind waves and one with combined wind-waves and swell. Comparisons are presented between the predicted wave elevation, obtained by processing the synthesized images with both 3D FFT and the proposed DAES method and the exact wave elevation as it was synthesised.

We start to specify the sea data and other physically and numerically relevant parameters of the simulations, followed by the simulation results.

3.7.1. PARAMETERS OF THE STUDIED CASES

GEOMETRY AND SPATIAL GRID PARAMETERS

The seas that we consider evolve above a depth $h = 50m$. The height of the radar is an important quantity because the severity of the shadowing effect is governed by the ratio of radar height and wave height. We will report on a value of the radar height h_R of 15 m above the still water level for which rather severe shadowing occurs. The radar is assumed to be at a fixed position above the still water level. The wave elevation is synthesized on a polar spatial grid, with range and azimuth resolution set to 7.5 m and 0.5 deg respectively. We assume that the radar scans the ring area with outer radius $r_{max} = 1800m$ and therefore taper the synthetic images to value 0 at $r = 1800m$ by multiplying the used images R with a window function which smoothly tapers from 0 at $r = 1800m$ to 1 at $r = 1800 - 75m$. In order to take into account the earlier mentioned 'blind' zone close to the antenna up to $r_0 = 500m$, a similar window function is used tapering from 0 at $r = 500m$ to 1 at $r = 500 + 75m$ around the position of the antenna. In this chapter, the fact that a navigation antenna has a limited rotational speed, resulting in a different recording time for each recorded beam, is ignored: spatial snapshots are synthesized in which all points are associated with the same instant in time. The time interval between the subsequent snapshots, dt , is set to 2 s. During the simulation each image is first interpolated on a square spatial grid of size 512 x 512 points, with spatial step size $dx=dy=7.5$ m before applying one of the reconstruction methods mentioned in paragraph 3.5.1.

SEA STATES

We provide the properties of the wind waves and the swell separately; since we consider linear waves, the characteristics of the multi-modal sea state, which is a combination of the wind waves and swell, can be derived in a straightforward way. The properties of the waves, with related wave characteristics above depth $h = 50m$, are summarized in Table 3.1.

Sea	Jonswap			direction		wave characteristics				
	H_s	T_p	γ	θ_{main}	s	ω_p	k_p	λ_p	C_p	V_p
Wind	3	9	3	$-\pi/2$	10	.7	.05	125	13.9	7.4
Swell	1	16	10	$3\pi/4$	50	.4	.02	308	19.2	14.8

Table 3.1: Characteristics of sea and swell waves

The wind waves have main propagation direction from North to South, $\theta^W = -\pi/2$; the wave spreading is given by equation (3.2) with exponent $s = 10$.

The frequency spectrum of the wind waves is a Jonswap spectrum with peakedness factor $\gamma = 3$, peak period $T_p = 9s$, and significant wave height $H_s^W = 3m$. (The significant wave height is not relevant for the behaviour of the waves themselves in the simulation but it is an important factor that affects the amount of shadowing.)

The multi-modal sea consists of the above wind waves to which is added the swell waves. The swell consists of waves from the South-Eastern direction, $\theta^S = 3\pi/4$, peakedness factor $\gamma = 10$, wave spreading with $s = 50$, peak period $T_p = 16s$, and significant wave height $H_s^S = 1$.

The significant wave height of this combined sea state will be $H_s^{WS} = \sqrt{10} \approx 3.15$. The study cases of wind waves without swell and combined wind waves-swell will be denoted by W15 and WS15 respectively. For the number of discrete components N (equation (3.3)) used to synthesize the waves, 1500 has been used for the wind waves of W15 and 1500 and 700 for the wind waves and swell respectively of which WS15 is composed.

3.7.2. SIMULATION RESULTS

In this paragraph results of the simulations using both 3DFFT and DAES will be presented.

We start with presenting some graphical results of the DAES method:

Starting with the first three synthetic images, the dynamic averaging- evolution scenario is initiated. The described procedure is repeated at every time being a multiple of $N_t dt$ where 3 is used for the value of N_t . For a certain $t = t_0$, relatively shortly after starting the simulation, spatial snapshots of the synthesised wave elevation, (shadowed) geometric image and computed reconstruction of the wave field are presented in figure 3.4. Figure 3.4(a) shows the true wave elevation as synthesised at $t = t_0$. Figure 3.4(b) shows the shadowed image of the wave elevation depicted in figure 3.4(a): near the antenna, where $r < 500$ no observation of the wave elevation is supposed to be available and the elevation is taken equal to 0 there. The black parts indicate the shadowed parts of the image: due to shadowing no observation is available and also there the elevation is taken zero. Figure 3.4(c), shows the reconstruction $U_0(t_0)$ (or equally $P(t_0, \tau = 0)$). As can be seen the wave field, which is propagating with the main direction from North to South, i.e. in negative y -direction has evolved already some distance into the near-antenna zone. Figure 3.4(d) shows the reconstruction $P(t_0, \tau = 0)$ for t_0 such that the wave field has evolved to fill the entire blind near antenna range (i.e. $r < 500$).

A cross section in y direction at $x = 0$ in figure 3.4(b) of the shadowed waves is shown in figure 3.5. (Contrary to figure 3.4(b), the waves are shown for $r < r_0$ here as well. The right hand side y -axis is used to show the mentioned window function $1 - \chi_{rad}$). As can be observed for this particular wave condition and radar altitude of 15 m, the shadowing is rather severe: beyond $r = 500$ hardly any wave troughs are visible. Despite this poor quality of the observation, a fairly good reconstruction of the wave elevation near the radar $r < 500$ is obtained. This is shown by figure 3.6 which depicts a similar cross-section showing the synthesised wave elevation, referred to as "true wave", and the reconstruction $P(t_0, \tau = 0)$ obtained by DAES again for t_0 such that the simulation has already run sufficiently long for the reconstructed waves to fill the entire near-antenna

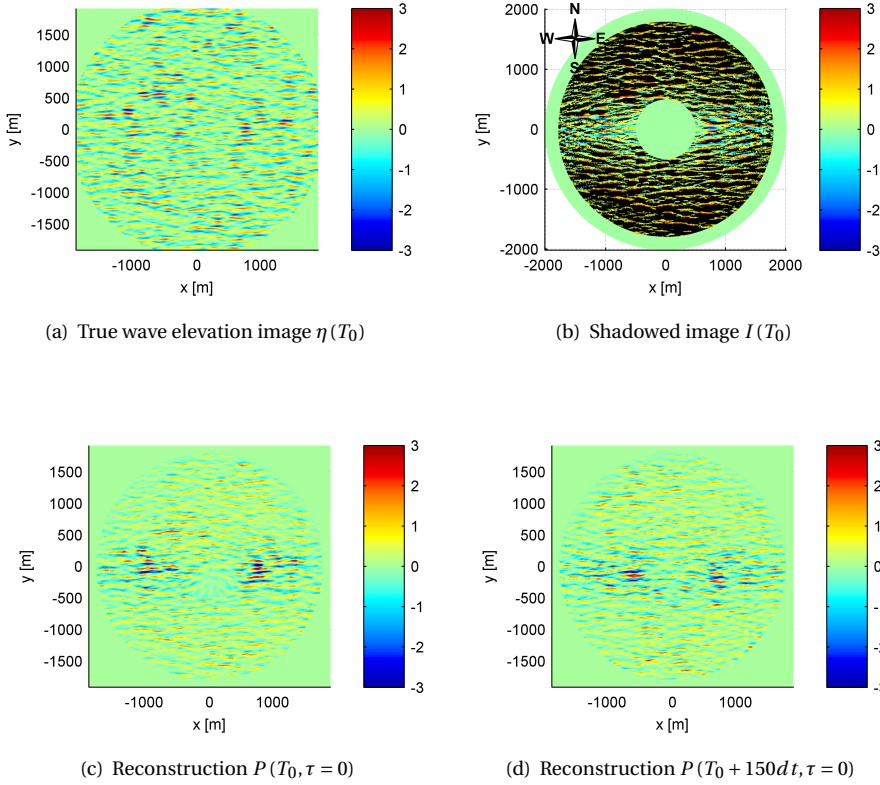


Figure 3.4: spatial snapshots of observation, true wave elevation and reconstruction for wave condition W15

blind zone.

CORRELATION

The accuracy of the prediction is quantified by the correlation coefficient $corr$, which correlates the prediction of the wave elevations, obtained from the simulation and the synthetic wave elevation. The correlation of the prediction of the wave elevation, τ sec ahead of t_0 , computed with the information available at time $t = t_0$ is defined as:

$$c(t_0, \tau) = \frac{\langle \eta(\mathbf{x}, t_0 + \tau), P(t_0, \tau) \rangle}{|\eta(\mathbf{x}, t_0 + \tau)| |P(t_0, \tau)|} \quad (3.28)$$

where $\langle \rangle$ denotes the inner product. P (introduced in equation (2.3)) denotes the predicted wave elevation which by definition is a function of \mathbf{x} and η (equation (3.3)) the synthetic wave elevation. (Since the synthetic wave elevation η was synthesized in a polar spatial grid, a linear interpolation was used to obtain it in the Cartesian grid referred to by \mathbf{x} .)

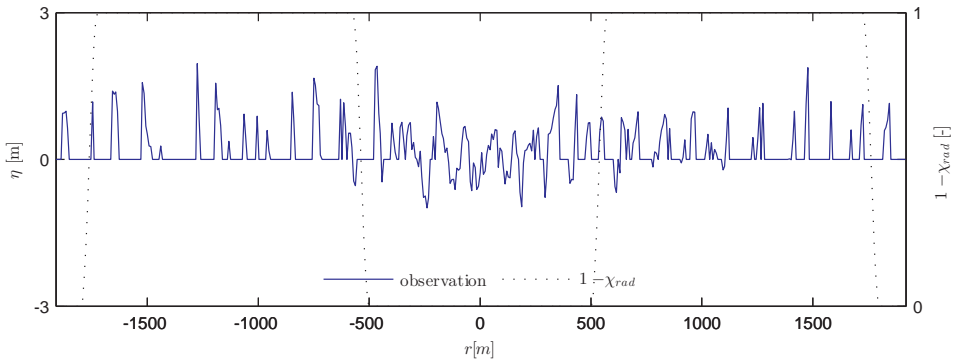


Figure 3.5: cross section along wave propagation direction of synthesized shadowed image

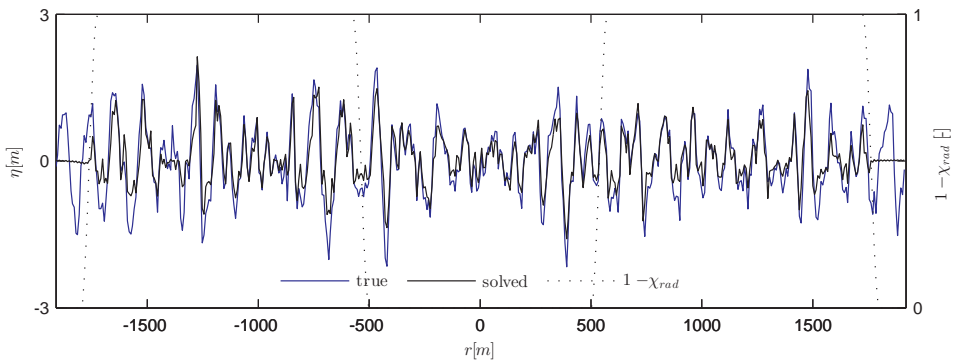


Figure 3.6: Evolution and true wave along a cross section in the main propagation direction

P and η for specified τ and t_0 are a function of \mathbf{x} so the correlation is taken over space (\mathbf{x}). Subsequently, the average is taken over t_0 to obtain a statistically more reliable *average* correlation coefficient $corr$:

$$corr(\tau) = \frac{1}{J} \sum_{j=1}^J c(t_{0j}, \tau) \quad (3.29)$$

Note the difference between τ and t_0 : t_0 is the time step of the simulation from which a prediction is calculated. Using the update scheme described in paragraph 3.5.3, t_0 is raised by $N_t dt$ every time step of the simulation. τ indicates the future moment in time, with respect to t_0 for which the prediction is computed.

(The correlation coefficient as defined above has the advantage of being independent of the amplitude or offset: multiplication of one of the signals with a constant or addition with a constant does not affect the correlation coefficient. This is a useful property to assess the accuracy of a prediction based on radar data for which the scaling with the absolute wave elevation is still an unknown. This scaling issue will be addressed in chapter 5 where real field data will be used.)

To exclude entrance effects, the computation of the correlation is restricted to t_0 such that all waves have evolved until the entire blind zone has been filled. For the presented simulations, this entrance amounts to roughly 200 s, i.e. 100 dt . The number of simulation steps J used for calculation of the correlation has been at least 550 for all presented results.

In order to compute $corr$, the predicted wave elevation η which is obtained in the Cartesian spatial grid of 512 x 512 points as mentioned in the previous paragraph, is interpolated to the same polar spatial grid at which the waves were originally synthesized. (Simulations for which the predictions were evaluated at the exact polar grid points at which the waves were synthesized were performed as well. The just mentioned interpolation appeared to have no significant effect on the obtained correlation coefficients.)

ACCURACY OF RECONSTRUCTION

The correlation coefficient has been computed for all investigated combinations of sea state and radar altitude and the distinction has been made between various sizes of the spatial domain: $corr$ is determined for $r < 50$, $r < 500$ and $r > 500$. Results are presented in table 3.2 and 3.3 for $\tau = 0$ which will be referred to as 'reconstruction'. 'Prediction' results (for which $\tau > 0$) will be presented in the next paragraph.

The first column in table 3.2 and 3.3 indicates the type of input data, single image reconstruction method (paragraph 3.5.1) and propagation scenario: 'Sea' refers to the perfect (not shadowed) synthetic waves, R^1 and R^2 refer to the simulations with shadowed waves using the two reconstruction methods as defined in paragraph 3.5.1 (i.e. R^1 for vertical shifting and R^2 for horizontal shifting). R^0 refers to simulations with shadowed waves applying no reconstruction of the individual images. DAES and 3DFFT refer to the propagation scenarios as described in section 3.5 and 3.6 respectively. The columns with 'Raw' and 'Rec' show the correlation of the synthetic images and the individually reconstructed images (both without having been subjected to DAES or 3D FFT) with the true wave elevation respectively. For the presented results, the scaling factor α in equation 3.7 and 3.8 was determined for each single reconstructed image separately as follows:

$$\alpha_n = \frac{H_s}{4 \cdot \sigma_{R_{n0}}} \quad (3.30)$$

where H_s is the significant wave height, assumed to be known. R_{n0} is referring to the unscaled reconstruction and $\sigma_{R_{n0}}$ refers to its standard deviation. This standard deviation is taken over the part of the image outside the blind near antenna zone, i.e. the part where $\chi_{rad} = 0$. In case of reconstruction method 1, the mean is taken over the part of the image outside the blind zone, i.e.:

$$R_{n0}^1 = I_n - \text{mean}(I_n \cdot (1 - \chi_{rad})) \quad (3.31)$$

	Raw	Rec	$r < 50$	$r < 500$	$r > 500$
Sea DAES	1.00	1.00	0.99	0.99	1.00
Sea 3DFFT	1.00	1.00	0.70	0.66	0.61
R^0 DAES	0.71	0.71	0.93	0.93	0.90
R^1 DAES	0.71	0.71	0.93	0.94	0.90
R^2 DAES	0.71	0.74	0.91	0.92	0.87
R^1 3DFFT	0.71	0.71	0.67	0.66	0.57

Table 3.2: Correlation at $\tau = 0$ for sea state W15

	Raw	Rec	$r < 50$	$r < 500$	$r > 500$
Sea DAES	1.00	1.00	0.99	0.98	0.99
Sea 3DFFT	1.00	1.00	0.67	0.64	0.60
R^0 DAES	0.70	0.70	0.92	0.92	0.90
R^1 DAES	0.70	0.70	0.92	0.93	0.90
R^2 DAES	0.70	0.72	0.90	0.90	0.86
R^1 3DFFT	0.70	0.70	0.62	0.62	0.56

Table 3.3: Correlation at $\tau = 0$ for sea state WS15

3.7.3. PREDICTION

The eventual aim of the simulation scenario is to predict in future time the elevation in the near-radar area. At each time t_0 during the simulation, the obtained reconstruction at that time, $P(t_0, \tau = 0)$ can be taken as initial state for a prediction according to equation (2.3), without additional updates.

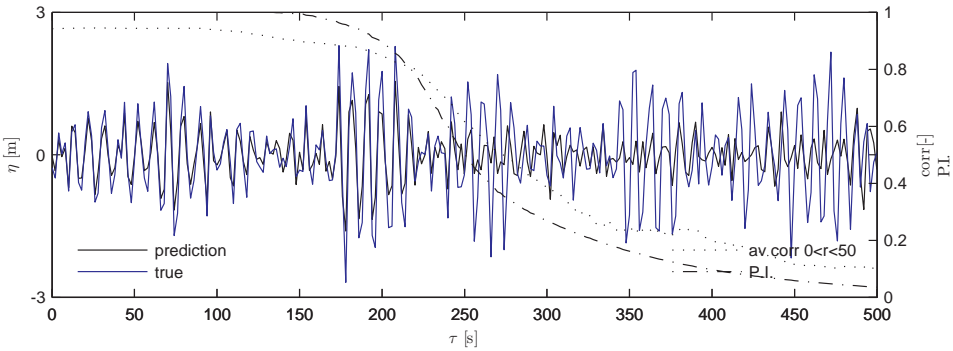


Figure 3.7: Predicted wave elevation using DAES and true wave elevation

Figure 3.7 shows an example of the predicted wave elevation and the true wave elevation at the antenna position against prediction time τ for a DAES simulation with sea state W15 and reconstruction method R^1 . (Also the correlation coefficient c (equation (3.28)) averaged over the latest 100 simulation time steps preceding the time of the sample prediction shown and the predictability indicator P.I. as defined in equation (3.17)

are shown.) Plots showing the correlation $corr$ for $r < 50$ against τ for simulations with the bimodal sea state WS15 using DAES are shown in figures 3.8 for perfect wave input ('Sea') and 3.9 for shadowed input using reconstruction method R^1 . (Correlation values drop below values that represent a practically useful accuracy at high prediction time τ , which is why in Figure 3.9 and further the τ axis is limited to 250 s.) Corresponding results with 3D FFT are shown in figures 3.10 and 3.11.

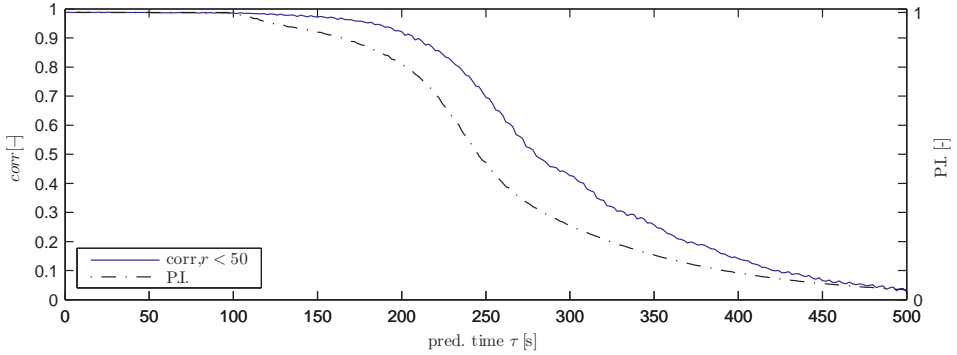


Figure 3.8: Corr of prediction with DEAS WS15 Sea

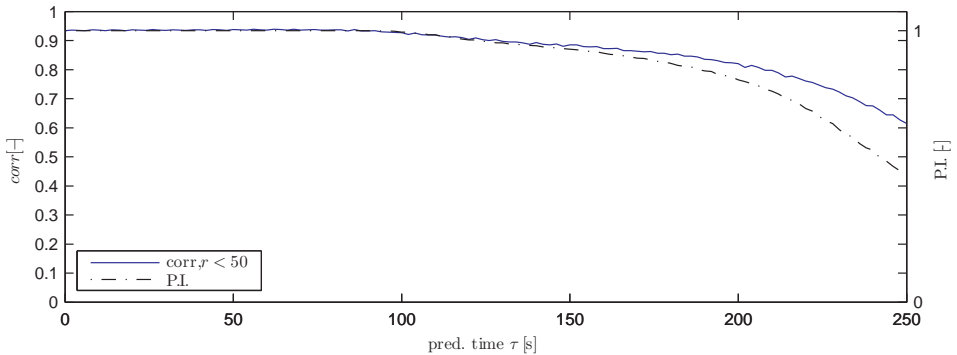


Figure 3.9: Corr of prediction with DEAS WS15 R^1

3.8. DISCUSSION OF RESULTS

3.8.1. RECONSTRUCTION METHOD

The vertical shifting method (R^1) does not improve the correlation of the individually reconstructed images as is reflected by the fact that for R^1 , 'Raw' and 'Rec' show identical correlation in table 3.2. This can be explained by the fact that a vertical shift and multiplication with a scalar (scaling factor α) as given in equation (3.7) does not affect the value of the correlation coefficient defined by equation (3.28). The remaining columns in table 3.2 and 3.3 show the mean correlation of the simulated *evolved* elevation and

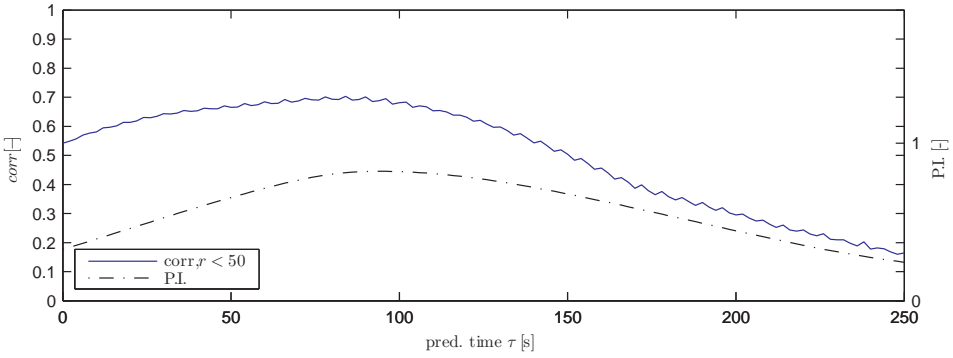


Figure 3.10: Corr of prediction with 3D FFT WS15 Sea

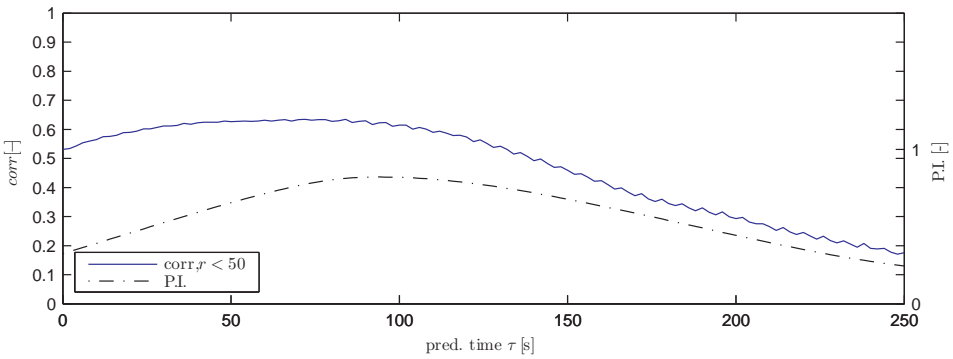


Figure 3.11: Corr of prediction with 3D FFT WS15 R¹

true elevation in the near-radar area ($r < 50$ and $r < 500$) and in the ring shaped observable zone only ($1800 > r > 500$). Here the results for reconstruction method 1 (R^1) and the R^0 results again hardly differ. The explanation for this is the fact that for evolutions with R^0 , as mentioned the 2D FFT component representing the average was taken 0 ($a(\mathbf{k} = (0, 0)) = 0$). This makes R^0 and R^1 virtually equivalent. A small difference can occur due to the fact that in R^1 the subtracted mean was taken over the part of the image outside the blind zone (as specified in equation 3.31), while setting $a(\mathbf{k} = (0, 0)) = 0$ in R^0 would be equivalent to subtracting the mean over the *entire* image.

The gain in accuracy due to the individual image reconstruction is very limited (nihil in case of R^1 as explained above) compared to what is achieved by the dynamic averaging: Using reconstruction method R^2 , for both investigated sea states W15 and WS15, the correlation of the individually reconstructed images ('Rec') has improved from 0.71 to 0.74 and from 0.70 to 0.72 respectively, whereas the correlation of the wave elevation in the near antenna zone, $r < 50$, which has been subjected to the dynamic averaging, shows a correlation value of 0.91 and 0.90 for these cases respectively.

For the prediction/reconstruction within 50 m from the antenna, it appears that neither reconstruction method R^1 nor R^2 preceding the DAES improves the final correlation (*corr*).

3.8.2. PREDICTABILITY

From e.g. figure 3.8 showing results for DAES applied to perfect non-shadowed waves ('Sea'), it can be seen that for large prediction time τ the correlation decreases. This can again be explained by the fact that beyond a certain prediction time, the fastest waves in the observation on which the prediction is based have passed the target location already: this is expressed by the value of *P.I.*, also plotted in the mentioned graphs, which starts to decrease from thereon. (It should be noted that the right-hand side axis associated with plotting *P.I.* is always scaled such that the value *P.I.* = 1 is at the same level as the value of the *corr* for $\tau = 0$ at left-hand side axis.) At a certain prediction time τ , *P.I.* has decreased until zero, meaning that even the slowest waves that were observed have passed the target location. It should be noted that *P.I.* is a qualitative indicator and not a quantitative one: a value of *P.I.* = 1 does not necessarily mean that we should expect a correlation of *corr* = 1; the actual correlation depends on many more parameters such as the quality of the observation and the prediction procedure. The main reason why *P.I.* is useful, is that it indicates from which value of τ the prediction accuracy will *certainly* decrease: both in this study and in chapter 2, a very clear match is found between the prediction time from where prediction accuracy starts decreasing (more drastically) and the prediction time from where *P.I.* starts decreasing. Therefore, for the maximum prediction horizon, the maximum value of τ can be taken for which *P.I.* is equal to one. In practice predictions will not be very relevant beyond a certain prediction time τ at which *P.I.* and consequently the accuracy have dropped significantly. In the specific cases presented here this prediction time is taken $\tau = 250s$ and in the remaining figures of predictions the maximum presented prediction time is limited to $\tau = 250s$.

As already explained in section 3.6, indicating the predictability in case of the 3D FFT approach is less straightforward than for DAES: Predictions from 3D FFT are based on multiple observations in time, while for DAES the prediction can be considered as the

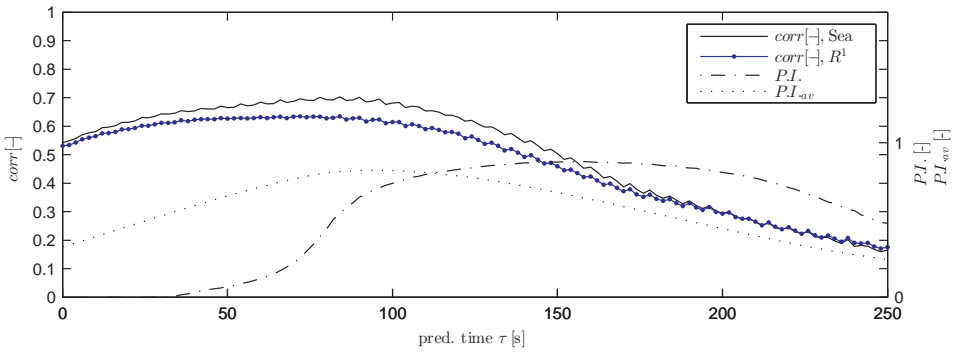


Figure 3.12: Predictability for 3D FFT approach

evolution of a single 'image' (though in itself, this 'image' results from dynamic averaging and evolution of many preceding observations). Figure 3.12 concerns a simulation with 3D FFT applied to perfect non-shadowed waves indicated by R^0 and shadowed waves indicated by R^1 , both sea state WS15. Predictability is indicated by both $P.I.$ (according to equation 3.26, so taking into account the effect of the blind zone ($r < r_0$)) and by $P.I._{av}$. It seems obvious that $P.I._{av}$ indeed better indicates the predictability: there is a more clear quantitative relation with the correlation found from the simulations. The initial increase in accuracy with increasing τ can be explained by the fact that indeed the shorter wave components need time to cross the near antenna blind zone, which is expressed by limiting the integration over ω to ω_h in equation (3.26).

3.8.3. DAES vs 3D FFT

In general it can be said that the proposed DAES yields far higher accuracy of the predicted wave elevation than the 3D FFT approach. Compare for example figure 3.9 with figure 3.11: Figure 3.9 shows that the correlation from DAES for $r < 50$ is 0.92 for all τ for which $P.I. = 1$, while 3.11 shows that a maximum correlation of only 0.62 is reached with 3D FFT.

3.8.4. SCALING

What also can be observed from figures 3.7 is that the variance of the predicted wave elevation decreases with increasing τ . This can be explained by the fact that for large values of τ , i.e. further into the future, the waves arriving at the antenna location originate from further distances from the antenna where the shadowing is more severe and the variance of the observation is lower (taking zero for shadowed regions). Using one scaling factor α based on the variance of the entire observed image and the true variance of the waves as was proposed in equation (3.7), does not take into account this decreased visibility at large ranges from the antenna and in fact does not even guarantee a correct variance at the antenna for $\tau = 0$. An alternative which is supposed to be practical and feasible for real life applications is proposed by Naaijen and Wijaya [2014]: a time history of the wave elevation at the antenna position (e.g. by an auxiliary wave buoy or via recorded ship motions) and a time history of the predicted wave elevation can be recorded and

used to calculate the variance of the true waves and the prediction. By taking the ratio of these variances, a scaling factor dedicated for the antenna location can be obtained. Such a scaling factor can also be computed as a function of τ , thus removing the aforementioned effect of decreasing variance of the prediction with increasing τ . Since in chapter 4, an alternative will be presented for the 2D FFT enabling to discard shadowed points instead of replacing them by zeros, the need for a τ -dependent scaling factor will be avoided which is why it is not addressed in detail here.

3

3.8.5. MED AND BIMODAL SEA STATE

In paragraph 3.5.2 it was explained how we propagate the wave components obtained from a 2D FFT in the mean evolution direction (MED). In case of multi modal sea states, it depends on the difference between the main propagation directions of the various modes how much of the total wave energy represented by the obtained components is propagated in the correct direction. The sea state WS15 was designed such, that the amount of energy represented by wave components propagating in opposite directions relative to the total wave energy, is very limited: less than 0.5 %. Differences in the obtained accuracy between W15 and WS15 can therefore only partly be explained by the limited capability of the MED method to cope with counter propagating waves occurring in the bi-modal seastate WS15.

3.9. CONCLUSIONS AND RECOMMENDATIONS

The main conclusion that can be drawn from the investigations presented in this chapter is that 3DFFT should be considered not to be suitable for the phase-resolved prediction of waves outside the observation area. The proposed DAES scenario where subsequent 2D FFT's are combined, yields a prediction accuracy that is significantly higher than what is achieved with 3D FFT. A limitation of the proposed DAES approach as presented here however is that it is not able to deal with counter propagating wave components which can occur in bi- or multimodal seastates. Furthermore it is concluded that the presented attempts to reconstruct individual images before using them as input for the DAES, do not improve the accuracy of the prediction of the wave elevation in the blind zone near the antenna and therefor will be omitted in the proceeding. It should be noted that the choice for the number of images used for the averaging $N_t = 3$ (see equation (3.13)) could be considered as rather arbitrary. Possibly more optimal choices for N_t can be made, likely to be depending on the wave period. An in depth investigation into optimization of N_t (as a function of the wave condition) could lead to improved and/or optimized accuracy in a wider range of wave conditions than the ones considered in this chapter and is therefore recommended. Concerning the averaging procedure represented by equation (3.14), the weighing factor w between the evolution and the new observation was taken 0.5. No in depth investigations into a potentially more optimal choice of w have been undertaken and are left as a recommendation.

4

MODELING AND INVERSION OF NORMALIZED RADAR CROSS SECTION

4.1. SUMMARY

This chapter will discuss a more realistic approach to nautical radar data and discuss its characteristics. An additional modulation mechanism known to radar images of ocean waves, being tilt modulation, will be introduced. Two methods to invert tilt modulated images into elevation will be presented and verified using synthetic radar images including tilt and shadowing, as opposed to Chapter 3, in which only shadowing was considered.

4.2. INTRODUCTION

The emphasis in the previous chapter, was on an assimilation procedure which updates the initialization of a linear wave model by continuously feeding in updated observation data. One step within the proposed assimilation procedure is solving the coefficients (or wave component / wave mode amplitudes) of the linear 2D wave representation, for which a 2D FFT was used as described in paragraph 3.5.2.

This chapter mainly focuses on alternatives for solving the coefficients. One of the reasons for this is that back scatter data from non-coherent radar may not be interpreted as something that linearly relates to the wave elevation but more realistically relates to the steepness of the waves in the look direction, which will be referred to as 'tilt'. This slightly complicates the solving of the coefficients from available observations as will be explained in more detail in paragraph 4.4.2.

Before further addressing the more realistic tilt model for back scatter data from non coherent radar, some recent efforts addressing the problem of solving coefficients of a linear 2D wave representation from spatio-temporal observation from various types of sensors are summarized.

Grilli et al. [2011] and Nouguier et al. [2014] report on an ocean wave reconstruction algorithm based on spatio-temporal surface elevation data acquired by a LIDAR camera. A least squares fit is applied to find the component amplitudes of a linear representation of the wave surface elevation, using observations from a spatial domain typically feasible with a LIDAR camera, which is significantly smaller than the spatial coverage of navigation radar. Additionally, non-linear dispersion effects are accounted for by iteratively solving for the optimal transformation involved with the so-called choppy wave model.

Connell et al. [2015] integrate the Doppler frequency shift obtained from fully coherent Doppler radar into a least squares problem, solving the coefficients of a linear 2D wave representation. This approach is very similar to the alternative suggested in paragraph 4.4.3. Main difference is that in case of a coherent Doppler radar, the observations are interpreted as the relative radial velocity of the wave surface, while in case of non-coherent radar, observations are interpreted as the steepness of the wave surface in radial direction.

Alford et al. [2014] also use radial velocity input from coherent radar to finally obtain a linear (and also non-linear) 2D wave field representation, but present a different approach for solving its coefficients: the radar data in polar coordinates is Fourier transformed and the time derivative of the velocity potential function is computed from which the surface elevation is derived through the dynamic free surface boundary condition. Contrary to the earlier mentioned research, this approach avoids the need of preliminarily associating wave numbers with frequencies by the dispersion relation and therefore the need of prior knowledge of the surface current.

None of these above mentioned references concerns observation of the sea surface by non-coherent radar. Therefore the modeling of the back scatter from the sea surface received by non coherent radar is presented in more detail in this chapter. Subsequently, given the presented model for the back scatter data, a description of two alternatives to obtain coefficients of a linear 2D wave representation from this data is given, being part of an assimilation procedure as described in chapter 3:

1. The first one naturally stems from and builds on the 2D FFT approach presented

in chapter 3 and will merely involve an additional processing step preceding the 2D FFT as is.

2. An alternative is presented which includes the inversion of tilt in a more direct way. Abandoning the 2D FFT approach, being part of the scenario used in chapter 3, this alternative comes with some important advantages:
 - Shadowed observation points can be omitted from the analysis since no spatially equidistant set of observation points is required.
 - Counter-propagating waves do not form a problem which makes the method applicable to arbitrary multi-modal sea states.

4.3. MODELING IMAGING OF SURFACE WAVES BY NON COHERENT RADAR

In the previous chapter shadowing was considered as the only modulation mechanism playing a role in imaging of ocean waves by nautical radar. For low grazing incidence, which is the case for most applications of wave sensing from ships, shadowing is indeed one of the dominant mechanisms (Wetzel [1990]). However, there is no physical argument to assume that back scatter recorded by a non-coherent nautical X-band radar has a direct relation to the surface elevation, as was done in the previous chapter. A more plausible approach is to assume it to be related to the local angle of incidence of the EM waves with the sea surface, as will be discussed in this chapter in more detail. Apart from the question which modulation mechanisms are relevant, their precise effect is not easily quantified. In other words: the obscure relation between the normalized radar cross section (NRCS)¹, and the sea surface elevation is a big challenge in the problem of wave sensing/prediction from non-coherent nautical radar. Nevertheless, numerous successful applications of nautical radar related to the measurement of gravity wave related parameters have been reported in literature: One and Two-dimensional wave spectra and significant wave height detection were obtained by Borge et al. [1999] and Borge et al. [2004]. Both Borge et al. [2004] and Dankert and Rosenthal [2004] attempt to obtain the actual surface elevation. A convincing validation of its accuracy is not presented. However, statistical distributions of crest heights, derived from the sea surface elevation by Borge et al. [2004] agree reasonably well with in-situ observations. Dankert and Rosenthal [2004] show accurate significant wave heights obtained from nautical radar, without using any reference observation.

An often used representation (see e.g. Velenzuela [1968], Alpers et al. [1981]) of radar backscatter from ocean waves is given by:

$$\sigma_0 = \bar{\sigma}_0 + \delta\sigma_0 \quad (4.1)$$

where σ_0 denotes the NRCS. A mean contribution to the NRCS due to Bragg scattering of the electromagnetic waves by the (wind induced) surface roughness is given by $\bar{\sigma}_0$ and an additional modulation $\delta\sigma_0$ is added due to the gravity waves which tilt the scattering sea surface.

Literature mentions various possible modulation effects caused by the waves, represented by $\delta\sigma_0$:

- shadowing
- hydromechanical modulation
- tilt modulation

The phenomenon of shadowing and an approach to minimize the effect of the resulting lack of observation data was addressed in chapter 3. As already mentioned in the

¹Radar cross section (RCS) can be considered as the 'detectability' of a scattering object by radar. In case of a large collection of scatterers, which the ocean surface is considered to be, the *normalized* RCS (NRCS) is used which can be considered as the RCS per unit surface area.

introduction of chapter 3, hydromechanical modulation is believed to be of minor importance. Besides, no straight forward approach to model or invert its effect is available. Tilt modulation is likely to be more relevant.

A commonly used model for the radar backscatter of ocean waves is the so-called 2-scale model of eq. 4.1. Indeed assuming tilt modulation as the relevant modulation mechanism, a linear representation for $\delta\sigma_0$ is given by Velenzuela [1968] and Alpers et al. [1981]:

$$\delta\sigma_0 = \left. \frac{\partial\sigma_0(\Theta, \psi, \delta=0)}{\partial \tan(\psi)} \right|_{\psi=0} \eta_r + \left. \frac{\partial\sigma_0(\Theta, \psi=0, \delta)}{\partial \tan(\delta)} \right|_{\delta=0} \left(-\frac{1}{r} \eta_\varphi \right) \quad (4.2)$$

Here ψ and δ are the local slope of the sea surface in the radar looking direction and perpendicular to this respectively and Θ is the local incidence or 'depression' angle as defined in figure 4.1. Λ as depicted in 4.1 is the antenna altitude above the mean sea surface.

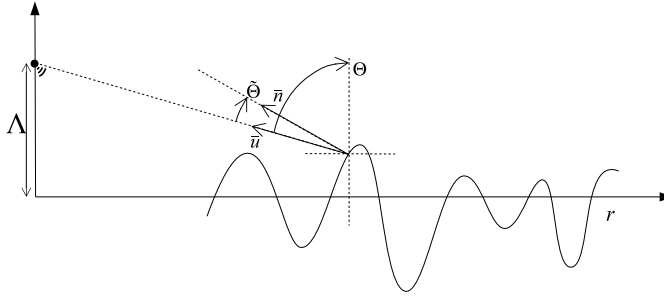


Figure 4.1: Tilt

In order to assess the derivatives in eq. 4.2, it is convenient to interpret $\delta\sigma_0$ as being related to what will be referred to as the 'tilt', the angle, $\tilde{\Theta}$, between the radar look direction, \vec{u} , and the normal to the sea surface, \vec{n} . They can be written as:

$$\vec{u}(r) = (-\sin\Theta(r), 0, \cos\Theta(r)) \quad (4.3)$$

and

$$\vec{n}(r, \varphi) = \left(-\partial_r \eta, -\frac{1}{r} \partial_\varphi \eta, 1 \right) \quad (4.4)$$

For $\tilde{\Theta}$ follows:

$$\cos(\tilde{\Theta}) = \frac{\vec{u} \cdot \vec{n}}{|\vec{u}| |\vec{n}|} = \frac{\sin\Theta \cdot \partial_r \eta + \cos(\Theta)}{\sqrt{(\partial_r \eta)^2 + \left(\frac{1}{r} \partial_\varphi \eta\right)^2 + 1}} \quad (4.5)$$

Linearizing for small wave steepness yields:

$$\cos(\tilde{\Theta}) \approx \sin\Theta \cdot \partial_r \eta + \cos(\Theta) \quad (4.6)$$

For the local incidence angle can be written:

$$\Theta = \tan^{-1} \left(\frac{r}{\Lambda - \eta} \right) \quad (4.7)$$

Linearizing for small wave amplitude yields:

$$\Theta \approx \tan^{-1} \left(\frac{r}{\Lambda} \right) \quad (4.8)$$

after which only the first term in eq. 4.6 depends on the surface gravity waves.

So assuming a linear dependence of $\delta\sigma_0$ on the *fluctuation* of $\cos(\tilde{\Theta})$ due to the surface waves, we could write:

$$\delta\sigma_0 = c \sin \Theta \cdot \partial_r \eta \quad (4.9)$$

where c is some constant.

Under these assumptions we could write for the derivatives in eq. 4.2:

$$\left. \frac{\partial \sigma_0(\Theta, \psi, \delta = 0)}{\partial \tan(\psi)} \right|_{\psi=0} = c \sin(\Theta) \quad (4.10)$$

and

$$\left. \frac{\partial \sigma_0(\Theta, \psi = 0, \delta)}{\partial \tan(\delta)} \right|_{\delta=0} = 0 \quad (4.11)$$

The second term in eq. 4.6 could be considered to introduce a range dependency of the mean part, $\bar{\sigma}_0$, of the total NRCS given by eq. 4.1 so we could write:

$$\bar{\sigma}_0 = \bar{\sigma}_{0B} + c \cos(\Theta(r)) \quad (4.12)$$

where $\bar{\sigma}_{0B}$ is the mean NRCS due to pure Bragg scattering and $c \cos(\Theta(r))$ is a modulation due to the variation of the local incidence angle.

Having available an observation of σ_0 , a logical first step for the inversion towards η is to eliminate the term $\bar{\sigma}_0$. This can be done by subtracting the mean of the (r and φ dependent) signal σ_0 , determined by calculating the average over a sufficiently long time history. After subtraction, the remainder is considered to equal $\delta\sigma_0$. From eq. 4.9 follows that from the obtained observation of $\delta\sigma_0$ the wave steepness in look direction can be determined:

$$\frac{\delta\sigma_0}{\sin(\Theta)} = c \cdot \partial_r \eta \quad (4.13)$$

As will be shown in the proceeding, the unknown constant c can be eliminated using a reference measurement.

[Dankert and Rosenthal \[2004\]](#) provide an elegant method to obtain the relation between observed NRCS and wave steepness that offers two advantages compared to the above mentioned approach:

1. it does not require any reference observation
2. it also works even if the relation between tilt and NRCS is not linear (as was assumed above).

Since the aim of this research is to use ship-mounted radar, it was decided to assume availability of a ship motion measurement, providing a convenient reference for determining the scaling constant c . This will be explained in more detail in chapter 5.

4.4. INVERSION METHODS FOR RADAR CLUTTER

In the following, basically two methods will be presented for inverting the NRCS into a wave elevation. To illustrate the methods, the constant Bragg-scattering contribution to the NRCS, $\bar{\sigma}_{0B}$ in equation 4.12 and the constant factor c in equation 4.12 and 4.9 will be assumed to be 0 and 1 respectively. (In the next chapter, dealing with actual field data from nautical radar, elimination of $\bar{\sigma}_{0B}$ and c will be considered.) For the principles of the inversion methods to be presented and their verification with synthetic data, it is not relevant to include these parameters here.

This means we are considering the inversion of what will be referred to as the 'synthetic NRCS', σ_{0s} , which equals $\cos(\tilde{\Theta})$ as given by equation 4.5:

$$\sigma_{0s} = \cos(\tilde{\Theta}) \quad (4.14)$$

This synthetic NRCS is *modeled* by the approximation given by equation 4.6:

$$\sigma_{0sm} = \sin(\Theta) \partial_r \eta + \cos(\Theta) \quad (4.15)$$

(with Θ as approximated by equation 4.8)

The first inversion method to solve η from equation 4.15 relies strongly on the methodology presented in chapter 3. The only difference of what will be presented in this chapter compared to chapter 3 is that an additional analysis step is introduced: a beam wise spatial integration of σ_{0s} is applied in order to find η , after which the obtained η can be subjected to a 2D FFT in order to find the amplitudes of the wave modes representing the 2D wave field. This approach will be referred to as '2D FFT' and will be described in more detail in paragraph 4.4.2.

Methods presented in previous chapters all rely on FFT techniques and consequently on equidistant observation data. Due to mainly shadowing or blockage of the radar beams by obstacles on board the ship, this equidistant observation data is generally not available in real life situations. Besides, nautical radar is a scanning type of radar: the antenna has a limited rotational speed meaning that radar images are in fact not spatial snapshots taken at one instant in time but rather a collection of beam-wise observations, each observed at its own instant in time. In paragraph 4.4.3, an alternative to the 2D FFT method is presented which will be referred to as 'least squares approach' (LSQ). The main advantages of this method are:

1. It can deal with an arbitrary collection of observation points each of whose actual location is used. Unlike methods involving spatial Fourier transformations, this method is not restricted to a equidistant Cartesian spatial grid. Therefore, unknown (e.g. shadowed) or unreliable observation points can be omitted from the analysis.
2. Since the observation points' actual recording time can be used in the analysis, no time interpolation in order to obtain spatial snapshots at one instant in time (as required for applying a 2D FFT, described in 4.4.2) are needed. Eventually introduced inaccuracies due to this interpolation, which can be expected to be more pronounced for slowly turning antennas and/or short waves, are avoided this way.
3. It can deal with counter propagating waves and therefore with arbitrary (multi-modal) sea states. There is no restriction on the propagation direction of the solved

wave modes: where waves propagating in directions deviating more than 90 degrees from the main evolution direction cannot be captured using the procedure described in chapter 3, the LSQ approach provides the freedom to solve waves propagating in arbitrary directions, thus enabling to handle multi-modal sea states with wave systems from arbitrary directions.

The main disadvantage of LSQ is the computational effort involved with solving the involved system of equations (given by equation 4.27).

Until now, surface current has not been considered. All investigations in chapter 3 were carried out with synthetic waves without surface current and for the simulations, zero current was assumed. For real field application though, a possible surface current has to be taken into account. Both inversion methods mentioned above rely on the dispersion relation for gravity waves which is affected by surface current. Since detection of spectrum and surface current are closely related, the next paragraph will be dedicated to these topics. It is acknowledged that current detection is an important part of a deterministic wave prediction procedure. However, in order to limit the scope of this research, detection of current has not been extensively studied and is only touched upon at an introductory level here. Actual investigations are left out of the scope of this thesis. After addressing spectrum and current detection in the next paragraph, a detailed description of the two mentioned deterministic tilt inversion methods will follow in the proceeding paragraphs of this section.

4.4.1. DETECTION OF DIRECTIONAL WAVE SPECTRUM AND CURRENT

In order to limit the scope of this research, detection of current has not been extensively studied. This paragraph merely presents a very brief introduction to the topic. For the purpose of wave propagation modeling in the proceeding, it will be assumed the surface current is known a-priori, or assumed to be zero.

Regarding wave spectrum, surface current (and water depth) detection, a general distinction can be made between so-called *local* and *global* methods. Basically, global methods can be used in case of sufficiently homogeneous wave fields, i.e. sufficiently flat sea bottom. In case of more pronounced bathymetry, spectrum and current will be less homogeneous and a local method is required. Since the objective of this research is to provide wave observation / prediction for *offshore* operation and since the used linear wave model is not capable of taking into account the effect of bathymetry in the first place, a global method is aimed for. (Local methods, yielding space dependent hydrographic parameters such as near-surface current, wave spectrum and bathymetry, are described by e.g. Hessner et al. [1999] and Senet et al. [2008].)

Young et al. [1985] is the oldest reference to the 3D FFT approach that forms the basis of most global methods for directional wave spectrum and surface current detection. Modifications to this basic approach have been made by Senet et al. [1997] and Senet et al. [2001] who use an iterative method and error model to take into account the non-linear imaging mechanism due to shadowing and aliasing resulting from temporal undersampling due to the limited rotational antenna speed. Serafino et al. [2010] has adapted the dispersion filtering by introducing an approach based on maximization of normalized scalar product of the filtered 3D image spectrum and a characteristic function identifying a narrow band-width around the linear dispersion shell in the 3D wave-vector - fre-

quency space, a method yielding more accurate current estimation especially for larger encounter frequencies, resulting from vessel speed.

The most basic method for current and spectrum detection will be presented here which is practically equivalent to the first iteration of the iterative method presented by [Senet et al. \[1997\]](#).

Let $a(\mathbf{k}, \omega)$ be the 3D amplitude spectrum obtained from the discrete 3D Fourier transform of σ_{0s} in a similar way as was done with the images R in equations 3.19 and 3.21 in section 3.6.

The 3D variance spectrum, one-sided with respect to the ω -axis can be defined as:

$$S(\mathbf{k}, \omega) = |a(\mathbf{k}, \omega)|^2 \quad (4.16)$$

In order to increase the confidence level for the variance spectrum obtained this way, averaging over time can be applied: $S(\mathbf{k}, \omega)$ is determined for (possibly overlapping) subsequent time series of radar images and the result is averaged over the number of time series N_{av} :

$$S_{av}(\mathbf{k}, \omega) = \frac{1}{N_{av}} \sum_{i=1}^{N_{av}} S_i(\mathbf{k}, \omega) \quad (4.17)$$

where S_{av} is the average 3D variance spectrum and S_i is the 3D variance spectrum obtained from the time series of realization i .

Following [Young et al. \[1985\]](#), the surface current can be found by fitting the dispersion shell through the obtained average 3D variance spectrum. The dispersion relation including surface current is defined as:

$$\Omega(\mathbf{k}, \bar{U}) = \sqrt{|\mathbf{k}|g \tanh(|\mathbf{k}|h)} + \mathbf{k} \cdot \bar{U} \quad (4.18)$$

where \bar{U} is the 2D surface current vector.

Using the average 3D variance spectral values as weighing factors, solving the following minimization problem leads to the detected 2D current vector \bar{U}_{av} :

$$\bar{U}_{av} = \min_{\bar{U}} \sum_{i=1}^I S_{av}(\mathbf{k}_i, \omega_i)^{w_p} |\omega_i - \Omega(\mathbf{k}_i, \bar{U})|^2 \quad (4.19)$$

Here, I defines the number of spectral coordinates that are used to fit the dispersion shell by solving the minimization problem represented by equation 4.19, w_p is a weighing factor for the energy assigned to each component $S_{av}(\mathbf{k}_i, \omega_i)$. $w_p = 0$ represents the option of no energy weighing. ω_i is the frequency associated with spectral coordinate i . Selecting the appropriate I spectral fitting coordinates is an important part of the procedure and is treated in e.g. [Senet et al. \[1997\]](#).

Once the surface current is known, a procedure referred to as 'dispersion filtering' as described in paragraph 3.6 can be applied in order to obtain the 2D spectrum. The main purpose of this is to give more physical meaning to the 3D variance spectrum by eliminating effects due to measurement noise and spectral leakage. Dispersion filtering attempts to maintain only the physical gravity wave related information contained

by the average 3D variance spectrum. The average 2D variance spectrum obtained by dispersion filtering is defined as:

$$S_{av}(\mathbf{k}) = \sum_{\omega} f(\mathbf{k}, \omega) S_{av}(\mathbf{k}, \omega) \quad (4.20)$$

where f represents a filtering factor as defined by equation 3.25.

The *normalized* average 2D spectrum, S_{avn} , is obtained by ensuring the total variance it represents to be 1:

$$S_{avn}(\mathbf{k}) = \frac{S_{av}(\mathbf{k})}{\int_{-\infty}^{\infty} S_{av}(\mathbf{k}) d\mathbf{k}} \quad (4.21)$$

4.4.2. 2D FFT PRECEDED BY BEAM-WISE SPECTRAL INTEGRATION ('2DFFT')

This paragraph presents the first of the two proposed methods to obtain wave component amplitudes for a 2D linear wave representation from radar data assuming the model given by equation (4.15). Let the 2D linear wave representation be given by:

$$\eta(\mathbf{x}, t) = \text{Re} \left(\sum_{n=1}^N a(\mathbf{k}_n) e^{i(\mathbf{k}_n \mathbf{x} - \Omega(\mathbf{k}_n) t)} \right) \quad (4.22)$$

In cylindrical coordinates this becomes:

$$\eta(r, \varphi, t) = \text{Re} \left(\sum_{n=1}^N a(\mathbf{k}_n) e^{i(|\mathbf{k}_n| r \cos(\varphi - \theta_n) - \Omega(\mathbf{k}_n) t)} \right) \quad (4.23)$$

Here, \mathbf{k} is again the 2D wave vector with θ the wave propagation direction:

$$\mathbf{k} = |\mathbf{k}| (\cos(\theta), \sin(\theta))$$

Subsequently, for $\partial_r \eta$ can be written:

$$\partial_r \eta(r, \varphi, t) = \text{Re} \left(\sum_{n=1}^N i |\mathbf{k}_n| \cos(\varphi - \theta_n) a(\mathbf{k}_n) e^{i(|\mathbf{k}_n| r \cos(\varphi - \theta_n) - \Omega(\mathbf{k}_n) t)} \right) \quad (4.24)$$

In equation 4.24, the dependence of the part before the exponent on the look direction φ prevents the tilt to be represented by a 2D FFT representation with look direction independent coefficients and as a consequence, the tilt cannot be represented by a representation whose coefficients can be directly obtained by a 2D FFT.

A first and logical way to obtain the solved wave elevation, directly related to the 2D FFT approach presented in paragraph 3.5.2, is to eliminate Θ from the observed σ_{0sm} and apply a spatial integration over r preceding the 2D FFT:

$$\partial_r \eta(r, \varphi) = \frac{\sigma_{0s}(r, \varphi) - \cos(\Theta(r))}{\sin(\Theta(r))} \quad (4.25)$$

To obtain η , a beam-wise spectral integration is used: for each separate beam in the radar image, a 1D FFT is applied to $\partial_r \eta$ with respect to r . With the Fourier transformed $\partial_r \eta$ denoted by $\hat{\eta}_r$, the wave elevation on one beam can be expressed by:

$$\eta(r, \varphi) = \sum_{k_{||}} (ik_{||})^{-1} \hat{\eta}_r(k_{||}, \varphi) e^{i(k_{||}r)} \quad (4.26)$$

where $k_{||}$ is the wave number projected in the look direction (φ) of the considered beam. This way η can be obtained for each radar image first, after which the exact same procedure as described in chapter 3 can be applied.

One aspect that was not addressed in chapter 3 but which is relevant for the 2DFFT approach is the fact that the scanning beam of a nautical radar rotates with a limited angular speed. Consequently, each beam is recorded at a different instance in time: in equation 4.25, φ is a function of time. In order to obtain all recorded data within one radar image for one specific instance in time, a linear interpolation using the preceding and the following image is applied. (Usually the data is interpolated towards the time associated with the so-called Azimuth Reset Pulse (ARP), usually the time when the radar scanner points to the bow of the vessel.) Let this time be indicated by t_{00} and let the time elapsed between subsequent instants of t_{00} (the rotation period of the antenna) be indicated by dt . During an antenna revolution, let a beam in a certain look-direction φ be recorded Δt after the t_{00} associated with the considered revolution. Assuming constant rotation speed for the sake of this explanation, the data value associated with look direction φ at time t_{00} is obtained by linear interpolation over time between the value for $t_{00} + \Delta t - dt$ and the value for $t_{00} + \Delta t$.

In the following, this interpolation is referred to as 'helical interpolation'.

4.4.3. LEAST SQUARES APPROACH

This paragraph presents the second approach to solve the wave component amplitudes replacing the '2DFFT' approach as described in the previous paragraph. The alternative will be a least squares minimization, referred to as 'LSQ'.

LSQ solves a predetermined number of wave modes (linearly superposed wave components). In order to minimize the computational effort, the modes to be solved are based on the normalized average 2D wave spectrum. This normalized 2D wave spectrum, as well as possible surface current need to be known a priori. This means that a 2 stage approach is proposed:

1. detect the directional wave spectrum and surface current by 3D FFT as presented in paragraph 4.4.1 and select the most energetic wave vectors
2. apply a least squares minimization, in order to find the amplitudes of the wave components for the set of 2D wave numbers that was selected based on the directional wave spectrum

LEAST SQUARES MINIMIZATION (LSQ) AS ALTERNATIVE TO 2D FFT

In order to obtain the complex wave mode amplitudes, $a(\mathbf{k}_n)$, equation 4.24 can be equaled to equation 4.25 containing the 'observed' σ_{0s} , yielding the following minimization problem in order to solve for the unknown complex wave components $a(\mathbf{k}_n)$:

$$\bar{a} = \min_{\mathbf{a}} \|\text{Re}(\mathbf{A} \cdot \mathbf{a}) - \mathbf{b}\|^2 \quad (4.27)$$

where matrix \mathbf{A} consists of elements A_{nm} defined as:

$$A_{nm} = i |\mathbf{k}_n| \cos(\varphi_m - \theta_n) e^{i(|\mathbf{k}_n| r_m \cos(\varphi_m - \theta_n) - \Omega(\mathbf{k}_n) t_m)} \quad (4.28)$$

Vector \bar{a} contains the complex wave mode amplitudes $a(\mathbf{k}_n)$ and the elements b_m of vector \mathbf{b} are defined as:

$$b_m = \frac{\sigma_{0s}(r_m, \varphi_m, t_m) - \cos(\Theta(r_m))}{\sin(\Theta(r_m))} \quad (4.29)$$

The observation points b_m and corresponding rows in matrix \mathbf{A} are not necessarily taken from one antenna revolution but can originate from several revolutions. Only visible points are selected, i.e.: $\chi(r_m, \varphi_m, t_m) = 1$ with χ the characteristic visibility function as defined in equation (3.4).

ADAPTED DAES

As mentioned, LSQ is integrated in a procedure whose principle idea is that of DAES, as presented in chapter 3. This paragraph describes this integration.

Initializing the DAES scenario at $t = t_0$, let \bar{a}_0 be the solution of minimization problem 4.27 at t_0 , where observations b (eq. 4.29) are obtained from N_t images preceding t_0 , only selecting visible points. The vector of observation points used to solve \bar{a}_0 will be referred to as \bar{b}_0 , containing elements $b_{m0}(r_{m0}, \varphi_{m0}, t_{m0})$. For the next iteration of the evolution scenario, say at t_1 , an updated series of N_t images (possibly partly overlapping with the series used for solution \bar{a}_0) is used in combination with the evolution of solution \bar{a}_0 to $t = t_1$. The solution at $t = t_0$ is evolved towards the time t_{m1} corresponding to each of the new observation points according to equation 4.24, resulting in $\partial_r \eta_1$:

$$\partial_r \eta_1 = \partial_r \eta(r_{m1}, \varphi_{m1}, t_{m1}) = \operatorname{Re} \left(\sum_{n=1}^N i |\mathbf{k}_n| \cos(\varphi_{m1} - \theta_n) a_0(\mathbf{k}_n) e^{i(|\mathbf{k}_n| r_{m1} \cos(\varphi_{m1} - \theta_n) - \Omega(\mathbf{k}_n) t_{m1})} \right) \quad (4.30)$$

The set of spatial co-ordinates (r_{m1}, φ_{m1}) is in general not equal to (r_{m0}, φ_{m0}) since different regions will be shadowed at different instants in time and the vessel may have moved in between.

Having available the evolved solution from t_0 , contrary to equation 4.29 (which only yields for initialization of the scenario), b_{m1} is obtained by combining this evolution with the newly observed σ_{0s} in a similar way as was done in chapter 3 (equation 3.14):

$$b_{m1} = \left(w \cdot \partial_r \eta_1 + (1 - w) \cdot \frac{\sigma_{0s}(r_{m1}, \varphi_{m1}, t_{m1}) - \cos(\Theta(r_{m1}))}{\sin(\Theta(r_{m1}))} \right) (1 - \chi_{rad}) + \partial_r \eta_1 \chi_{rad} \quad (4.31)$$

Solving the minimization problem again now using 'observations' b_{m1} yields solution \bar{a}_1 corresponding to time t_1 .

b_{m2} is obtained by combining the solution \bar{a}_1 (evolved from t_1 to t_2) and observations at t_{m2} etc.

4.5. SIMULATIONS WITH SYNTHETIC DATA

In order to verify and compare the two approaches for deterministic prediction from radar back scatter proposed in this chapter, simulations using synthetic data were carried out. This section will describe the simulations, and present and discuss their results. The approach is very similar to that was done in chapter 3: synthetic waves are created and the corresponding radar images are constructed. The latter are used as input for the two proposed alternatives for deterministic wave prediction. The obtained wave prediction can finally be compared to the originally synthesized waves.

In the following, the set-up of the simulations will be described (paragraph 4.5.1 and 4.5.2), followed by simulation results. The deterministic prediction results with the two proposed approaches will be presented in paragraph 4.5.3.

As explained, in case of the LSQ approach an estimation of the average directional wave spectrum is required in order to select the most relevant wave modes. Therefore, results from simulations concerning spectrum estimation are presented in paragraph 4.5.4.

4.5.1. WAVE CONDITIONS AND SYNTHETIC RADAR DATA

The objective in this chapter is to present a comparison between the two proposed alternatives for solving the wave component amplitudes, rather than just illustrating their principles. Since the results obtained with one alternative or the other are likely to depend on the wave condition, a range of different wave conditions is considered. The considered conditions are summarized in table 4.1

Condition	H_s [m]	T_p [s]	γ [-]	θ_{main} [deg]	s [-]
1	1.65	5.0	3	0	10
2	3.0	9.0	3	0	10
3	4.8	13.0	3	0	10
4	3.0, 3.0	9.0, 16.0	3, 10	0, 170	10, 50

Table 4.1: Wave conditions for synthetic simulations

For all cases, water depth $h = 1000$ was used for the synthetization of the waves. Radar images were synthesized in a similar way as was done in chapter 3 concerning the shadowing effect. A radar antenna height Λ above the free surface of 15 m was used. Additionally the effect of tilt was included: the synthetic images were created according to the exact (and non-linear) formulation of equation (4.5), representing the modulation term in equation (4.1). (As mentioned, the constant term was not included in the synthetization.) For the synthetization of the radar data, an antenna height Λ above the sea surface of 15 m was used. For all considered unimodal conditions, i.e condition 1-3, the significant wave height was chosen such that it resulted in an as equal as possible 'visibility', i.e. the average percentage of shadowed points was aimed to be the same. Figure 4.2 shows the percentage of shadowing against range r from the antenna for conditions 1-3.

Anticipating the validation study using field data, to be presented in the next chapter, an antenna rotation speed was used that is identical to that of the radar system aboard the

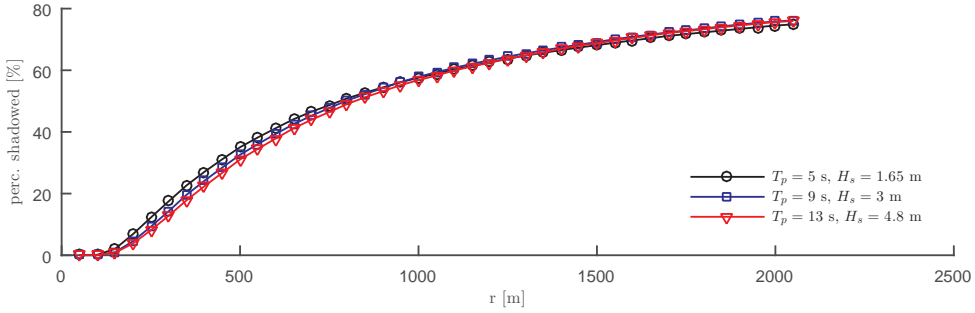


Figure 4.2: Percentage of shadowed points against range r for wave conditions 1-3

vessel used during the field campaign, being 44 rotations per minute. The used range and azimuth resolution were set to 7.5 m and 0.5 deg respectively, both corresponding to realistic values for navigation radar systems. A blind zone around the antenna of 300 m was applied. Table 4.2 summarizes the simulated radar system specifications used to synthesize the radar data.

Λ	Antenna height [m]	15
rpm	Antenna revolutions per minute	44
dt	Antenna rotation time [s]	1.36
$\Delta\varphi$	Azimuth resolution [deg]	0.5
Δr	Range resolution [m]	7.5
r_0	radius of blind zone [m]	300
r_{max}	outer radius of image [m]	1250

Table 4.2: Radar specs for synthetic simulations

4.5.2. SIMULATION SETTINGS

CHOICE OF OBSERVATION POINTS AND WAVE MODES

A great advantage of using nautical radar as a wave observer is the spatial coverage and resolution it can provide: typically a range of 1-3 km can be achieved at a range resolution of 3-10 m. The azimuth resolution can be in the range of 0.05 - 0.3 deg. Depending on the sea-state, this wealth of spatial information can be rather abundant, especially at close range r from antenna where the mentioned azimuth resolutions result in a high density of available observation points. In chapter 3 a Cartesian spatial grid with $dx = dy = 7.5$ m was used towards which the (synthesized) radar data was interpolated, thus decreasing the amount of data to be processed. This would allow for the detection of waves of 15 m minimal length. This is considered to be sufficient for generally occurring sea-states. Moreover, shorter waves are not likely to be relevant in terms of excitation for 1st order motions of offshore vessels.

The set of wave vectors \mathbf{k} corresponding to a 2D FFT applied to the chosen spatial grid

are given by:

$$\mathbf{k} = \left(n \frac{2\pi}{N \cdot dx}, m \frac{2\pi}{M \cdot dy} \right) \quad \text{with } n \in [0, N/2] \quad \text{and} \quad m \in [0, M/2] \quad (4.32)$$

M and N are the number of observation points in x and y direction of a rectangular observation domain respectively. In principle, the LSQ approach provides the freedom to choose any set of wave vectors whose corresponding amplitudes can be solved. Given the limitation that, in order to limit the computational burden of solving the minimization problem of equation (4.27), we are solving a pre-set number of wave components, different wave conditions will lead to different ideal resolutions of the wave vector. However, it was decided to fix the wave vectors: for all cases to be presented, the wave vectors \mathbf{k} of the components to be solved with LSQ were chosen from the set of wave vectors according to equation 4.32 (which is equal to the set of wave vectors corresponding to a 2DFFT). For LSQ, of this set of wave vectors, a set of 1500 components is selected representing a maximum amount of energy according to the supposedly known 2D wave spectrum.

The two steps involved in the LSQ approach (spectrum detection and deterministic solving of the wave modes) are addressed separately in this section: in the simulations, the most relevant modes to be solved are selected based on the exact 2D wave spectrum. Separate simulations address the detection of the spectrum itself. The exact 2D spectrum $S(\omega, \theta)$ is the spectrum on which the synthesized waves were based as described in paragraph 3.4.1. In order to select the most relevant components from the total wave vector space as defined in 4.32, $S(\omega, \theta)$ is transformed from the polar (ω, θ) -base to the Cartesian $\mathbf{k} (= (k_x, k_y))$ -base and normalized:

$$S(\mathbf{k}) = S(\omega, \theta) \cdot \frac{v_g(\omega)}{|\mathbf{k}|} \quad (4.33)$$

$$S_n(\mathbf{k}) = \frac{S(\mathbf{k})}{\int_{\mathbf{k}} S(\mathbf{k}) d\mathbf{k}} \quad (4.34)$$

where $\frac{v_g(\omega)}{|\mathbf{k}|}$ represents the Jacobian involved with the transformation, v_g being the group speed. S_n refers to the *normalized* spectrum.

In practice, for LSQ, the used observation points do not necessarily have to be part of a rectangular or square spatial domain: any arbitrary set of points can be used. However, for all presented results, a square domain is used with the observation points and wave modes chosen as above. Additionally, a window function is applied which tapers the values of the used observation points to zero outside a chosen radius r_{max} of a circular domain centered around the antenna, similar as described in paragraph 3.7.1.

Solving the linear system resulting from equation (4.27) was done using a graphical processing unit (GPU). Because of the computational cost of the LSQ approach and the limited memory of the GPU, both the number of modes to be solved and the amount of observation data used was limited. In order to be able to use data from several subsequent antenna revolutions, the amount of used observation data per revolution was decreased as compared to the 512 x 512 spatial grid used in chapter 3: the spatial grid size was chosen to measure 360 x 360 points. The radius of the blind zone, r_0 was chosen to be 300 m and the maximum range was set to $r_{max} = 1250m$.

SOLUTION UPDATE RATE

The number of radar images used per update, N_t as defined in paragraph 3.5.3 was set to 5 for the 2DFFT approach. The same number was chosen for the number of images used to extract the observation data from for the LSQ approach: N_t as defined in paragraph 4.4.3 is set to 5 as well. Due to the memory limitation of the GPU, there is a trade-off between maximum range and number of images from which observation data is used (and the number of modes to be solved). In depth investigations into optimizing this trade-off, which is again likely to be depending on the wave condition, have not been undertaken.

The chosen N_t for the 2D FFT approach is not claimed to be optimal either. In order to assess the effect of N_t , a small sensitivity study will be presented further on in this paragraph in which N_t was varied.

Since no overlapping data was used in subsequent solution updates and no data was skipped, the time between each prediction update is $5dt$. As a consequence, for a chosen distinct value of prediction time τ , say 30 s into the future, the simulation results in subsequent updates of the wave prediction at $\tau = 30$ that are $5dt$ apart.

In paragraph 3.5.4, equation (3.16), P was defined as the wave prediction as a function of prediction time τ obtained from a solution update corresponding to time t_0 . P refers to a spatial snapshot of the wave field in the used spatial domain involved with the 2D FFT. Let P_0 now refer to the point of P corresponding to the antenna position. The equivalent of P_0 obtained with the LSQ approach can be constructed by substituting the solved wave mode amplitudes at update time $t = t_u$, referred to as a_u into equation 4.23:

$$P_0(t_u, \tau) = \text{Re} \left(\sum_{n=1}^N a_u(\mathbf{k}_n) e^{i(|\mathbf{k}_n|r \cos(\varphi - \theta_n) - \Omega(\mathbf{k}_n)(t_u + \tau))} \right) \quad (4.35)$$

Generally $r = 0$ can be substituted for the antenna position.

$P_0(t_0, \tau)$, obtained with solution a_0 refers to the very first update of a simulation, $P_0(t_1, \tau)$ obtained with solution a_1 to the second, etc, all such that $t_u = t_{u-1} + 5 \cdot dt$.

4.5.3. RESULTS AND DISCUSSION DETERMINISTIC PREDICTION

As explained in paragraph 4.5.2, a simulation will yield time traces of the prediction for distinct values of prediction time τ whose temporal resolution amounts to $5dt$. In order to increase this time resolution, time traces were created by concatenating the values $P_0(t_u, \tau + m \cdot dt)$, with $m \in \{0, 1, 2, 3, 4\}$ and $\{u \in \mathbb{Z} | u_{\min} \leq u\}$. Here u_{\min} corresponds to the time at which all (including the shortest) waves have crossed the blind zone with radius r_0 . This means that a thus created time trace for a chosen prediction time value τ is constructed not only from actual values for τ from subsequent updates, but also values for up to $\tau + 4dt$. Time traces at the antenna position for a chosen prediction time value τ created this way, are denoted by $P_0(t, \tau)$ where t now refers to the absolute time. Of $P_0(t, \tau)$, the accuracy can be determined by correlating it with the originally synthesized wave elevation at the antenna, $\eta(\mathbf{x} = 0, t)$:

$$\text{corr}(\tau) = \frac{\langle P_0(t, \tau), \eta(\mathbf{x} = 0, t) \rangle}{|P_0(t, \tau)| |\eta(\mathbf{x} = 0, t)|} \quad (4.36)$$

Figures 4.3 and 4.4 present this correlation $corr$ as a function of prediction time τ for wave condition 1-3, together with the predictability indicator $P.I.$ (the latter based on the theoretical wave spectrum which was used to synthesize the simulation data). (Figures B.1(a), B.1(b) and B.1(c) in Appendix B present the same results in separate figures per wave condition, each of which containing results for the 2 different approaches, enabling easier comparison between the approaches.)

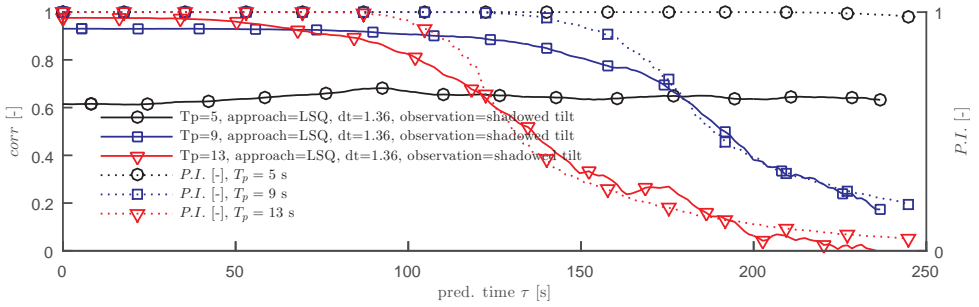


Figure 4.3: Correlation of predicted wave elevation at the antenna for conditions 1-3 obtained with LSQ

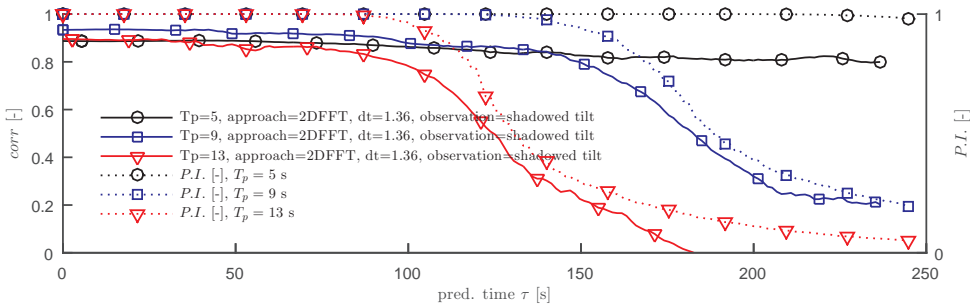


Figure 4.4: Correlation of predicted wave elevation at the antenna for conditions 1-3 obtained with 2DFFT and spectral integration

One of the things that can be seen from the result is that $P.I.$ again proves to be a fairly good qualitative indicator for the prediction accuracy as a function of prediction time τ . However, compared to results presented in chapter 3 a more pronounced decrease in correlation can be observed also for the part of the prediction time where $P.I. = 1$. As mentioned, the 2DFFT approach presented here is identical to the approach presented in chapter 3, except for the fact that:

- a preceding beam-wise integration is included here in order to invert the tilt effect while tilt wasn't addressed in chapter 3
- the helical interpolation was applied to map all data during one antenna revolution to one instance in time (whereas in chapter 3 no antenna speed was taken

into account: snap shots with constant recording time were generated by the synthetization).

- in order to enable fair comparison between 2DFFT and LSQ results in this chapter, the outer radius of the radar images, r_{max} was chosen 1250 m for both cases, while in chapter 3 this was 1800 m.

(Moreover, it should be noted that an antenna revolution period dt of 2.0 s was used in chapter 3 while here $dt = 1.36$ s.)

Concerning the second item mentioned above, it was observed from comparison to additional simulations where antenna speed was ignored that it had little to none effect on the correlation. The helical interpolation can become an issue though under different circumstances as will be addressed further on in this paragraph. In order to assess the effect of the third item above, simulations were carried out using synthetic data without tilt for which rotation speed of the antenna was ignored (as was done in chapter 3) and with a decreased r_{max} of 1250 m. Results showed a correlation drop at lower prediction time τ , as can be expected based on predictability theory, but exactly the same correlation for low τ as simulations with the large $r_{max} = 1800$. The effect of first item, the tilt, will be discussed in the next sub-paragraph.

EFFECT OF TILT

In general, for both the 2DFFT and the LSQ approach, slightly lower maximum level and faster decrease with increasing τ of the correlation was found when the observation data included the tilt effect. This is illustrated more clearly by figure 4.5 and 4.6 which show the correlation obtained with LSQ and 2DFFT respectively for condition 2, both for the case that the tilt effect was omitted (in the synthetization of the data and in the analysis) (black, circular markers) and for the case that it was included (blue, square markers).

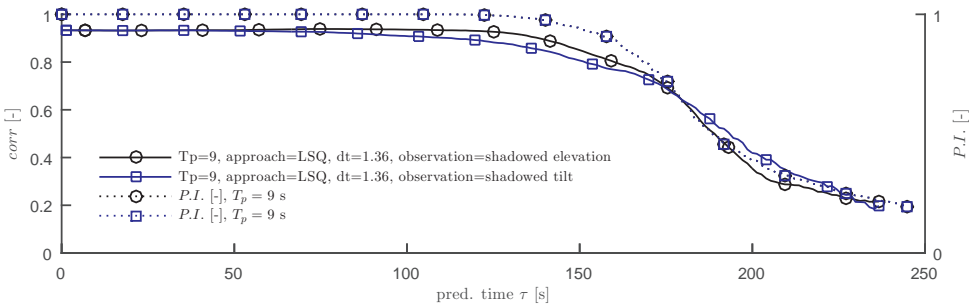


Figure 4.5: Correlation of predicted wave elevation at the antenna obtained with LSQ for conditions 2, comparing situation with and without tilt

A good explanation for this has not been found.

COMPARISON OF RESULTS BETWEEN DIFFERENT WAVE CONDITIONS FOR 2D FFT APPROACH

Another observation from figure 4.4 is that the condition with the shortest peak period (condition 1) appears to be more challenging in terms of prediction accuracy than con-

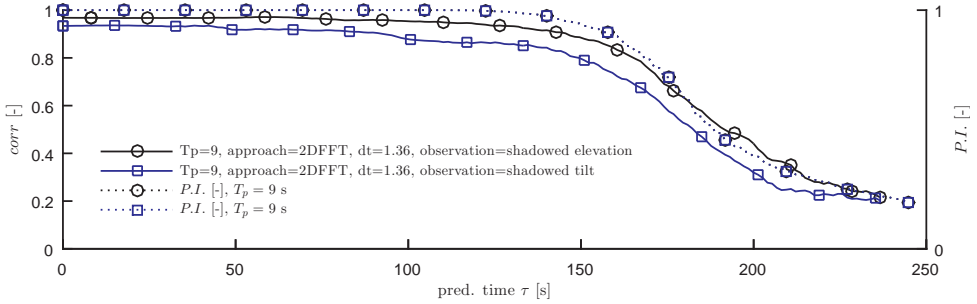


Figure 4.6: Correlation of predicted wave elevation at the antenna obtained with 2DFFT for conditions 2, comparing situation with and without tilt

4

dition 2. Condition 3 however, although involving the longest waves, shows a lower correlation than condition 2.

In general it can be expected that the decrease in accuracy with increasing propagation time or distance is related to the wave properties in terms of some characteristic period or length. Therefore a faster decrease in accuracy with increasing τ can be expected for the shorter wave condition. This however, is hardly reflected by the simulation results. More obvious is a difference in the *level* of the correlation, starting at $\tau = 0$ (the nowcast), rather than in its rate of decrease with increasing τ . It could be argued that for a shorter wave condition, the waves undergo more assimilation updates in the DAES procedure while they travel through the observation domain since their propagation speed is lower, which should even result in a higher accuracy for shorter waves. On the other hand, for shorter waves, the relative propagation distance (relative to the peak wave length e.g.) through the blind zone, where no new information is added from any observations before the waves arrive at the antenna position, is longer. This would explain a lower accuracy for shorter waves. The separate and joint effects of these mentioned (and possibly more) factors are not easily quantified or explained and no further attempts are done in pursuit of a sound explanation for this aspect of the observed results for now.

COMPARISON OF RESULTS BETWEEN DIFFERENT WAVE CONDITIONS FOR LSQ APPROACH

The differences between the results for wave conditions 1-3 obtained with LSQ as observed in figure 4.3 are much more pronounced. This can be explained as follows: Very obvious from the presented results is the fact that for the short wave period (condition 1, $T_p = 5$), the correlation obtained with the LSQ approach is much lower than for the 2DFFT approach, while with increasing wave period, the accuracy with LSQ increases and exceeds the 2DFFT accuracy for condition 3 ($T_p = 13$). The main reason for a low accuracy for short wave period using LSQ, is the limited amount of energy that is represented by the 1500 components chosen to represent the wave field. For the case of condition 1, 1500 wave components (chosen from the set of wave vectors as described in paragraph 4.5.2, such that together they represent a maximum amount of wave energy according to the theoretical spectrum) represent only 51% of the total spectral energy. For condition 2 and 3 this is 89% and 95% respectively. The 'footprint' of a Jonswap

spectrum in the wave vector space is apparently much larger for shorter peak periods. Figure 4.7 shows the normalized wave spectrum for condition 1. The contour tightly surrounding the selected 1500 components is shown by the solid white line.

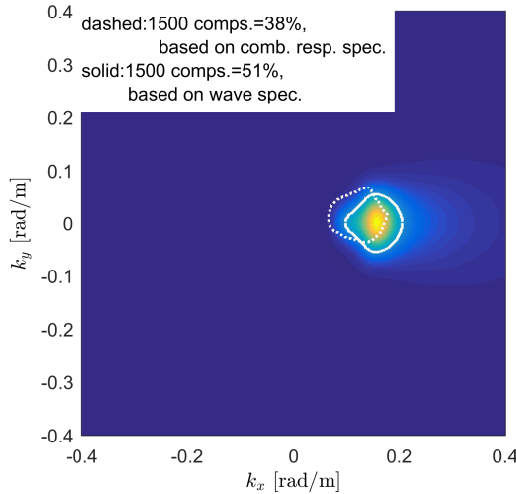


Figure 4.7: 2D wave spectrum of wave condition 1, with indications of the partitions represented by 1500 components based on the wave spectrum and the combined response spectrum

EFFECT OF MOTION TRANSFER FUNCTIONS

Although the found correlation obtained with the LSQ approach for condition 1 is too low for the wave prediction to be useful from a practical point of view, it doesn't necessarily mean that LSQ should be entirely rejected in case the chosen number of wave modes represents a (too) limited fraction of the total wave energy. Keeping in mind that in many practical cases it is the motions of the ship that are of interest rather than (just) the waves, we might be 'saved' by the fact that in general a ship will act as a low pass filter on the incoming waves: under the linear assumptions which allow to adopt the superposition principle, the effect of the (mostly short) waves that are not covered by the e.g. 1500 components chosen to represent the waves of condition 1 will be much less if the vessel does not respond to these short waves.

If we take this one step further, it can be argued that in case it is ship motions that are of interest instead of waves, the components chosen to represent the wave field should be selected based on the *response* spectrum rather than the wave spectrum. In order to do so, the following selection procedure was devised: Let the normalized response spectrum S_{x_i} for motion mode x_i ($i = 1 - 6$ referring to surge-yaw) be given by:

$$S_{x_i}(\mathbf{k}) = \frac{|H_i(\mathbf{k})|^2 \cdot S_\eta(\mathbf{k})}{\int_{-\infty}^{\infty} |H_i(\mathbf{k})|^2 \cdot S_\eta(\mathbf{k}) d\mathbf{k}} \quad (4.37)$$

where S_η indicates the directional wave spectrum wave and H_i indicates the transfer function for motion mode i , defined in the same (earth- fixed) reference system as the wave spectrum. (This means that H_i defined this way will depend on the earth-fixed heading of the vessel!)

Assuming that all 6 ship motion modes are equally important, the so-called normalized *combined* response spectrum is introduced which is defined as:

$$S_x(\mathbf{k}) = 1/6 \sum_{i=1}^6 S_{x_i}(\mathbf{k}) \quad (4.38)$$

Although the normalized combined response spectrum defined this way doesn't have much physical meaning, it can be used in order to select the most relevant wave modes. giving equal importance to all 6 modes and finally resulting in a possibly more optimal selection of the wave modes to be solved.

It should be noted though that such an approach is feasible when it is indeed prediction of the first order response of the vessel that is pursued. For the eventual extension of the application towards prediction of second order drift forces (reported on by [Naaijen and Huijsmans \[2010\]](#)), the relative wave elevation around the vessel will be important which is much affected by shorter waves that are possibly neglected when using the proposed selection procedure based on the *response* spectrum.

Simulations were carried out using the motion response transfer functions of the vessel on board of which the field campaign (presented in the next chapter) was performed. It concerns a 106 m long well intervention vessel. (More details of the ship are presented in section 5.3 of the next chapter. The procedure of computing ship motions using motion transfer functions will be described in paragraph 5.5.2.) During the simulation the vessel had a constant heading with respect to the main direction of the incoming waves resulting in bow quartering waves. The transfer functions were constructed correspondingly. As an example, figure 4.8 shows the normalized heave response spectrum in which the dashed white contour line tightly bounds the 1500 selected components based on the combined response spectrum and the solid white line tightly bounds the components selected based on the wave spectrum. In the former case, 76% of the total heave response energy is represented by the selected components, which is significantly more than the wave energy represented by the same components (which amounts to only 38 %, see figure 4.7). The selected components based on the wave spectrum only represented 52% of the total heave response energy.

The correlation for the heave motion is presented by the black line with circular markers in figure 4.9. (The same figure shows the correlation for the case of a slower turning antenna, which will be discussed in the following.)

EFFECT OF ANTENNA ROTATION SPEED AND HELICAL INTERPOLATION

Concerning the effect of the helical interpolation involved with the 2DFFT approach in order to map the observation to one instant in time per radar revolution, it was observed that it had little to none effect on the correlation (as compared to the situation where the data was synthesized as snapshots with constant time per revolution). However, it must be noted that in practice rotational antenna speeds significantly lower than the assumed 44 rpm are not uncommon. On many ships, navigation antennas are used turning at 24

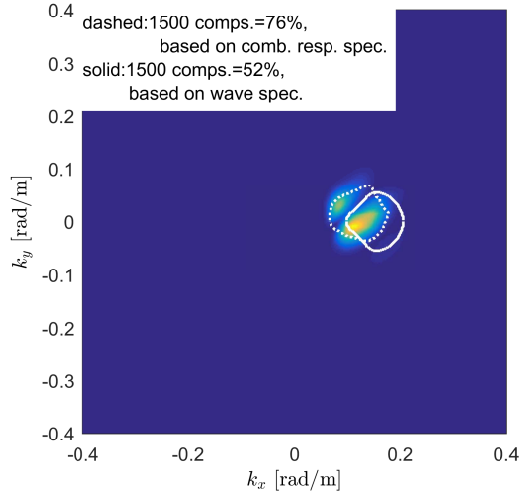


Figure 4.8: Normalized heave response spectrum for wave condition 1, with indications of the partitions represented by 1500 components based on the wave spectrum and the combined response spectrum

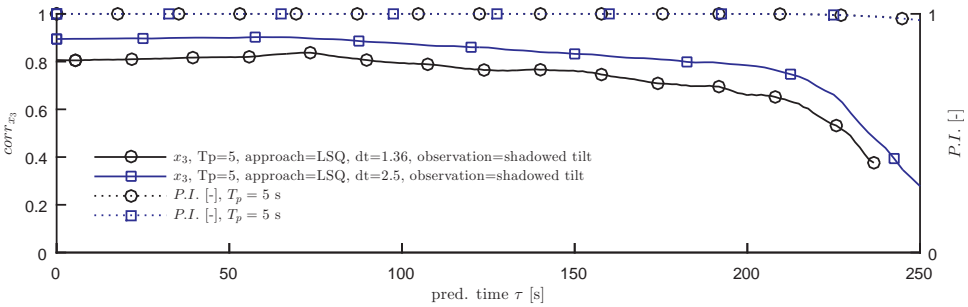


Figure 4.9: Correlation of predicted heave motion obtained with LSQ for condition 1, comparing a fast (44 rpm, black, circular markers) and a slowly (24rpm, blue, square markers) rotating antenna

rpm. In that case, especially for short waves, the mentioned interpolation is likely to have a more dramatic effect: it would result in only two measurement points per peak wave period for condition 1.

Simulation results with condition 1 for the earlier used fast rotating antenna (44 rpm, $dt = 1.36$ s) are compared with those for a slower antenna (24 rpm, $dt = 2.5$ s) in figure 4.10.

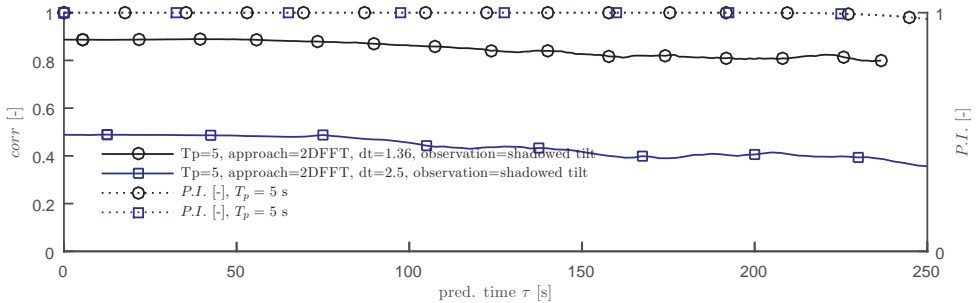


Figure 4.10: Correlation of predicted wave elevation at the antenna obtained with 2DFFT for conditions 1, comparing a fast ($dt=1.36$, black, circular markers) and a slowly ($dt=2.5$, blue, square markers) rotating antenna

As can be seen, the correlation for the case of the slow antenna has dropped dramatically. The same comparison is made for the LSQ approach, as presented by figure 4.11.

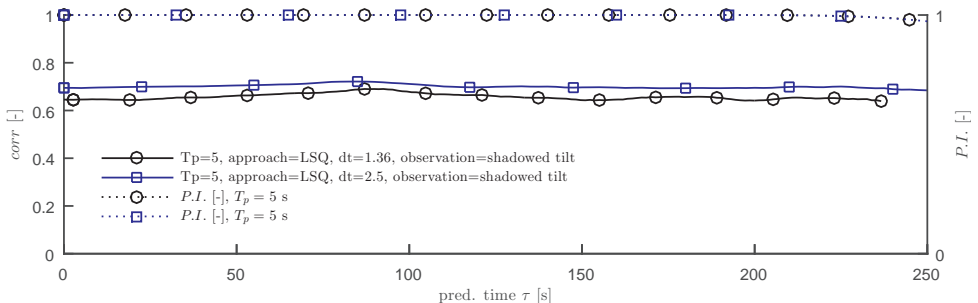


Figure 4.11: Correlation of predicted wave elevation at the antenna obtained with LSQ for conditions 1, comparing a fast ($dt=1.36$, black, circular markers) and a slowly ($dt=2.5$, blue, square markers) rotating antenna

Interestingly, it can be observed that the correlation of the wave elevation for the case of the slow antenna has increased compared to the fast antenna. The correlation of the heave response for the slow antenna has been included in figure 4.9, which also shows the increase. Although slightly surprising at first sight, a likely explanation can be given: in the case of the fast antenna, the observation data taken from 5 subsequent radar revolutions in order to solve the minimization problem (4.27) concerns 1.36 peak wave periods. In case of the slow antenna, 5 images concern 2.5 peak wave periods. Apparently, the decrease in time resolution is over-compensated by the increase in observation du-

ration in terms of 'input information' for the minimization problem. This result gives lead to a more thorough investigation into optimal choice of data to use as input for the minimization problem. Under the restrictions of the maximum size of the minimization problem that will in the end be feasible from the point of view of the computational burden, it might even be the case that in case of a fast antenna, skipping images is beneficial. For the time being, such investigations are left as a recommendation, since they will have to be related to maximum feasible size of the problem and computational speed, aspects that have been left out of consideration in this thesis.

EFFECT OF COUNTER PROPAGATING WAVES IN COMBINED SEA AND SWELL CONDITION

In order to illustrate the advantage of LSQ being able to cope with counter-propagating waves, results are presented for wave condition 4. As shown in table 4.1 condition 4 concerns a bi-modal sea state with wind waves and swell waves propagating in almost opposite main directions. Concerning the 2DFFT simulations, the MED (mean evolution direction, introduced in paragraph 3.5.2) found for this sea state is 87.5 deg and the relevant half of the wave vector space associated with this MED represents 74% of the total wave energy. For the LSQ simulations, the selected 1500 components are representing 91% of the total wave energy. Not surprisingly, the comparison between the two approaches, presented by figure 4.12, reveals a significantly higher prediction accuracy for the wave elevation at the antenna position obtained by the LSQ approach.

Apart from a lower correlation in general, the 2DFFT results shows an initial increase in correlation with increasing prediction time. This phenomenon is related to the blind radius: it does not occur without a blind radius. However, no sound explanation can be given for this particular prediction time dependency of the correlation.

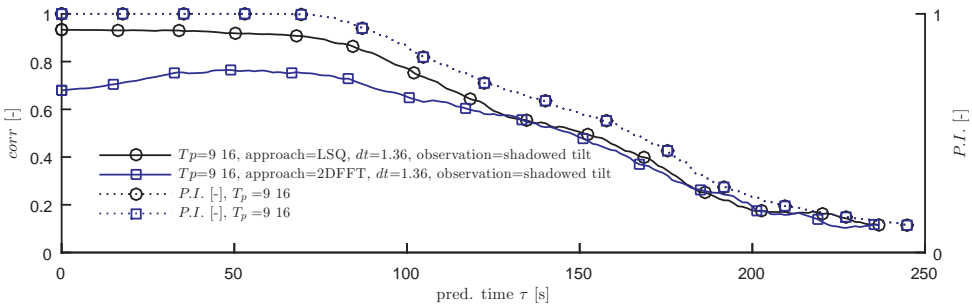


Figure 4.12: Correlation of predicted wave elevation at the antenna obtained with LSQ and 2DFFT for bi-modal sea state of condition 4

EFFECT OF USED NUMBER OF IMAGES PER PREDICTION UPDATE

To conclude this paragraph, a small sensitivity study into the effect of the number of new images used per update, N_t , is presented. See figure 4.13 and 4.14 which present for condition 2 ($T_p = 9$) the correlation of the predicted wave elevation at the antenna against prediction time τ . Figure 4.13 concerns the LSQ approach while 4.14 shows the result using the 2DFFT approach. Overall it can be said that an increased N_t results in

a slightly increased correlation (at least for τ such that $PI. = 1$) for both approaches. For the presented results the update rate was taken equal to the number of new images used per update, as a consequence of which an increase of N_t will result in a decreased number of updates per unit of time, i.e. a decreased update rate. However, this is not a strict requirement to the procedure: there's no principle objection against using updates each of whose subsequent stack of N_t images is overlapping in time. In that case the benefit of using a larger number of images per update, N_t , might be further increased slightly, since an increase of N_t wouldn't result in a lower update rate. Such simulations haven't been carried out.

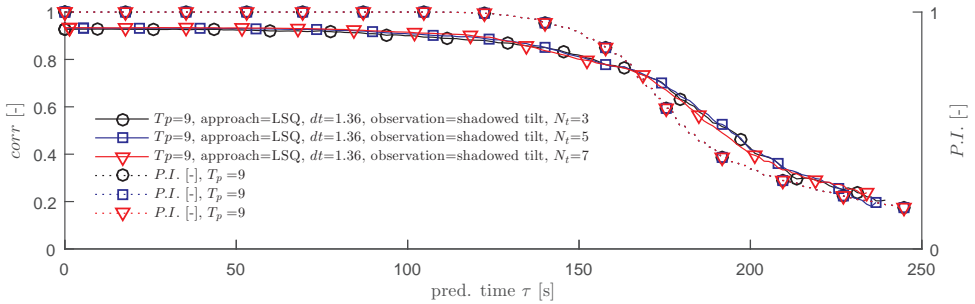


Figure 4.13: Effect of N_t on correlation for $T_p = 9$ s, using LSQ approach

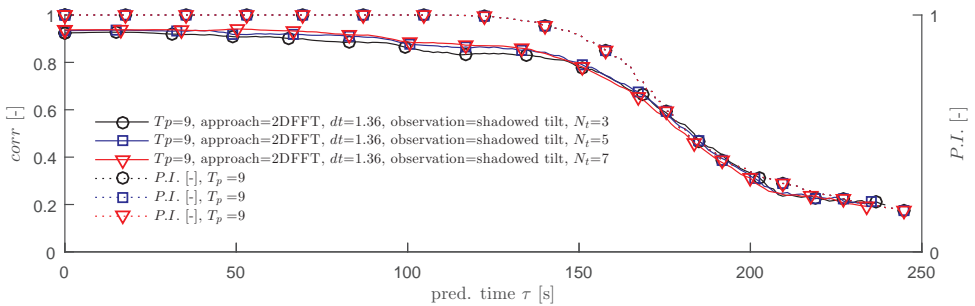


Figure 4.14: Effect of N_t on correlation for $T_p = 9$ s, using 2D FFT approach

In the proceeding paragraph, results from simulations with the procedure for detecting the wave spectrum are presented.

4.5.4. RESULTS AND DISCUSSION WAVE SPECTRUM ESTIMATION

In the context of this thesis, it is not a very exact estimation of the directional spectrum that is pursued: the only reason why an estimate of the directional spectrum is required, is the fact that the most relevant wave modes have to be selected to be solved in case of the LSQ approach: it is sufficient to estimate the most relevant 'footprint' in the wave vector space rather than the exact spectral shape. Therefore, the investigation into spec-

trum estimation presented here is not meant to be an exhaustive study. Only some aspects are highlighted that are relevant within the context of the main objectives.

The confidence level of a wave spectrum estimated by some FFT approach is usually increased by averaging FFT results obtained from subsequent time traces, each of which gives one estimate of the spectrum. Under the assumption that the statistical properties of the waves vary only slowly, the average of the subsequent FFT's is a better estimator for the spectrum than a single FFT result. The averaging comes with the cost of losing phase information. The averaging and dispersion filtering procedure to detect the directional wave spectrum from series of radar images, was verified by the following simulations: To each of N_{av} subsequent partly overlapping time series of N_t synthesized images that were first subjected to the spectral integration (as described in paragraph 4.4.2), a 3D FFT was applied, each of the time series of length N_t starting 8 images later than the preceding one. Converting the individual 3D FFT results into 3D spectra according to equation (4.16) and averaging over the N_{av} subsequently obtained 3D spectra according to equation (4.17) yields the average 3D spectrum S_{av} . Subsequently, dispersion filtering and normalizing according to equation (4.20) and (4.21) results in the average normalized 2D wave spectrum $S_{avn}(\mathbf{k})$. This procedure is repeated N_{real} times using total time series each of which starting as well 8 images later than the preceding realization. For the 3 wave conditions, sensitivity of the obtained accuracy of the directional spectrum to the following parameters have been investigated :

- N_t , length of the time series to which 3D FFT is applied
- effect of not taking into account tilt effect, i.e. omitting the spectral integration. (Doing so is likely to result in over-estimation of the energy related to high wave number components. Indeed, [Borge et al. \[2004\]](#) shows that the tail of the spectrum obtained by ignoring the tilt effect is too thick.)
- the filter width of the dispersion filter f used in equation (4.20), i.e. the value of w_f in equation (3.25) as described in section 3.6

The accuracy of the detected S_{avn} is quantified in terms of the following error definition:

$$Err_S = \frac{1}{N_{real}} \frac{\sum_{i=1}^{N_{real}} \int_{-\infty}^{\infty} |S_{avn_i}(\mathbf{k}) - S_n(\mathbf{k})| d\mathbf{k}}{\int_{-\infty}^{\infty} S_n(\mathbf{k}) d\mathbf{k}} = \frac{1}{N_{real}} \sum_{i=1}^{N_{real}} \int_{-\infty}^{\infty} |S_{avn_i}(\mathbf{k}) - S_n(\mathbf{k})| d\mathbf{k} \quad (4.39)$$

where S_n is the normalized theoretical directional spectrum used to generate the synthetic waves. N_{real} is the number realizations.

Firstly, simulation results with and without omitting the spectral integration are compared. To isolate this issue, these investigations concern simulations with synthesized radar data without shadowing. Not surprisingly, figure 4.15 shows that the error in the spectrum detection is indeed significantly larger when interpreting the images as elevation, while in fact they include the tilt effect. This is of course in a sense a very self fulfilling prophecy, since in the synthesized data the tilt effect *was* included.

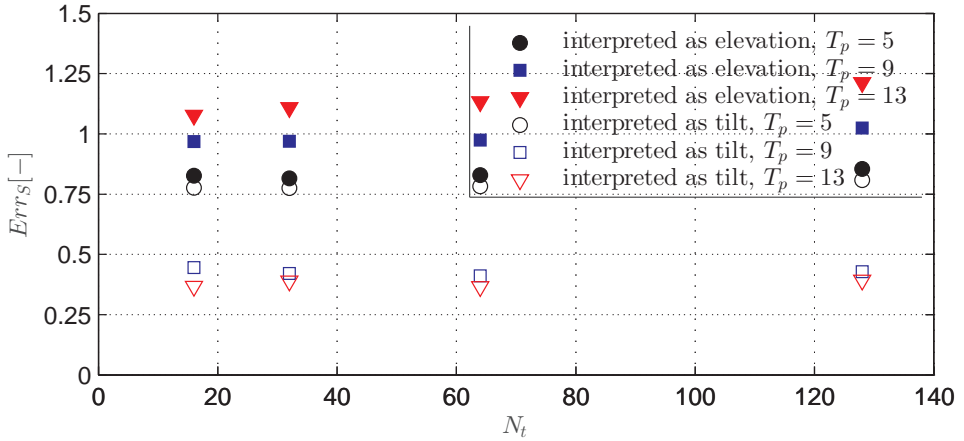


Figure 4.15: Error in directional spectrum detection, Err_S

It is still interesting to illustrate that under the assumption that the used model for backscatter is indeed realistically representing actual radar back scatter, it is crucial to include the tilt effect in the interpretation of the back scatter data: Figure 4.16 shows the 1D spectrum (which is obtained by transforming S_{av} from the \mathbf{k} basis to the (ω, θ) basis and integrating over θ) for the case of $N_t = 128$ and $w_f = 1$.

The figure clearly illustrates how the 'wrong' interpretation of the radar data results in an overestimated energy at the higher frequencies. This effect becomes more pronounced with longer peak period since the difference between the amplitude of the wave elevation and the amplitude of the tilt is larger for lower wave numbers. It can be concluded that despite the fact that it is merely a 'footprint' of the spectrum in \mathbf{k} -space that will be used (in order to select the relevant wave components to be solved with LSQ) rather than the actual shape of the spectrum, it is not justified to neglect the tilt effect in the spectrum detection: doing so will result in a possibly wrong selection of components.

Some additional investigations were carried out in order to obtain a suitable choice for the filter width w_f . Results are presented in figure 4.17, from which it can be concluded that the choice of w_f does not have a dramatic effect on the accuracy of the detected spectrum. A reasonable choice for w_f seems to be 5.

Finally, investigations were carried out in order to assess the effect of shadowing. The results are presented in figures 4.18 and 4.19, showing the error Err_S and a comparison with the theoretical 1D spectra respectively. As can be expected, a higher Err_S is found for the situation including shadowing although the effect is not dramatic. However, the difference with the situation without shadowing decreases with increasing N_t . It is therefore concluded that of the considered values of N_t , $N_t = 128$ can be considered as the optimal choice.

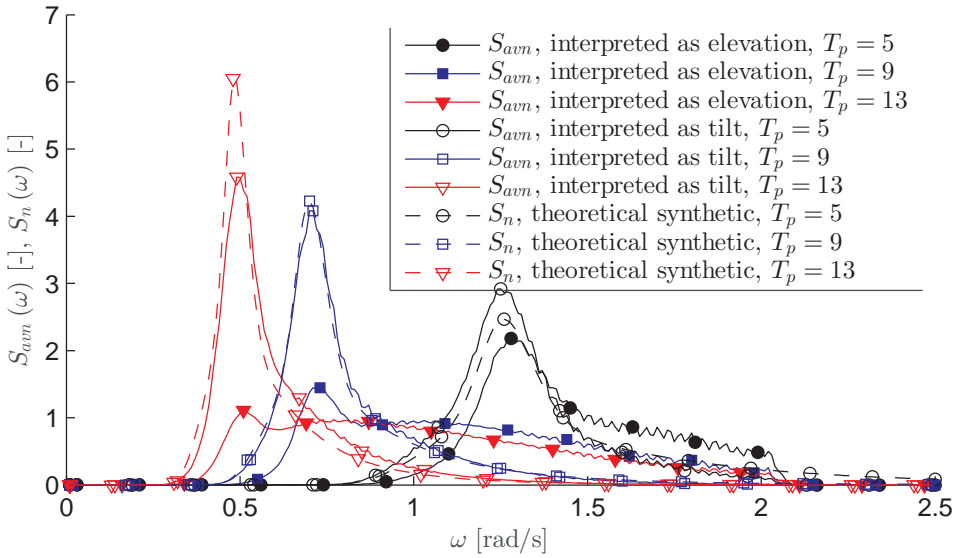


Figure 4.16: Detected and theoretical 1D Spectra

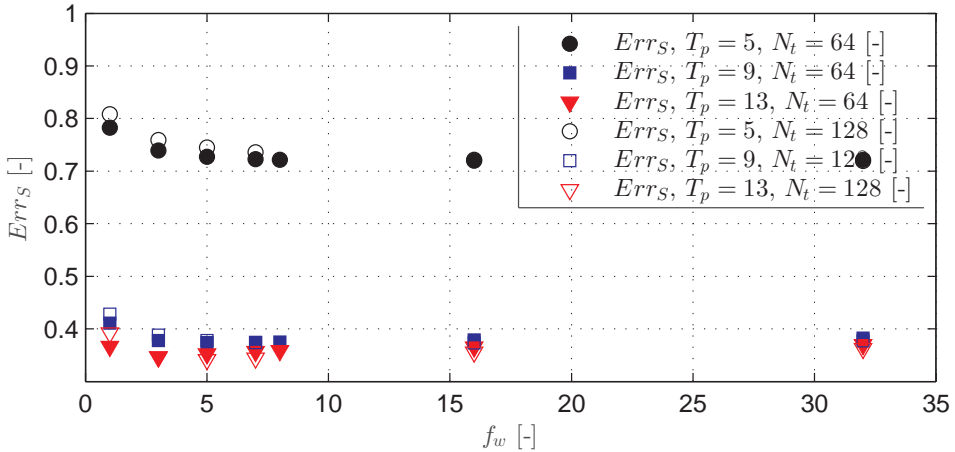


Figure 4.17: Effect of filter width on accuracy of detected spectrum

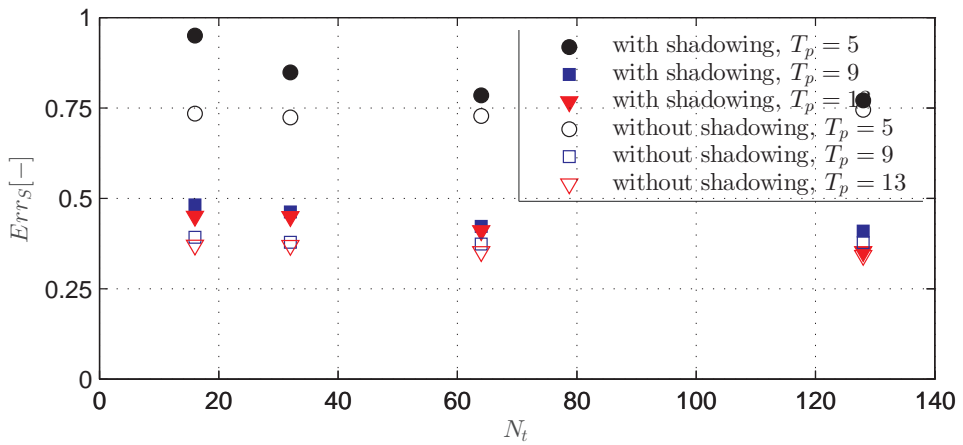


Figure 4.18: Error in directional spectrum detection, including shadowing Err_s

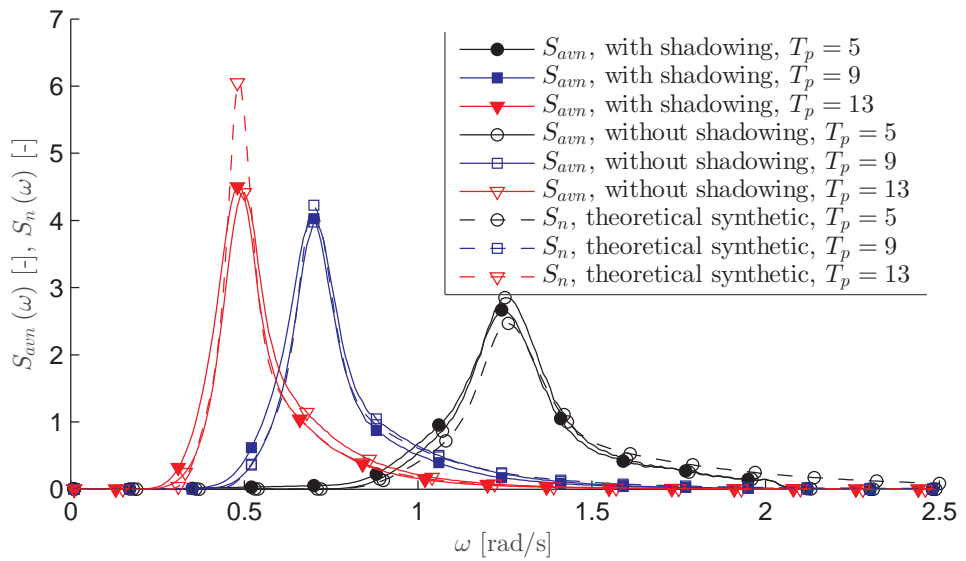


Figure 4.19: the effect of shadowing on the detected 1D Spectra

4.6. CONCLUSIONS AND RECOMMENDATIONS

Two approaches have been presented for deterministic wave predictions from radar observations including the tilt effect. Both have been shown to be able to yield accurate results by applying them to synthetic radar data. It is not possible to draw one general conclusion about which of the two approaches is superior. It has been shown that this depends on the wave condition and properties of the simulated radar system. For the considered cases, it can be said that 2DFFT is superior in case of situations where the limited number of wave components solved with LSQ does not represent a sufficient fraction of the total wave energy. A required condition for this, is a sufficiently fast rotating radar antenna: the linear helical interpolation preceding the 2DFFT, applied to map the radar data to constant instant in time, has been shown to introduce high inaccuracies in case of a combination of short waves and a slow antenna. For the investigated longer wave periods, the chosen 1500 wave components represented at least 89% of the wave energy in which cases accurate results were obtained with LSQ. Table 4.3 summarizes the comparisons presenting the minimum and maximum correlation of the wave elevation at the antenna found for prediction time values τ at which the predictability indicator $P.I. = 1$. Minimum and maximum correlation are indicated with $corr_{min}$ and $corr_{max}$ respectively. The maximum prediction time τ for which $P.I. = 1$ is indicated by τ_{max}

Condition	T_p [s]	τ_{max} [s]	$corr_{max}$ [-]		$corr_{min}$ [-]	
			LSQ	LSQ	2DFFT	2DFFT
1	5.0	215	0.68	0.61	0.88	0.81
2	9.0	120	0.93	0.89	0.93	0.85
3	13.0	80	0.98	0.90	0.89	0.85

Table 4.3: Minimum and maximum correlation of wave elevation at antenna for $P.I. = 1$ obtained with LSQ and 2DFFT

Investigations concerning the detection of the 2D wave spectrum revealed that it is important to take into account the tilt effect even if the detected spectrum only serves as input for the selection procedure of the most relevant wave modes: ignoring tilt can lead to a not optimal selection of wave modes. It was also shown that the effect of shadowing on the accuracy of the detected spectrum is limited in case the 3D FFT is applied to sufficiently long time traces of radar images: best results were obtained for the case of $N_t = 128$. Variations of the width of the dispersion filter f_w lead to the conclusion that 5 is a suitable value for f_w .

Concerning the averaging procedure represented by equation (4.31), the weighing factor w between the evolution and the new observation was taken 0.5. Like in chapter 3, again no in depth investigations into a potentially more optimal choice of w have been undertaken and are left as a recommendation.

As mentioned, due to the memory limitation of the GPU, there is a trade-off between maximum range and number of images from which observation data is used (and the number of modes to be solved) for the LSQ problem. In depth investigations into optimizing this trade-off, which is again likely to be depending on the wave condition, have not been undertaken.

Also related to the limited memory of the GPU and to the computational burden of solving LSQ problem is the limited number (1500) of wave modes that were solved. Increasing this number would increase the energy associated to the solved modes, improving the prediction accuracy, especially for the shorter wave conditions. Currently the computational time prevents real time application of the LSQ approach. Investigations into a fast solver for the LSQ problem and an efficient implementation (on the GPU) are required to develop the presented technology from a proof of principle to an operational tool and are left as a recommendation.

Apart from the aforementioned increase of the number of wave modes, another way to improve the results for short wave conditions (or more generally for conditions with the large footprint in the wave number space), is to improve the selection of the wave modes: for the LSQ approach the resolution $d\mathbf{k}$ in the wave number space associated to the chosen set of wave components, was linked to the chosen spatial grid as explained in the preceding. The consequence of this was that for the short wave condition, the chosen fixed number of components only represented a relatively small fraction of the total wave energy. This resulted in a poor accuracy of the wave prediction. A very logical way to improve the result is to optimize the chosen $d\mathbf{k}$: with a larger $d\mathbf{k}$, 1500 components will represent a larger fraction of energy, thus improving the accuracy. Such optimization will involve a trade-off between resolution in the wave number space and total energy represented by the chosen number of components and is left as a recommendation for further improvement of the LSQ approach.

5

APPLICATION AND VALIDATION WITH FIELD DATA

5.1. SUMMARY

This chapter presents the results of a validation study where the LSQ approach as presented in the previous chapter is applied to real radar images recorded during the field campaign carried out within the framework of the OWME-JIP project. During this campaign, radar images and vessel motions of the well-intervention vessel 'Island Frontier' were recorded. The vessel was operating under DP i.e. without forward speed. Some details of the campaign and the acquired data will be presented. Motions of the vessel are computed from the predicted waves using the vessel's available RAO's. Since the exact relation between real radar images and wave height is unknown, the recorded vessel motions are used to scale the predicted motions as will be described. Finally predicted vessel motions will be compared to recorded vessel motions, yielding an accurate to fairly accurate match.

5.2. INTRODUCTION

The joint industry project (JIP) OWME (Onboard Wave and Motion Estimator) had an objective that was very similar to the PROMISED project: to derive a prediction of phase resolved ship motions up to at least 2 minutes in advance using navigation radar data as a remote wave sensor (Dannenberg et al. [2010]). Part of the project was a field campaign for which the well intervention vessel 'Island Frontier' was used while it was operating in the Statoil operated Gullfaks oil field in the North Sea, 110 nm North-West of Bergen. During the campaign, a wave buoy was deployed and raw radar data was stored. Additionally the vessel was equipped with a motion sensor and a down looking radar, both mounted on the helideck. Comparisons made back in the days of the OWME JIP between recorded ship motions and predictions obtained from the radar data did not yield any statistically significant correlation. With the benefit of hindsight, it can be stated now that the most important reason for this is the fact that the used methodology during the OWME project relied on the 3DFFT approach, which has been shown in chapter 3 to be not suitable for phase-resolved prediction. Having developed the alternatives presented in chapter 3 and 4, yielding much more promising results from synthetic radar data, was enough reason to revisit the OWME campaign and apply the newly developed methods to the available data. It was shown in chapter 4, that the performance of the two proposed approaches for deterministic wave prediction largely depends on the encountered condition. For longer wave periods, given that the limited number of solved wave components with LSQ represent a sufficiently large fraction of the total wave energy, LSQ yielded more accurate results. Anticipating the conditions that occurred during the OWME field campaign, which were sea states with peak periods all above 11 s, it was decided to select the LSQ approach to be applied to the field data. Challenges regarding computational efforts involved with solving the minimization problem of equation 4.27, which currently prevent real-time application of the LSQ approach, are assumed to be solvable by improved numerical methods and/or increased hardware capacity. In order to achieve a proof of principle for successful deterministic wave / vessel motion prediction from non-coherent radar data, which has not been reported on in literature, accuracy is considered to be the dominating criterion.

In this chapter the stored raw radar data obtained from the OWME campaign will be used as input in similar simulations as presented in chapter 4. The LSQ approach is applied to predict the Island Frontier's motions, which will be compared to the recorded motions.

5.3. VESSEL AND TRIAL LOCATION

The vessel that hosted the OWME field experiments was the light-well intervention vessel 'Island Frontier', depicted in figure 5.1. The vessel was operating under DP during trials at the Gullfaks oil field offshore the coast of Bergen where the water depth amounts to 127 m. The experiments took place between 17 and 25 September 2008.



Figure 5.1: Island Frontier

Some vessel dimensions are given in table 5.1.

Vessel name	Island Frontier
Owner / operator	Island Offshore
Length over all	106.2 m
Width	21.0 m
Deadweight	4700 ton

Table 5.1: Vessel specs Island Frontier

The motion response functions (RAO's and phase angles of the 6 DOF motions) were provided by the owner and depicted in Appendix D, figure D.1.

5.4. USED SENSOR DATA

During the OMWE trials, data was acquired over a period of 8 days. The amount of actually useful data resulting from the trials is rather limited though due to the fact that a few criteria had to be satisfied simultaneously, which was the case for only a short period of time. Examination of the available data resulted in the selection of 3 data sets considered to sufficiently meet all criteria. These are listed in table 5.2. The criteria referred to are:

- radar operating at short pulse
Standard navigation radar systems have an adjustable pulse rate: short pulse gives short range but high spatial resolution while long pulse provide a far range at the price of lower spatial resolution. In general, the coarse spatial resolution associated with long pulse setting is insufficient for wave detection.
- sufficient radar data quality
Sufficient signal to noise ratio: at too low wind speed and/or too low wave height, x-band navigation radar is known to give insufficient back scatter / modulation of back scatter respectively, resulting in wave extraction from the data to fail.
- sufficient radar data quantity: minimal amount of data acquisition interruptions
The data acquisition was done by the WAMOS system. For various reasons it may occur that data from one or several antenna rotations is not stored. Although the 3D FFT involved with detecting the 2D wave spectrum requires uninterrupted input sequences, (small) data gaps are not necessarily a major problem for the proposed deterministic prediction approaches. Time slots were selected with interruption intervals of at most 15 seconds. (All three selected time slots indeed contained some interruption intervals of almost 15 seconds as can be seen in Figure E1 which shows the time intervals between subsequently acquired radar images (referred to as dt_{im}) during the three selected data sets. The antenna rotation time was 1.36 s.)
- availability of reference signal from the motion sensor
Motions of the vessel were recorded by the motion reference unit (MRU) mounted at the heli deck. Data acquisition was interrupted multiple periods of time. Of the selected data sets, only the 3rd one contains a MRU data gap of 27 seconds.

	start data / time	end data / time	duration
data set 1	2008-09-22 04:00:00	2008-09-22 06:00:00	2 hours
data set 2	2008-09-22 20:00:00	2008-09-22 21:00:00	1 hour
data set 3	2008-09-25 17:00:00	2008-09-25 18:00:00	1 hour

Table 5.2: Selected data set for validation

5.4.1. RADAR DATA

RADAR SPECS ISLAND FRONTIER

The radar data used in this validation study was acquired from the vessel's navigation radar antenna by Ocean Waves' WAMOS data acquisition system. Basically, the data

acquisition system combines the analogue radar video signal, the corresponding trigger pulse, the azimuth change pulse (ACP) and the azimuth reset pulse (ARP) in order to create files containing radar back-scatter as a function of range and azimuth. These mentioned files will be referred to as raw polar files and contain the most raw form of the radar data. Besides these files contain ship's position data, being GPS longitude and latitude and the vessels heading obtained by the gyro compass. Some specs of the radar system used onboard the Island Frontier are given in table 5.3.

Radar brand/type	Furuno FR-2115
Antenna length	6.5 ft
Antenna height above free surface	25 m
Antenna specified beam width	1.23 deg
Radar repetition time (RPT)	1.36 s
Digitization rate	20 MHz
Range resolution	7.5 m
Samples per pulse	256
Dead/blind zone	120 m
Maximum range	2040 m
Pulse rate	1.188 kHz
Azimuth sample resolution	0.22 deg
Nr. of bits ADC	12

Table 5.3: Radar specs Island Frontier

THE EFFECT OF ANTENNA MOTIONS ON THE RECEIVED RADAR SIGNAL

Obviously, due to the ship motions, the antenna cannot be assumed to be positioned in a perfectly constant location nor orientation. Concerning the *location*, the instantaneous position can in theory be measured by a sufficiently accurate GPS location sensing system. Using the available GPS systems on a vessel, knowing the relative position of the GPS antenna and the radar antenna, together with the vessel heading obtained from the gyro compass, the earth fixed horizontal location of the antenna can be found. For the presented results in this chapter, this is indeed the followed approach.

This approach requires an additional synchronized measurement of the vessel's roll and pitch motions in case their effect on the horizontal position of the antenna is to be taken into account as well. This has not been done in practice mainly because of the questionable time synchronization of radar data and recorded vessel motions.

In order to assess the effects of the antenna *orientation*, let's consider three possible rotational modes of the antenna defined as: *roll rotation* around an axis parallel to the instantaneous look direction in the horizontal plane, *pitch rotation* around an axis perpendicular to the instantaneous look direction in the horizontal plane and *azimuth rotation* around a vertical axis. The azimuth rotation is taken into account by an exact measurement, available through the so-called azimuth count pulse (ACP) signal which is part of any scanning radar system.

In general for the mapping of the radar return time to range, the vertical elevation of the antenna Λ above the surface is neglected introducing an error that is much smaller

than then the range resolution. Let r' be the exact distance from the antenna and r its projection in the horizontal plane of the free surface:

$$r' = \sqrt{\Lambda^2 + r^2} \quad (5.1)$$

where Λ is the elevation of the antenna above the free surface.

The difference between r' and r is presented in figure 5.2(a). For the case studies presented in this chapter, where a blind radius of $r_0 = 250$ was assumed and the antenna elevation Λ being 25 m, the largest range error due to neglecting the antenna elevation (occurring at $r = 250$) is 1.25 m. This is indeed well within the radar's range resolution of 7.5 m and very small with respect to the relevant wave lengths to be observed.

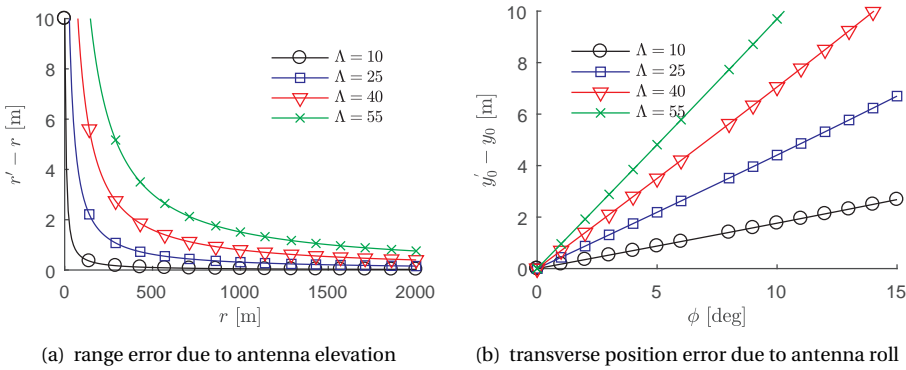


Figure 5.2: Position error due to antenna elevation and roll rotation

A roll rotation of the antenna would result in a shift of the illuminated sea surface in transverse (y) direction, i.e. perpendicular to r . This is illustrated in figure 5.3(b) and 5.3(d) where b_ϕ is the so-called azimuth beam-width. The positioning error $y'_0 - y_0$, defined as the distance between the center of the beam when looking vertically down and when looking under angle antenna roll angle ϕ can be expressed as:

$$y'_0 - y_0 = \Lambda \tan(\phi) \quad (5.2)$$

Figure 5.2(b) presents this error as a function of antenna roll angle ϕ for various values of antenna elevation Λ . The azimuth beam width b_ϕ of a radar antenna depends on the antenna beam and amounts to 1.2 deg for the radar system on board the Island Frontier, resulting in a resolution in y -direction between 5.4 m at $r = 250$ m and 26.8 m at $r = 1250$ m, from which it is concluded that especially at larger ranges, the positioning error $y'_0 - y_0$ due to antenna rotation is small.

For the effect of the pitch rotation it is important to understand the principle of remote sensing with radar. See figure 5.3(a) which shows the antenna elevation beam-width b_θ , illuminating the surface between range r_1 and r_2 . Figure 5.3(c) show the situation after an antenna pitch rotation: the illuminated part has shifted. Since the range r of the points within the shifted illuminated part is associated with the return time of the radar signal, their values haven't shifted. This means antenna pitch rotation only affects the illuminated part, but doesn't introduced a range 'error'.

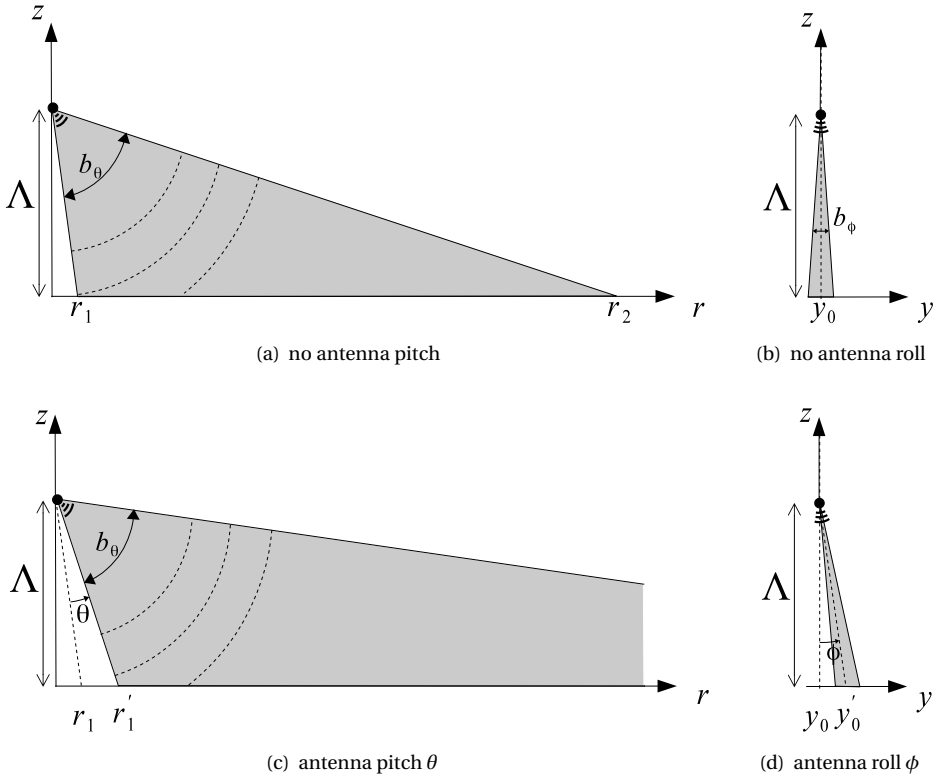


Figure 5.3: Antenna pitch and roll

RECEIVED RADAR SIGNAL AND OFFSET CORRECTION

This paragraph describes some aspects concerning the radar data that was recorded during the OWME trials and how this data was pre-processed in order to enable the application of the proposed analysis method in the previous chapter.

In chapter 4, it was considered how to obtain wave elevation from the NRCS σ_0 . In practice, nautical radars do not provide the NRCS value itself but the amplified received signal power P_r . The received signal power P_r can be formulated by the radar equation:

$$P_r = P_t G_t A_w \frac{r^{-4}}{(4\pi)^2} \cdot \sigma_0 \tag{5.3}$$

with P_t, G_t, A_w being transmitted power, gain factor and effective aperture respectively. Additionally a logarithmic amplifier is used for nautical radar whose base is in general not known. The recorded radar data can therefore be presented as:

$$I_0 = {}^b \ln \left(P_t G_t A_w \frac{r^{-4}}{(4\pi)^2} \sigma_0 \right) \tag{5.4}$$

with b being the unknown base of the logarithmic amplifier. (Additionally, an ADC usu-

ally converts the radar data into an unsigned integer value in order to save storage disk space and speed up I/O. In case of the Island Frontier, the radar video output from data acquisition system was represented by 12 bit unsigned integers.)

Using the NRCS model from the previous chapter (paragraph 4.3), I_0 can be related to the wave steepness η_r : Substituting eq. 4.1, 4.12 and 4.9 in eq. 5.4 and applying a 1st order Taylor expansion around $\delta\sigma_0 = 0$ yields:

$$I_0 = \frac{\ln\left(P_t G_t A_w \frac{r^{-4}}{(4\pi)^2}\right)}{\ln(b)} + \frac{\ln(\bar{\sigma}_0)}{\ln(b)} + \frac{\delta\sigma_0}{\ln(b)\bar{\sigma}_0} = \frac{\ln\left(P_t G_t A_w \frac{r^{-4}}{(4\pi)^2}\right)}{\ln(b)} + \frac{\ln(\bar{\sigma}_{0B} + c \cos(\Theta(r)))}{\ln(b)} + \frac{c \sin(\Theta)}{\ln(b)(\bar{\sigma}_{0B} + c \cos(\Theta))} \partial_r \eta \quad (5.5)$$

The first two terms in eq. 5.5 represent a range dependent constant. A pragmatic approach to finally obtain $\partial_r \eta$ from the recorded I_0 , is to first eliminate this constant by subtracting a range and azimuth dependent average of I_0 obtained from a time history: (The NRCS is considered to be azimuth dependent because of its probable wind direction dependency. Moreover, interaction of the transmitted radar waves with the ship's hull is very likely to introduce additional azimuth dependency.)

$$I(r, \varphi, t) = I_0(r, \varphi, t) - I_{0,av} = I_0(r, \varphi, t) - \frac{1}{D_h} \int_{t-D_h}^t I_0(r, \varphi, t^*) dt^* \quad (5.6)$$

where D_h is the duration of the used time history and I represents now only the last term in eq 5.5:

$$I(r, \varphi, t) = \frac{c \sin(\Theta(r))}{\ln(b)(\bar{\sigma}_{0B} + c \cos(\Theta(r)))} \partial_r \eta(r, \varphi, t) \quad (5.7)$$

This approach however has an undesired side effect. Because of shadowing, only parts of the wave field are visible as a result of which $I_{0,av}$ will be biased as compared to the non shadowed situation. This is explained and illustrated in more detail in appendix E by analyzing the visibility of a harmonic wave as was done by [Wijaya and van Groesen \[2016\]](#). No attempts were made in order to mitigate this bias effect.

Substituting in equation (5.7) the 'depression angle' $\tilde{\Psi}$, being the angle between the radar look direction in the vertical plane and the horizontal plane, $\tilde{\Psi} = \frac{\pi}{2} - \Theta$ and assuming it is small, we find:

$$\begin{aligned} I(r, \varphi, t) &= \partial_r \eta(r, \varphi, t) \ln(b)^{-1} \frac{\cos(\tilde{\Psi}(r))}{\bar{\sigma}_{0B} c^{-1} + \sin(\tilde{\Psi}(r))} \approx \\ &\partial_r \eta(r, \varphi, t) \ln(b)^{-1} (\bar{\sigma}_{0B} c^{-1} + \tilde{\Psi}(r))^{-1} \approx \\ &\partial_r \eta(r, \varphi, t) (\ln(b) \bar{\sigma}_{0B} c^{-1})^{-1} = \\ &\partial_r \eta(r, \varphi, t) C^{-1} \quad (5.8) \end{aligned}$$

where C is representing a scaling factor: $C = \ln(b) \bar{\sigma}_{0B} c^{-1}$

This means that the above approximations have lead to an interpretation of the received radar data (first corrected for a range dependent offset) which is linear in $\partial_r \eta$ and can be used as input for the LSQ procedure as outlined in chapter 4. The scaling factor C is unknown at the time of simulation but can be eliminated by using a reference measurement as will be explained in paragraph 5.5.2.

5.4.2. MOTION SENSOR DATA

A motion reference unit (MRU) containing a 3-axis accelerometer and a 3-axis gyro was installed during the trials from which the 3 DOF translational displacements (surge, sway and heave) and the 3 DOF rotational displacements (roll, pitch, yaw) were derived. The sensor was mounted below the deck of the heli-platform as depicted in figure 5.4.

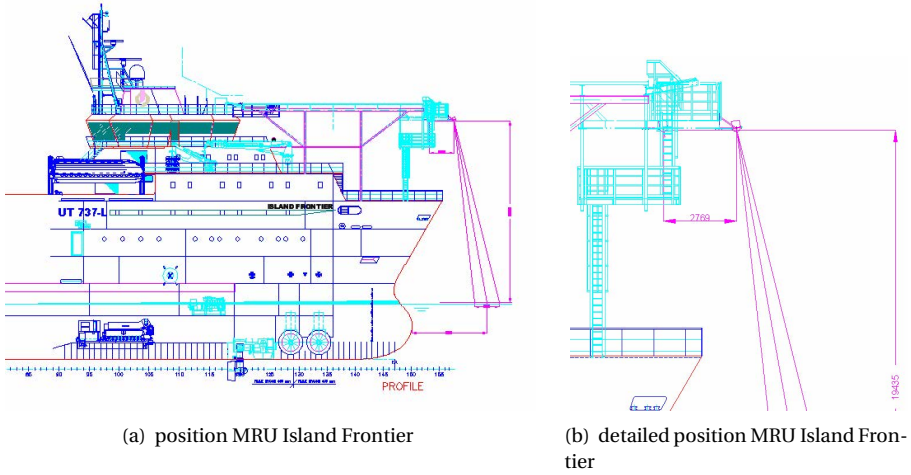


Figure 5.4: Mounting position of MRU sensor onboard Island Frontier

The motion sensor used is a 6 degree of freedom medium accuracy sensor with specifications given in Appendix G.

The translations of and rotations around the center of gravity (COG) of the vessel, referred to as surge, sway, heave and roll, pitch yaw respectively were derived from the recorded motions of the motions sensor, linearizing for small rotation angles:

$$\begin{pmatrix} x_{1,MRU} \\ x_{2,MRU} \\ x_{3,MRU} \end{pmatrix} = \begin{pmatrix} x_{1,S} \\ x_{2,S} \\ x_{3,S} \end{pmatrix} - \begin{pmatrix} 0 & -x_{6,S} & x_{5,S} \\ x_{6,S} & 0 & -x_{4,S} \\ -x_{5,S} & x_{4,S} & 0 \end{pmatrix} \begin{pmatrix} x_S \\ y_S \\ z_S \end{pmatrix} \quad (5.9)$$

where $x_{1,MRU}$, $x_{2,MRU}$ and $x_{3,MRU}$ refer to the vessel's measured surge, sway and heave motion respectively. $x_{1,S}$, $x_{2,S}$ and $x_{3,S}$ refer to the longitudinal, transverse and vertical motion of the motion sensor respectively. $x_{4,S}$, $x_{5,S}$ and $x_{6,S}$ refer to the sensor's rotations around the longitudinal, transverse and vertical axis respectively. Sensor's axes coincide with the vessel's axes which results in:

$$\begin{pmatrix} x_{4,MRU} \\ x_{5,MRU} \\ x_{6,MRU} \end{pmatrix} = \begin{pmatrix} x_{4,S} \\ x_{5,S} \\ x_{6,S} \end{pmatrix} \quad (5.10)$$

where $x_{4,MRU}$, $x_{5,MRU}$ and $x_{6,MRU}$ refer to the vessel's measured roll, pitch and yaw motion respectively.

5.5. SIMULATIONS

As described in chapter 4, the applied analysis method that finally leads to the individual amplitudes and phases of the frequency and wave number dependent wave components, exists of two phases:

1. A conventional 3DFFT and dispersion filtering is applied to subsequent sets of images, in order to detect the directional wave spectrum and surface current.
2. The phase resolved solving of the wave components using LSQ

For real time application, these two processes would need to run in parallel (with possibly different update rates). For the proof of concept that is pursued on this chapter, they two steps were carried out in separate simulations where spectrum updates from the first step were saved to be used later in the second step.

Having solved the individual wave components in step 2, these are propagated, multiplied by the vessel motion transfer functions and summed to yield the predicted time traces of vessel motions.

In the next paragraphs, some more details are given of the computational procedure summarized above, finally leading to the results of the ship motion prediction to be presented later in this chapter.

5.5.1. PROCEDURE AND SETTINGS OF SPECTRUM AND CURRENT DETECTION

As explained in chapter 4 LSQ only solves relevant wave modes in order to reduce the computational effort. The selection of these relevant modes is done based on the directional wave spectrum, which is derived from the radar images by means of the procedure described in paragraph 4.4.1.

The values of the parameters used for this procedure as explained in paragraph 4.4.1 are given in table 5.4. The procedure is applied to the averaging buffer, which is a running buffer existing of the most recent N_{av} (120) series of N_t (128) images which is updated with every 16th newly acquired image.

parameter	symbol	unit	value
blind radius	r_0	[m]	250
max. observation radius	r_{max}	[m]	1800
Nr. of observation points in x direction	N_x	[-]	512
Nr. of observation points in y direction	N_y	[-]	512
Nr. of images used per 3DFFT	N_t	[-]	128
spatial resolution in x direction	dx	[m]	7.5
spatial resolution in y direction	dy	[m]	7.5
update rate		[-]	16
averaging buffer length	N_{av}	[-]	120
dispersion filter width	w_f	[-]	5

Table 5.4: Parameters of 3DFFT spectrum detection

Surface current velocity was not solved but assumed to be 0. For the 3 investigated data sets, the directional spectra obtained from the above described procedure, averaged over the duration of the considered data set is presented in figure H.1. Some obtained wave characteristics are presented together with the vessel's heading in table 5.5. As can be seen all three investigated cases concern a uni modal wave wave condition with a peak wave direction close to Eastward. For all cases the vessel was positioned such that it experienced approximately bow-quartering waves.

data set	T_p [s]	θ_p [deg]	Ψ [deg]	μ [deg]
	peak period	peak dir.	ship's gyro	peak wave dir.
		rel. to East		rel. to ship
1	10,7	8,1	196	114,1
2	12,2	-9,4	226	126,6
3	11,12	-3,6	231	137,4

Table 5.5: Wave field parameters found from spectrum estimation and vessel heading

5.5.2. PROCEDURE AND SETTINGS LSQ

UPDATING AND VESSEL MOTIONS

In order to calculate the phase resolved wave components, the LSQ approach as outlined in 4.4.3 was used. At each update step, the elements of the observation vector \mathbf{b} in equation 4.27 are taken from the most recent series of acquired radar images. The length of this series of images used as input for each computation update step was maximized with regard to the memory size of the graphical processing unit (GPU) that was used to solve the system of equations (eq. 4.27) and corresponds to minimum 5 and maximum 10 images per update for the presented cases. (The number of radar images from which the observation data for a certain update is not fixed, since the amount of shadowing may vary per image and per wave condition.) Updates are computed every 5th antenna rotation. After having solved the phase resolved wave component amplitudes \mathbf{a} , the wave elevation at any given location \mathbf{x} and time t can be obtained by substituting these amplitudes in equation 4.22. Here, for each individual update, \mathbf{x} is relative to the axes system used for solving the minimization problem of equation 4.27 whose origin is located at the vessel's antenna position corresponding to the first recorded image of the entire considered data set. The x - and y - axis of the used earth-fixed coordinate system are pointing Eastward and Northward respectively. For each u^{th} individual update, t_u is associated with the time of recording the first beam of the last image of the series of images from which the observations were taken.

In the proceeding, results will be presented concerning the so-called 'nowcast' of wave elevation or vessel motions. Time traces of the nowcast (or forecast) are created in a similar way as explained in the beginning of paragraph 4.5.3 by concatenating the values of subsequent updates: In paragraph 4.5.3, updates of the wave elevation prediction at the antenna position as a function of prediction time τ were given by $P_0(t, \tau) = P_0(t_u, \tau + m \cdot dt)$, with $m \in \{0, 1, 2, 3, 4\}$ in case of a solution update rate of $5dt$ (5 antenna revolutions).

Now, let x_i be the equivalent of P_0 for vessel motion mode i , i referring to the 6 possible motion modes. So e.g. $x_3(t, \tau = 0)$ represents the time trace of the heave motion nowcast obtained by the above mentioned concatenation. Again, for u yields $\{u \in \mathbb{Z} | u_{\min} \leq u\}$ where u_{\min} corresponds to the time at which all (including the shortest) waves have crossed the blind zone with radius r_0 . The actual vessel motion prediction update u is computed in a similar way as was done for the the wave prediction update P_0 in equation (4.35):

$$x_i(t_u, \tau) = \text{Re} \left(\sum_{n=1}^N H_i(\Omega(\mathbf{k}_n), \theta_n - \Psi(\tau)) a_u(\mathbf{k}_n) e^{i(\mathbf{k}_n \Delta \mathbf{x} - \Omega(\mathbf{k}_n)(t_u + \tau))} \right) \quad (5.11)$$

Comparing to equation (4.35) there are a few changes:

- H_i has been substituted which is the transfer function of the considered motion as a function of wave frequency Ω and wave direction relative to the vessel. The wave direction relative to the vessel equals $\theta - \Psi$, with Ψ being the vessel's heading with respect to the coordinate system's x-axis (i.e. with respect to East). τ represents the prediction time.
- $r = 0$ is substituted
- spatial shift $\Delta \mathbf{x}$ is added in order to take into account the horizontal position of the ship's center of gravity (with respect to which the motion transfer functions are defined) and the radar antenna. Besides, $\Delta \mathbf{x}$ can represent a horizontal position offset of the ship relative to the chosen spatial origin.

In case of the field data simulations presented here, again an update rate of $5dt$ was chosen. Due to the radar data gaps (Figure E.1) this time between subsequent updates can be longer meaning that m which was ideally not larger than 4, can be larger occasionally. The main simulation parameters involved with the LSQ approach applied to the field data are given in table 5.6.

parameter	symbol	unit	value
blind radius	r_0	[m]	250
max. observation radius	r_{max}	[m]	1250
Nr. of observation points in x direction	M	[-]	360
Nr. of observation points in y direction	N	[-]	360
spatial resolution in x direction	dx	[m]	7.5
spatial resolution in y direction	dy	[m]	7.5
time history length for scaling factors		[min]	15
solution update rate		[dt]	5
number of solved wave modes		[-]	1000

Table 5.6: Parameters of wave prediction simulations from radar data

SCALING

The result of the vessel motion from equation 5.11 is still an 'unscaled' value: The observation vector \mathbf{b} in equation 4.27 was taken from I (eq. 5.6) whose interpretation (eq. 5.5) still includes an unknown scaling factor C . This scaling factor is determined by comparing the recorded ship motions by the MRU and the nowcast of the vessel motions. In fact, since 6 different motion modes are predicted and recorded, 6 scaling factors can be determined: At each update step, the variance of both the recorded shipmotion for mode i and the nowcast is determined over the recent history of both quantities. With x_i^* being the history of the nowcast ($\tau = 0$) of the vessel motion and $x_{i,MRU}$ being the history of the recorded motion by the MRU, the scaling factor C is determined as follows:

$$C_i = \sqrt{\frac{\sigma_{x_{i,MRU}}^2}{\sigma_{x_i^*}^2}} \quad (5.12)$$

where σ^2 refers to variance.

For the length of the used history over which the variances were determined at each update, 15 minutes was taken.

Ideally, under the assumption that C_i is frequency independent, C_i would be equal for all 6 motion modes i , at least if there is some overlap between the frequency band containing wave energy and the frequency band with non-zero motion transfer function amplitudes. Using a motion mode dependent scaling factor however, possibly partly solves the issue of inaccurate motion transfer functions.

5.6. RESULTS AND DISCUSSION

The procedures described in paragraph 5.5.2 and 5.5.1 have been applied to the 3 field data sets. The results will be presented in this section.

5.6.1. 15 MINUTES SPECTRA AND SCALING FACTORS

For all six DOF, unscaled nowcast time traces of the motions were constructed. At every update, the scaling factors C_i for each DOF ($i \in [1, 6]$) were obtained using the most recent 15 minutes history of the constructed nowcast. The variances used in equation 5.12 were obtained by integrating the spectra obtained over these 15 minutes histories. As an example, normalized versions of the nowcast and MRU-recorded heave motion spectra from data set 2 are presented in figure 5.5. The scaling factor (C_3) is associated with the right hand side axis in figure 5.5. As can be seen, the spectral shape of nowcast and recorded spectrum match fairly well. It should be kept in mind that the vessel's RAO's have the effect of a low-pass filter and the result could be less good if it were the wave elevation that would be compared. However, the result justifies the choice of using a frequency independent scaling factor. (Borge et al. [2004] illustrated the need of a frequency dependent scaling factor to match the 1D wave spectrum obtained from 3DFFT applied to radar data with that obtained from a buoy measurement. A logical explanation could be the fact that tilt modulation was not modeled. (However, earlier work (Borge and Soares [2000]) did show a good match throughout the entire frequency range without modeling tilt modulation and without a frequency dependent scaling fac-

tor obtained from a reference measurement.) The scaling factor C is associated with the right hand side axis in figure 5.5. For all 3 data sets, figures such as 5.5 are presented in Appendix I for all six DOF. Overall a good agreement is observed between the normalized measured and nowcast spectra and the scaling factors C_i have fairly similar values for the different DOF's. An exception to these statements however, is the roll motion. A likely explanation for this is the fact that no attempts were made to model any of the non-linearities that are known to be involved with the roll motion: roll motion was calculated like the 5 other motion modes by the linear transfer function approach. Besides, the vessel was known to be using various anti-roll devices. It was not possible to verify how well their effect is reflected by the available transfer functions, which were provided by the vessel owner.

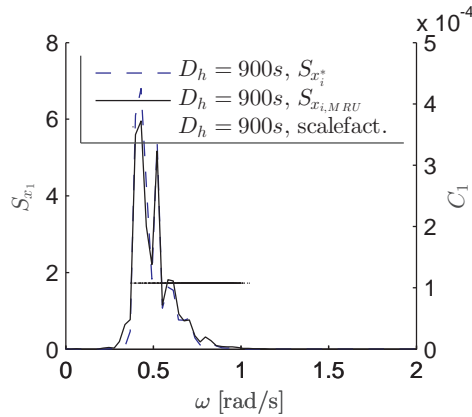


Figure 5.5: Example of 15 minutes spectrum of nowcast ($S_{x_1^*}$) and measurement ($S_{x_1,MRU}$) of surge motion from data set 2 and derived scaling factor C_1

5.6.2. NOWCAST ACCURACY

After having constructed the time trace of the nowcast of all 6 motions, a comparison could be made with the motions as recorded by the MRU.

First of all, in order to detect a possible time lag between nowcast from radar data and measured motions, a cross correlation was determined between each of the two signals, defined as follows:

$$\rho_{x_i^*, x_{i,MRU}}(\tau_{cc}) = D_t^{-1} \int_0^{D_t} \frac{x_i^*(t) - \overline{x_i^*}}{\sigma_{x_i^*}} \cdot \frac{x_{i,MRU}(t + \tau_{cc}) - \overline{x_{i,mru}}}{\sigma_{x_{i,mru}}} dt \quad (5.13)$$

Here, x_i^* and $x_{i,MRU}$ again indicate the nowcast and measurement of motion i respectively. The upper bar denotes the mean and σ denotes the standard deviation. τ_{cc} denotes the applied time shift between the two signals. The correlations are taken over the data set duration, denoted by D_t . An example is shown in figure 5.6, showing the correlation between the nowcast and the recorded surge motion as a function of the applied

time shift τ_{cc} from data set 2. Although it is very well possible that these two data sources were not perfectly synced, such asynchronization is not necessarily the only explanation for the time shift at which maximum correlation occurs. A time shift could also be explained by an imperfection in the interpretation of the radar data: the assumption that it is the pure *tilt* that is observed would in the theoretical case of an harmonic wave result in a time difference of a quarter of the wave period compared to the assumption that we would observe the *elevation*. Possibly, neither of these assumptions represents a *perfect* representation. However, assuming that a quarter of the period of a single harmonic wave is more or less equivalent to a quarter of the peak wave period for the considered cases, only approximately 3 seconds of the found time shift could be explained by a possible misinterpretation associated with the used modeling.

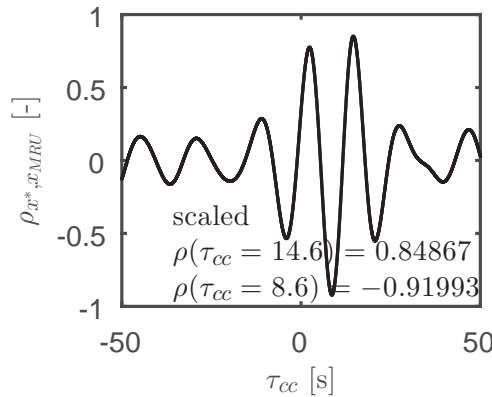


Figure 5.6: Cross correlation between nowcast (x_1^*) and measurement ($x_{1,MRU}$) of surge motion, data set 2

Appendix J presents cross correlations for the three data sets for all 6 motions. Maximum and minimum values of the cross correlations for all motion modes for the 3 data sets are also listed in table 5.7 in which $\tau_{cc,max}$ and $\tau_{cc,min}$ refer to the time shifts associated with the maximum and minimum correlation values respectively and ρ denotes the correlation values. As can be observed in Appendix J and table 5.7, in quite some cases the absolute value of the minimum cross correlation is significantly larger than the maximum cross correlation. (This is also the case in the example shown in figure 5.6.) A possible explanation for this could be a reversed orientation of the motion sensor. However, the results show to be inconsistent over the 3 data sets and among the motion modes: for data set 1 the maximum correlation peaks have higher absolute values than the minimum troughs. For data set 2 and 3 however it is the other way around, except for pitch motion in data set 2. A fully consistent explanation for the higher absolute correlation trough values could not be established. In the proceeding, the time shifts associated with the positive correlation peaks were used for further analysis.

Having determined the time shift τ_{cc} resulting in maximum correlation between MRU recording and nowcast, time traces were plotted taking into account this shift. A sample of a comparison for the surge motion for data set 2 is presented in figure 5.7. As can be seen a good phase resolved match is obtained and time windows (groups) of

(a) Data set 1				
	$\tau_{cc,max}$	$\rho(\tau_{cc,max})$	$\tau_{cc,min}$	$\rho(\tau_{cc,min})$
surge	12.90	0.71	7.75	-0.67
sway	13.00	0.76	7.75	-0.73
heave	12.90	0.77	7.85	-0.73
roll	11.85	0.64	6.40	-0.61
pitch	13.10	0.58	17.55	-0.53
yaw	13.00	0.59	17.55	-0.52

(b) Data set 2				
	$\tau_{cc,max}$	$\rho(\tau_{cc,max})$	$\tau_{cc,min}$	$\rho(\tau_{cc,min})$
surge	14.60	0.85	8.60	-0.92
sway	14.15	0.83	8.45	-0.86
heave	14.05	0.86	8.60	-0.87
roll	1.95	0.69	8.35	-0.71
pitch	14.30	0.85	9.30	-0.76
yaw	14.25	0.81	9.00	-0.82

(c) Data set 3				
	$\tau_{cc,max}$	$\rho(\tau_{cc,max})$	$\tau_{cc,min}$	$\rho(\tau_{cc,min})$
surge	13.30	0.83	7.45	-0.89
sway	12.95	0.72	7.25	-0.78
heave	12.85	0.79	7.30	-0.86
roll	1.25	0.41	7.20	-0.38
pitch	12.75	0.82	7.80	-0.86
yaw	12.85	0.77	7.60	-0.83

Table 5.7: Minimum and maximum nowcast cross correlations

low and high motions in both signals are matching very accurately. Appendix K presents sample time traces of the nowcast for the 3 data sets for all motion modes.

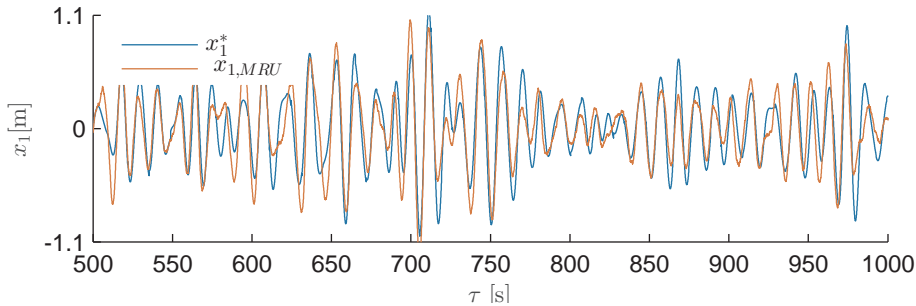


Figure 5.7: Sample time trace of nowcast and MRU measurement of surge motion, data set 2

In general it can be stated that a very significant correlation between nowcasted and measured motions was found, again with the exception of the roll motion. The nowcast accuracy was not consistent over the the different data sets however: data set 1 resulted in significantly lower accuracy. Data set 2 yielded the best results. A sound explanation for the differences in accuracy between the 3 data sets is not provided here. What can be said is that the condition during data set 2 involved the highest waves (significant double amplitudes of the heave motion amounted to 2.6, 3.1 and 2.4 m for data set 1, 2 and 3 respectively). From examining time traces of now cast and measured motion (Appendix K) it can be observed that the accuracy is higher during periods with high motions than during periods with lower motions, which at least partly 'explains' the best accuracy for data set 2. Also data set 2 involved the longest waves, and data set 1 the shortest. (see table 5.5). In the investigations in chapter 4 LSQ was indeed shown to perform better at longer waves, at least for short prediction times. Differences between the encountered wave periods during the 3 data sets are small however. However, many other factors can affect the accuracy of ship motion predictions from radar back scatter, an important one of which is assumed to be the radar back scatter 'quality' (sufficient surface roughness, mostly affected by local wind). Also motion transfer function accuracy (and its sensitivity to the wave direction) are likely to have a significant effect. A thorough investigation to reveal the reason for the found differences in nowcast (and forecast) accuracy among the 3 data set is left as a recommendation.

5.6.3. PREDICTION ACCURACY

Knowing the time shift associated with maximum nowcast cross correlation, $\tau_{cc,max}$, from the analysis presented in the previous paragraph, *prediction* time traces were compared to measured motions as well and correlation of the motion prediction as a function of the prediction time τ was considered. This correlation $corr_{x_i}(\tau)$ is computed as:

$$corr_{x_i}(\tau) = D_t^{-1} \int_0^{D_t} \frac{x_i(t, \tau) - \overline{x_i(t, \tau)}}{\sigma_{x_i}(\tau)} \cdot \frac{x_{i,MRU}(t + \tau_{cc,max}) - \overline{x_{i,mru}}}{\sigma_{x_{i,mru}}} dt \quad (5.14)$$

Figure 5.8 shows the correlation of the surge motion prediction as a function of prediction time τ from data set 2, together with the wave predictability indicator $P.I.(\tau)$, the latter being associated with the right hand side vertical axes. Appendix L, shows similar figures for all motion modes and for the remaining data sets.

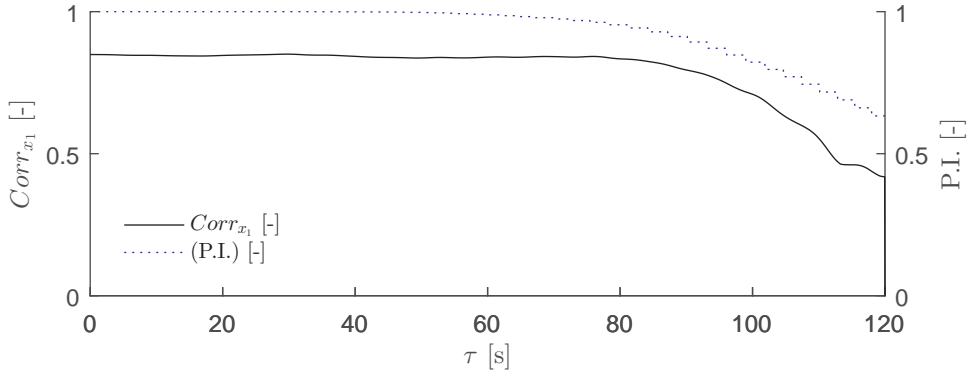


Figure 5.8: Correlation of prediction of surge motion, data set 2

(The prediction correlation for $\tau = 0$ is what was referred to as the 'nowcast' and its values were listed in table 5.7.) As can be seen figure 5.8 and all figures in Appendix L, the correlation of the prediction stays fairly constant approximately upto the value of $\tau = 80$ where $P.I.$ starts to decrease. Again $P.I.$ is shown to be a reasonably good indicator for the maximum prediction horizon.

It can be argued that for many practical offshore operations, it would not necessarily be the exact phase resolved deterministic motion behavior that is anticipated on for the timing of motion critical phases of the operation, but rather the 'group' behavior: a critical phase is postponed until a sufficiently long time window with sufficiently low motions occurs. Whether the exact phasing of the prediction within such a period is accurate, is less relevant. With this in mind, the accuracy of the predicted motion groups was quantified. This was done by computing the correlation of the *envelopes* of the motion, defined as the absolute value of the Hilbert transform:

$$\tilde{x}_i(t, \tau) = |H(x_i(t, \tau))| \quad (5.15)$$

where \tilde{x}_i denotes the envelope of motion x_i (for a fixed chosen prediction time τ) and H denotes the Hilbert transform.

The correlation of the envelope of the prediction is significantly higher than the correlation of the prediction itself. This is illustrated by figure 5.9: it shows the correlation of the heave prediction and its envelope. As can be seen, the heave prediction envelope

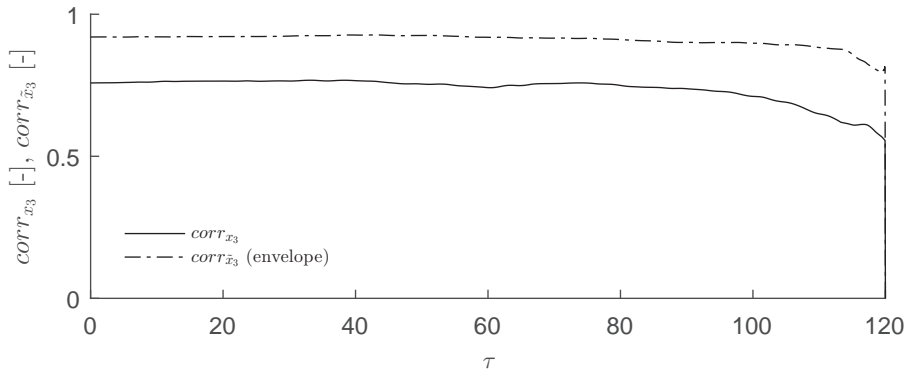


Figure 5.9: Correlation of prediction and envelope prediction of heave motion, data set 1

shows a high correlation while, as for all motion modes in data set 1, the correlation of the heave prediction itself is rather low. Results for all other motion modes and all data sets can be found in Appendix M.

5.7. CONCLUSIONS

From the presented investigations using the OWME field data, the following conclusions can be drawn:

- Vessel motions, predicted from a linear wave field representation with component amplitudes solved by the LSQ approach as proposed in chapter 4, show a very significant correlation with recorded motions.
- Prediction accuracy is fairly constant upto prediction horizons that do not exceed the predictability limits associated with the considered sea state (as defined by the predictability indicator $P.I.$).
- As can be expected, the linear approximation is not adequate to obtain a roll motion accuracy that matches the other motions: a non linear approach for roll is recommended.
- The accuracy, expressed by the correlation coefficient, of the predicted motion envelope is significantly higher than that of the predicted motion itself.

6

CONCLUSIONS AND RECOMMENDATIONS

In this final chapter, the main conclusions and recommendations for further work based on this study will be presented.

- From the investigations into the relation between the spatio-temporal observation domain and the related prediction horizon, it could be concluded that the maximum forecast horizon for phase-resolved wave prediction is governed by the group velocity of the waves.
- Although being an established technique to reveal the directional wave spectrum and surface current from radar images, 3D FFT combined with dispersion filtering is not suitable for deterministic wave prediction: From a wave field decomposition obtained by 3DFFT no accurate phase resolved wave prediction outside the observation domain can be obtained.
- It was shown that dynamically averaging of subsequent prediction updates leads to a prediction accuracy that is significantly higher than the accuracy of the observation of the waves itself.
- For the decomposition of the waves into a linear representation by a set of directional wave modes, both an approach using 2D FFT and one based on least squares minimization (LSQ) have proven successful from simulations with synthetic input data. For the latter, a convincing proof of concept has been obtained from a validation study with actual *field data*.

6

For the decomposition into wave modes, the proposed LSQ approach has been shown to be *potentially* superior to the investigated alternatives in a wide range of conditions, its main advantages being that it can deal with counter propagating waves that can occur in multi-model sea states and that it has been shown to be a feasible approach at low antenna speed. The reason why the word 'potentially' still has to be included in this statement is related to some remaining issues that are recommended here to be addressed:

- The computational burden involved with the LSQ approach currently prevents its real time application. A fast solver for the LSQ problem and efficient implementation, probably involving the use of GPU are needed to develop this technique from its current state of proof of principle to an operational tool.
- In order to either reduce the computational burden or increase the accuracy, it is recommended to improve the selection of the wave modes to be solved: especially for wave conditions whose energy is widely spread over the wave number space (having a large 'footprint'), reducing the resolution in the wave number space is expected give large improvements. Research into automatic optimization of the condition specific trade-off between resolution and covered footprint in the wave number space is recommended.
- Under the restriction of the size of the minimization problem solved with the LSQ approach in terms of input observations, choices concerning spatial and temporal resolution will affect the accuracy as was illustrated in paragraph 4.5.3. Deeper

investigations into this phenomenon could lead to an automated optimization of the chosen input, thus optimizing the prediction accuracy due to this aspect.

As concluded, the presented proof of concept from the application of the developed LSQ approach on field data can be considered to be convincing in general. Nevertheless, significant differences in the accuracy were observed between results for different data sets in chapter 5, despite the fact that they all concern the same ship with the same radar system at the same location: thorough investigations into what affects the performance of the approach are recommended in order to increase its robustness.

It was observed from the validation with the field data in chapter 5 that the accuracy of roll motion predictions was significantly lower than that of the remaining 5 motion modes. This doesn't come as a surprise since mainly due to the possibly quite non-linear damping, computation of roll-motion is notoriously more inaccurately approximated by a linear transfer function approach than the remaining motion modes. At the same time, from an operational point of view its effect on workability can be a decisive factor. It is therefore recommended to investigate ways to improve the accuracy of the roll motion response that meet the requirement of real time applicability involved with the operational (real-time on-board) application of deterministic wave and motion prediction.

A final recommendation concerns definition of the prediction accuracy. Throughout this study, the *correlation* of the wave elevation and the motion response was used to quantify the accuracy. A slightly more pragmatic accuracy quantifier was already introduced by considering the *envelopes* of predicted properties. From an operational point of view, it can be argued that a more meaningful quantification of the accuracy should be related to the specific operational criteria: e.g. the statistics of erroneously predicted workable time windows (and/or erroneously predicted exceeding of operational limits) would probably be more useful in order to decide whether or not to rely on the deterministic prediction for operational decision support. In practice, with many factors affecting the prediction accuracy, it will be challenging to obtain such an operational accuracy quantification with sufficient statistical reliability. Nevertheless, for the acceptance by potential users of decision support based on deterministic prediction, this aspect is important enough for further investigations.

REFERENCES

- L Abusedra and M R Belmont. Prediction diagrams for deterministic sea wave prediction and the introduction of the data extension prediction method. *International Shipbuilding Progress*, 58:59–81, 2011.
- Leon Adegeest. Short - term motion prediction of navy vessels in heavy weather. Technical report, Ministry of Defence the Netherlands, Report 20130624, 2013.
- Laura K Alford, Robert F Beck, Joel T Johnson, David Lyzenga, Okey Nwogu, and Alan Zundel. Design , Implementation , and Evaluation of a System for Environmental and Ship Motion Forecasting. In *30th Symposium on Naval Hydrodynamics*, number November, pages 2–7, Hobart, Tasmania, Australia, 2014.
- Laura K Alford, Robert F Beck, Joel T Johnson, David Lyzenga, Okey Nwogu, and Alan Zundel. A Real-Time System for Forecasting Extreme Waves and Vessel Motions. In *Proceedings of the ASME 2015 34th International Conference on Ocean, Offshore and Arctic Engineering*, volume 11, pages 1–8, 2015.
- Werner R. Alpers, Duncan B. Ross, and Clifford L. Rufenach. On the Detectability of Ocean Surface Waves by Real and Synthetic Aperture Radar. *JOURNAL OF GEOPHYSICAL RESEARCH*, 86(C7):6481–6498, 1981.
- Sina Aragh. *Radar Data Assimilation And Forecasts Of Evolving Nonlinear Wave Fields*. PhD thesis, University of Michigan, 2007.
- Sina Aragh, Okey Nwogu, and David Lyzenga. Improved Estimation of Ocean Wave Fields from Marine Radars Using Data Assimilation Techniques. In *ISOPE*, 2008.
- Robert F Beck. Final Report - Optimum Vessel Performance in Evolving Nonlinear Wave Fields. Technical Report 350, Office of Naval Research (ONR), 2012.
- M R Belmont, J Christmas, J Dannenberg, and B Ferrier. An Examination of the Feasibility of Linear Deterministic Sea Wave Prediction in Multi-Directional Seas Using Wave Profiling Radar : Theory , Simulation and Sea Trials. *Journal of Atmospheric and Oceanic Technology*, 31(7):1601–1614, 2014.
- E Blondel and P Naaijen. Reconstruction And Prediction Of Short-crested Seas Based On The Application Of A 3d-fft On Synthetic Waves. Part 2: Prediction. In *Proceedings of the 31st International Conference on Ocean, Offshore and Arctic Engineering*, 2012.
- E Blondel, G Ducrozet, F Bonnefoy, and P Ferrant. Extreme Wave Characterization and Prediction using an Advanced Higher-Order Spectral (HOS) Model. In *27th Symposium on Naval Hydrodynamics Seoul, Korea*, number October, pages 5–10, 2008.

- E. Blondel, F. Bonnefoy, and P. Ferrant. Deterministic non-linear wave prediction using probe data. *Ocean Engineering*, 37(10):913–926, 2010a.
- E. Blondel, F. Bonnefoy, and P. Ferrant. Experimental Validation of Deterministic Non-linear Wave Prediction Schemes in 2D. In *Proceedings of the 20th (2010) International Offshore and Polar Engineering Conference (ISOPE2010), Beijing, China, 2010b*.
- J. C. Nieto Borge and C. Guedes Soares. Analysis of directional wave fields using X-band navigation radar. *Coastal Engineering*, 40:375–391, 2000.
- J. C. Nieto Borge, Konstanze Reichert, and Jürgen Dittmer. Use of nautical radar as a wave monitoring instrument. *Coastal Engineering*, 37(3-4):331–342, 1999.
- J. C. Nieto Borge, G. Rodriguez Rodriguez, Katrin Hessner, and Paloma Izquierdo Gonza Lez. Inversion of Marine Radar Images for Surface Wave Analysis. *Journal Of Atmospheric And Oceanic Technology*, 21:1291–1300, 2004.
- J. R. Buckley and J. Aler. Enhancements in the determination of ocean surface wave height from grazing incidence microwave backscatter. In *Proceedings of IEEE IGARS*, pages 2487–2489, 1998.
- CAA. CAA Paper 2008/03 Helideck Design Considerations - Environmental Effects. 2008. URL <http://www.hse.gov.uk/offshore/infosheets/is5-2011.htm>.
- F. Clauss, Marco Klein, Matthias Dudek, Miguel Onorato, Dipartimento Fisica, and Università Torino. Deterministic Non-Linear Wave Forecast and Motion Prediction for Short-Term Offshore Operations. In *ISOPE*, 2015.
- G. F. Clauss, S. Kosleck, and D. Testa. Critical Situations of Vessel Operations in Short Crested Seas - Forecast and Decision Support system. In *Proceedings of the ASME 2009 28th International Conference on Ocean, Offshore and Arctic Engineering*, 2009.
- G. F. Clauss, Sascha Kosleck, and Daniel Testa. Critical Situations of Vessel Operations in Short Crested Seas - Forecast and Decision Support System. *J. Offshore Mechanics and Arctic Engineering*, 134(3):15, 2012.
- Benjamin S. H. Connell, William M. Milewski, Jason P. Rudzinsky, John G. Kusters, Christopher S. Brundick, and Gordon Farquharson. Development of an environmental and ship motion forecasting system. In *Proceedings of the ASME 2015 34th International Conference on Ocean, Offshore and Arctic Engineering OMAE2015*, pages 1–11, 2015.
- H. Dankert and W. Rosenthal. Ocean surface determination from X-band radar-image sequences. *J. Geophys. Res.*, 109(C4):C04016, 2004.
- Jens Dannenberg, Peter Naaijen, and Konstanze Reichert. The On Board Wave and Motion Estimator OWME. In *Proceedings of the Twentieth (2010) International Offshore and Polar Engineering Conference*, volume 7, pages 424–431, 2010. ISBN 9781880653777.

- D R Edgar, J M K Horwood, R Thurley, and M R Belmont. The Effects Of Parameters On The Maximum Prediction Time Possible In Short Term Forecasting Of The Sea Surface Shape. *International Shipbuilding Progress*, 47(451):287–301, 2000.
- R Gangeskar. An algorithm for estimation of wave height from shadowing in X-band radar sea surface images. *IEEE Trans. Geosci. Remote Sens.*, 52:3373–3381, 2014.
- Yoshimi Goda. *Random Seas And Design Of Maritime Structures*. World Scientific, 2010.
- S T Grilli, C Guerin, and B Goldstein. OceanWave Reconstruction Algorithms Based on Spatio-temporal Data Acquired by a Flash LIDAR Camera. In *Proceedings of ISOPE*, 2011.
- K Hessner, K Reichert, and W Rosenthal. Mapping Of Sea Bottom Topography In Shallow Seas By Using A Nautical RadarHe. In *2nd International Symposium on Operationalization of Remote Sensing, Enschede, The Netherlands, 16-20 August, 1999*, 1999.
- T Hilmer and E Thornhill. Deterministic wave predictions from the WaMoS II. In *OCEANS 2014 - TAIPEI*, pages 1–8, apr 2014.
- P. Hooeboom and W. Rosenthal. Directional wave spectra in radar images. In *Int. Geosci. Remote Sens. Symp., IEEE*, Munich, 1982.
- T T Janssen, A R Van Dongeren, and C Kuiper. Phase resolving analysis of multidirectional wave trains. In *Proceedings of the Fourth International Symposium Waves 2001, San Francisco, CA*, 2001.
- E R Jefferys. Directional seas should be ergodic. *Applied Ocean Research*, 9(4):186–191, 1987.
- P H Y Lee, J D Barter, K L Beach, C L Hindman, B M Lake, H Rungaldier, J C Shelton, A B Williams, R Yee, and H C Yuen. X band microwave backscattering from ocean waves. *Journal of Geophysical Research: Oceans*, 100(C2):2591–2611, 1995.
- D Lyzenga, O Nwogu, D Trizna, and K Hathaway. Ocean wave field measurements using X-band Doppler radars at low grazing angles. In *Geoscience and Remote Sensing Symposium (IGARSS), 2010 IEEE International*, pages 4725–4728, 2010.
- E L Morris, H K Zienkiewicz, and M R Belmont. Short term forecasting of the sea surface shape. *International Shipbuilding Progress*, 45:383–400, 1998.
- J D Murray. *Asymptotic analysis*. Oxford University Press, 1974.
- P Naaijen and E Blondel. Reconstruction And Prediction Of Short-crested Seas Based On The Application Of A 3d-fft On Synthetic Waves. Part 1: Reconstruction. In *Proceedings of the 31st International Conference on Ocean, Offshore and Arctic Engineering*, 2012.
- P Naaijen and R H M Huijsmans. Real Time Wave Forecasting For Real Time Ship Motion Predictions. In *Proceedings of the ASME 2008 27th International Conference on Ocean, Offshore and Arctic Engineering*, 2008.

- P. Naaijen and R. H. M. Huijsmans. Real Time Prediction of Second Order Wave Drift Forces for Wave Force Feed Forward in DP. *29th International Conference on Ocean, Offshore and Arctic Engineering: Volume 4*, pages 357–364, 2010.
- P Naaijen, R R T van Dijk, R H M Huijsmans, and A A El-Mouhandiz. Real time estimation of ship motions in short crested seas. In *Proceedings of the ASME 2009 28th International Conference on Ocean, Offshore and Arctic Engineering*, 2009.
- P Naaijen, K Trulsen, and E Blondel-Couprie. Limits to the extent of the spatio-temporal domain for deterministic wave prediction. *International Shipbuilding Progress*, 61: 203–223, 2014.
- Peter Naaijen and A P Wijaya. Phase Resolved Wave Prediction from Synthetic Radar Images. In *Proceedings of the 33rd International Conference on Ocean, Offshore and Arctic Engineering*, volume 23470, 2014.
- F Nouguiet, S T Grilli, and C A Guerin. Nonlinear Ocean Wave Reconstruction Algorithms Based on Simulated Spatiotemporal Data Acquired by a Flash LIDAR Camera. *Ieee Transactions on Geoscience and Remote Sensing*, 52(3):1761–1771, 2014.
- ONR. Environmental and Ship Motion Forecasting (ESMF), 2010.
- H M Oudshoorn. The use of radar in hydrodynamic surveying. In *7th Coastal Engng. Conf.*, pages 59–76, 1960.
- M Paalvast, P Naaijen, and R H M Huijsmans. Propagation Of A Radar Modulated Ocean Wave Field. In *Proceedings of ASME 2014 33rd International Conference on Ocean, Offshore and Arctic Engineering*, 2014.
- William J Plant and Gordon Farquharson. Wave shadowing and modulation of microwave backscatter from the ocean. *Journal of Geophysical Research: Oceans*, 117 (C8):n/a—n/a, 2012.
- J. Seemann, F Ziemer, and C.M. Senet. A method for computing calibrated ocean wave spectra from measurements with a nautical X-band radar. *Oceans '97. MTS/IEEE Conference Proceedings*, 2:1148–1154, 1997.
- C M Senet, J Seemann, and F Ziemer. The near-surface current velocity determined from image sequences of the sea surface. *Geoscience and Remote Sensing, IEEE Transactions on*, 39(3):492–505, 2001.
- C M Senet, J Seemann, S Flampouris, and F Ziemer. Determination of Bathymetric and Current Maps by the Method DiSC Based on the Analysis of Nautical X-Band Radar Image Sequences of the Sea Surface (November 2007). *Geoscience and Remote Sensing, IEEE Transactions on*, 46(8):2267–2279, 2008.
- Christian M Senet, Jorg Seemann, and Fhedwart Zaemer. An iterative technique to determine the near surface current velocity from time series of sea surface images. In *Proc. Oceans MTS/IEEE Conf.—500 Years of Ocean Exploration*, pages 66–72, 1997.

- F Serafino, C Lugni, and F Soldovieri. A Novel Strategy for the Surface Current Determination From Marine X-Band Radar Data. *Geoscience and Remote Sensing Letters, IEEE*, 7(2):231–235, apr 2010.
- Lev Shemer, Anna Sergeeva, and Alexey Slunyaev. Applicability of envelope model equations for simulation of narrow-spectrum unidirectional random wave field evolution: Experimental validation. *Physics of Fluids*, 22(1):16601, 2010.
- G E Smith, N Majurec, A O'Brien, J Pozderac, C J Baker, J T Johnson, D R Lyzenga, O Nwogu, D B Trizna, D Rudolf, and G Schueller. High power coherent-on-receive radar for marine surveillance. *Radar (Radar), 2013 International Conference on*, pages 434–439, 2013.
- K Trulsen. Spatial Evolution Of Water Surface Waves. In *Fifth International Symposium WAVES 2005*, Madrid, 2005.
- K Trulsen and C T Stansberg. Spatial Evolution of Water Surface Waves: Numerical Simulation and Experiment of Bichromatic Waves. In *Proceedings of the Eleventh (2001) International Offshore and Polar Engineering Conference*, Stavanger, 2001.
- G R Venzuela. Scattering of electromagnetic waves from a tilted slightly rough surface. *Radio Science*, 3:1057, nov 1968.
- Lewis B Wetzel. Electromagnetic Scattering from the Sea at Low Grazing Angles. In G L Geernaert and W L Plant, editors, *Surface Waves and Fluxes: Volume II — Remote Sensing*, pages 109–171. Springer Netherlands, Dordrecht, 1990.
- A P Wijaya and E van Groesen. Significant wave height retrieval from synthetic radar images. In *Proceedings of the 11th International Conference on Hydrodynamics (ICHHD 2014)*, page 44, Singapore, 2014. Maritime Research Centre, Nanyang Technological University.
- A.P. Wijaya and E. van Groesen. Determination of the significant wave height from shadowing in synthetic radar images. *Ocean Engineering*, 114:204–215, mar 2016. ISSN 00298018. doi: 10.1016/j.oceaneng.2016.01.011. URL <http://www.sciencedirect.com/science/article/pii/S0029801816000226>.
- A.P. Wijaya, P. Naaijen, Andonowati, and E. van Groesen. Reconstruction and future prediction of the sea surface from radar observations. *Ocean Engineering*, 106:261–270, 2015. URL <http://linkinghub.elsevier.com/retrieve/pii/S0029801815003133>.
- G Wu. *Direct Simulation and Deterministic Prediction of Large-scale Nonlinear Ocean Wave-field*. PhD thesis, Massachusetts Institute Of Technology, 2004.
- I R Young, W Rosenthal, and F Ziemer. A Three-Dimensional Analysis of Marine Radar Images for the Determination of Ocean Wave Directionality and Surface Currents. *Journal of geophysical research*, 90:1049–1059, 1985.

- K.D.S. Zeilstra, A.J.C. de Reus, and J. Koning. Improving offshore helicopter operability & safety Customer. Technical Report February, National Aerospace Laboratory NLR, Netherlands, 2015.
- J. Zhang, J. Yang, J. Wen, I. Prislín, and K. Hong. Deterministic wave model for short-crested ocean waves: Part I. Theory and numerical scheme. *Applied Ocean Research*, 21(4):167–188, 1999.
- F Ziemer and W Rosenthal. On the Transfer Function of a Shipborne Radar for Imaging Ocean Waves. In *Proc. IGARSS'87 Symp. Ann Arbor. Michigan*, pages 1559–1564, 1987.
- F Ziemer, W. Rosenthal, and H. Carlson. Measurements of directional wave spectra by ship radar. In *Assembly International Association for Physical Science of the Ocean (IAPSO)*, Hamburg, 1983.

A

APPENDIX

Depending on the magnitude of Δt , the realizations constructed as shown in figure 2.5 will be dependent, thus the ensemble size required for convergence may be larger than for independent realizations.

In order to assess the required ensemble size for independent realizations, we have synthesized an ensemble of size 700 according to the spectrum of the TUD data mentioned in table 2. We have studied the convergence of the practical prediction error Err at an arbitrary point in the sloped part of the predictable zone.

Figure A.1 shows the average prediction error against the number of realizations for independent realizations. It is anticipated from this figure that the result is sufficiently converged after approximately 600 realizations. Additional examinations at other locations within the spatio-temporal prediction zone led to the same conclusion.

Figure A.2 shows the convergence in the case of partly overlapping sections of one time trace of synthetic data generated as described in the previous paragraph. The dashed lines in figure A.1 and A.2 indicate the value from the entire ensemble of independent realizations in figure A.1. Figure A.2(b) shows results for increased values of Δt . Considering some additional results for other times / locations, it was concluded that the gain in the level of convergence from $\Delta t = 0.25$ compared to $\Delta t = 2.5$ is so limited that it justifies the pragmatic approach of using $\Delta t = 2.5$, resulting in an ensemble size of 500. This level of convergence was considered to be sufficient in order to draw the conclusions within the scope of the presented paper.

Figure A.2 shows the convergence in the case of partly overlapping time traces of the experimental data. The dashed lines indicates the value obtained from averaging over the entire ensemble obtained by using $\Delta t = 0.25$ s, i.e. the last point of figure A.3(a). It is seen that using a Δt of 10 samples (corresponding to 2.5 s) and with 400 overlapping time traces, the same result is obtained as when using a Δt of 1 sample (0.25 s) using roughly 4000 overlapping time traces. We therefore conclude that with the available experimental data, there is no gain in convergence from using a smaller Δt than 10 samples (2.5 s). For Δt of 15 or 20 samples (corresponding to 3.75 s or 5.0 s, respectively), small deviations from the optimally converged result can be observed. Again, for sev-

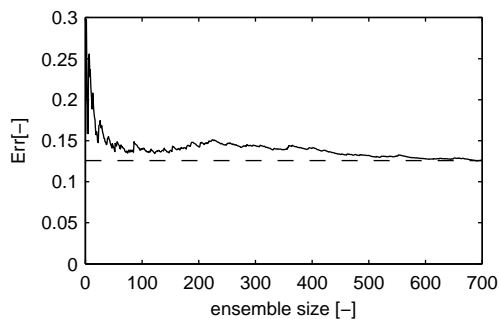


Figure A.1: Prediction error against number of independent realizations.

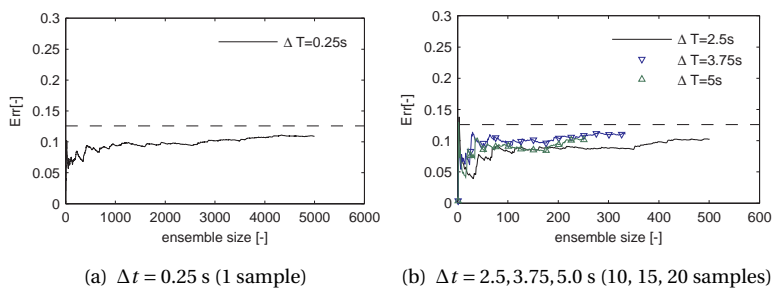


Figure A.2: Prediction error against number of partly overlapping segments, synthetic data.

eral points in the spatio-temporal prediction zone similar investigations were done all of which showed a reasonable level of convergence.

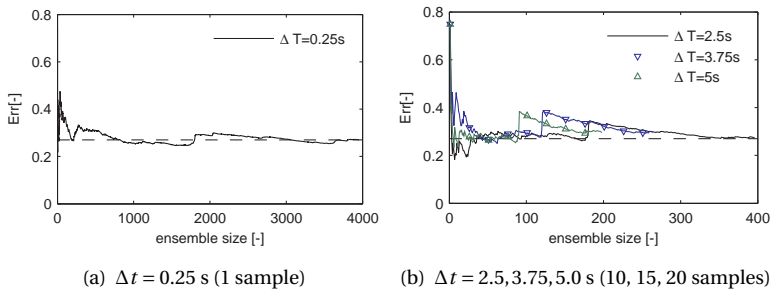
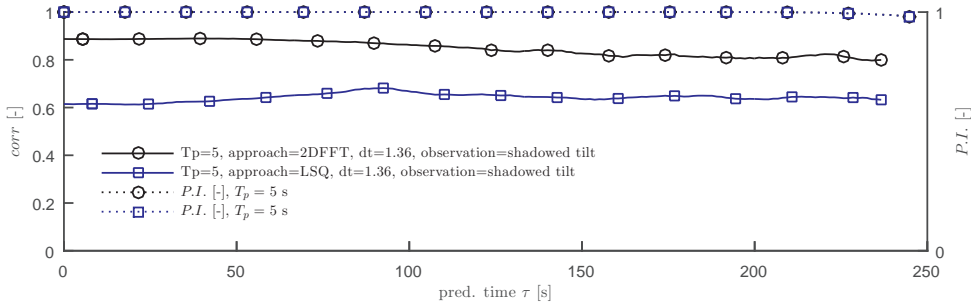


Figure A.3: Averaged prediction error against number of partly overlapping segments, experimental data.

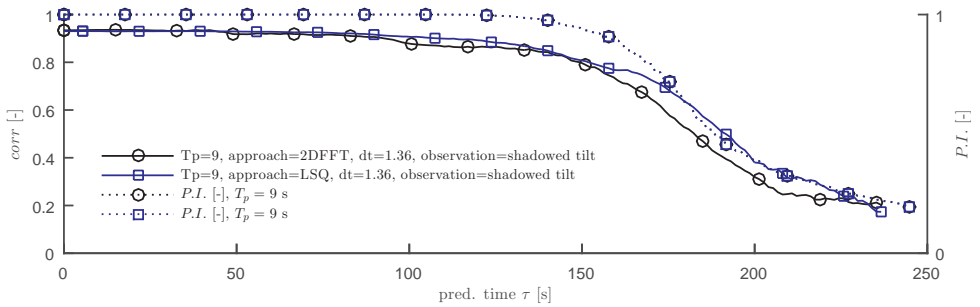
B

APPENDIX

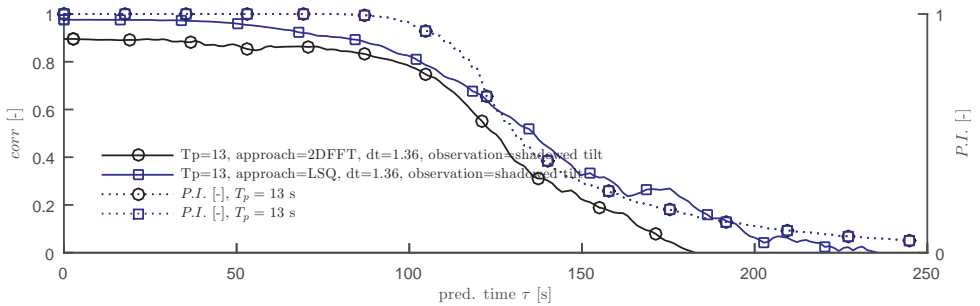
B



(a) Condition 1



(b) Condition 2



(c) Condition 3

Figure B.1: Correlation of predicted wave elevation at the antenna with 2DFFT and LSQ method, for wave condition 1-3

C

APPENDIX

Consider figure 3.2 again, a 2D (space and time) representation of spatio temporal predictability. B indicates the the location of the radar antenna. Distance OB can be considered to be the above mentioned radius R of a circular observation domain. The line connecting $(0, O)$ with (τ_2, B) has a slope equal to the group velocity of the longest wave components in a sea state representing 'significant' energy. At any point (τ, x) below/at the right hand side of this line, some long wave components being part of the spatial observation at OB have passed the considered prediction location x at time τ already. So τ_2 is in this case the maximum prediction horizon at the antenna location B . Choosing a criterion for what is considered 'significant', the required observation distance for a given prediction horizon can be determined. Suppose those low frequency wave components together representing a fraction of the total spectral wave energy of less than α are considered to be 'insignificant'. The frequency of the longest 'significant' wave component, ω_l and α are then related as follows:

$$\alpha = 1 - \frac{\int_0^{2\pi} \int_{\omega_l}^{\infty} S(\omega, \mu) d\omega d\mu}{\int_0^{2\pi} \int_0^{\infty} S(\omega, \mu) d\omega d\mu} \quad (C.1)$$

Let the group velocity associated with ω_l be given by c_{gl} . The minimum observation distance r_{min} required for a chosen prediction time τ is then given by:

$$r_{min} = \tau c_{gl} \quad (C.2)$$

For deep water, a chosen α value of 0.005 and a range of sea states defined by the spectral shape of the Jonswap formulation, peak period T_p and peakedness factor γ , the minimum required observation distance r_{min} is plotted against prediction horizon τ in figure C.1(a). Figure C.1(b) presents a similar plot with the equivalent non-dimensional properties on the axes.

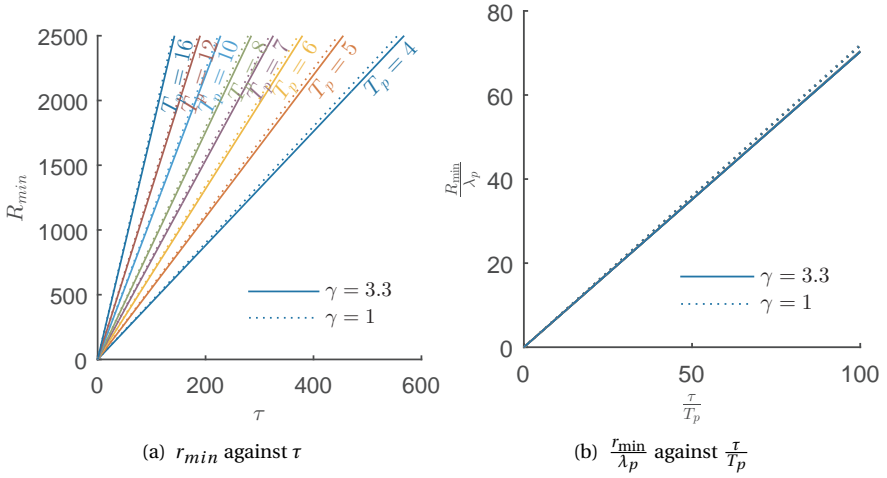


Figure C.1: minimum observation distance against prediction horizon

For deep water equation C.2 can be approximated by:

$$R_{min} = \tau c_{gl} \approx \tau 0.5 \frac{\lambda_l}{T_l} \quad (C.3)$$

From this it follows that:

$$\frac{R_{min}}{\lambda_p} = 0.5 \frac{T_l}{T_p} \frac{\tau}{T_p} \quad (C.4)$$

From the fact that the lines for the different T_p values in figure C.1(b) coincide, it can be concluded that $\frac{T_l}{T_p}$ is independent of T_p . It is found that:

$$\begin{aligned} \frac{T_l}{T_p} &\approx 1.406 \quad \text{for } \gamma = 3.3 \\ \frac{T_l}{T_p} &\approx 1.436 \quad \text{for } \gamma = 1.0 \end{aligned} \quad (C.5)$$

So using $\lambda \approx 1.56T^2$, as a deep water approximation for r_{min} we find:

$$\begin{aligned} R_{min} &\approx 1.09T_p\tau \quad \text{for } \gamma = 3.3 \\ R_{min} &\approx 1.12T_p\tau \quad \text{for } \gamma = 1.0 \end{aligned} \quad (C.6)$$

D

APPENDIX

D

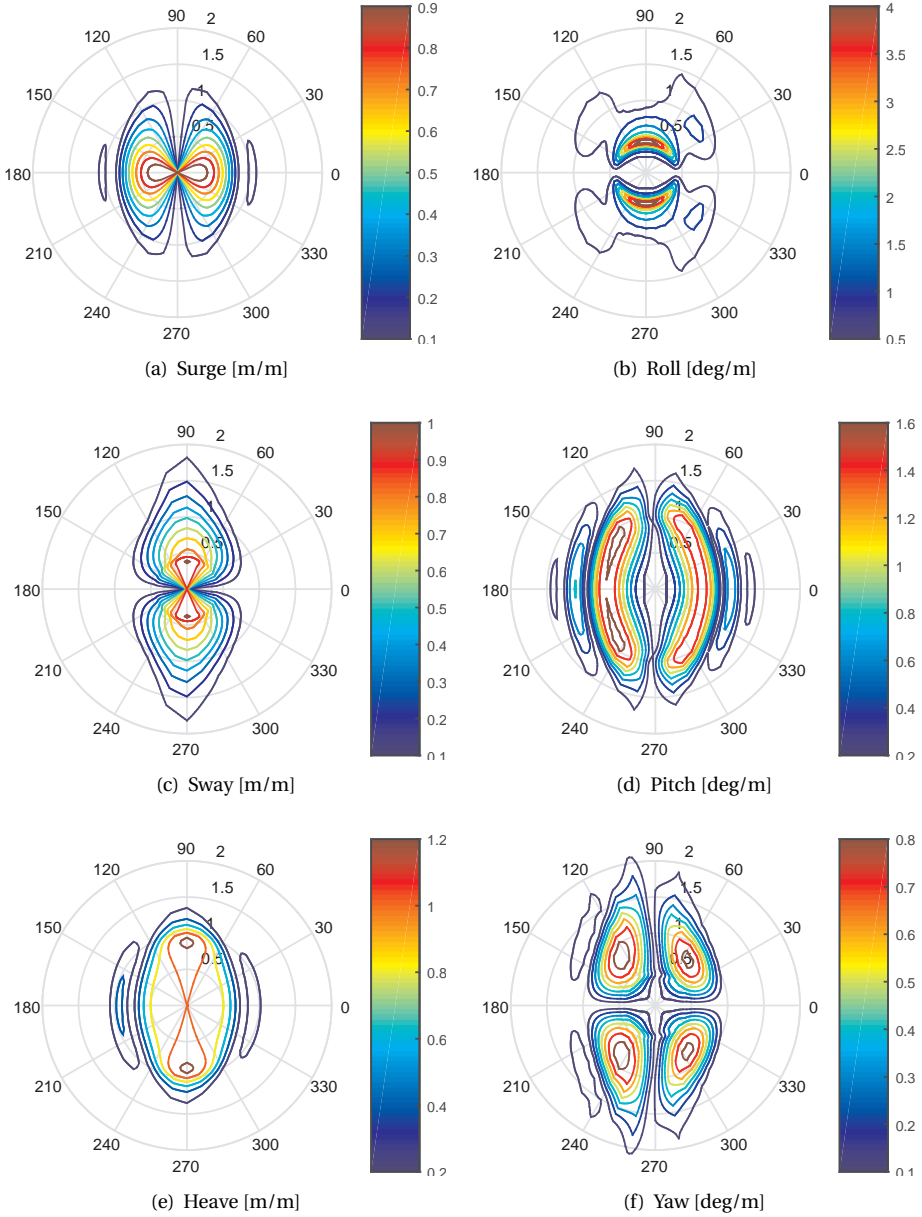


Figure D.1: polar representation of vessel RAO's as a function of wave direction relative to vessel [deg] and wave frequency [rad/s] (wave direction defined relative to vessel x-axis pointing to the bow, such that)

E

APPENDIX

This Appendix aims to illustrate that the standard deviation of synthetic radar backscatter will include a range dependent effect, when this standard deviation is obtained from a shadowed observation, even though the synthetic unshadowed backscatter itself does not contain any range dependency.

For the sake of simplicity:

- Synthetic backscatter is here modeled as $\partial_r \eta$ without any offset or factor and therefor the standard deviation of the backscatter modeled this way is range independent.
- The backscatter from a regular wave is considered. Clearly, shadowing is a non-linear phenomenon to which no superposition principle can be applied. However, as a qualitative investigation, considering a harmonic wave profile is an adequate approach.

Let the wave surface be observed at horizontal distance r_0 from an antenna positioned at height Λ above the mean surface and let's consider over what part of its length it will be visible. The harmonic wave profile is written as:

$$\eta(r) = A \cos(k(r - r_0 + \xi)) \quad (\text{E.1})$$

Here ξ is a horizontal shift (to the left) of the harmonic wave profile.

Obviously, when the angle $\pi/2 - \Theta$ of the line of sight from the antenna to the surface at r_0 with the horizontal is more than the maximum wave steepness, the wave will be visible over its entire length. This is the case when $r_0 < \frac{\Lambda}{Ak}$. See figure E.1(a). Let ξ_l be the shift that the wave profile can make until the part where $r > r_0$ becomes shadowed. Equating the slope of $\eta(r)$ at $r = r_0$ with the gradient of the antenna's line of sight ($-\tan(\pi/2 - \Theta)$) yields:

$$kr_0 \sin(k\xi_l) = \frac{\Lambda}{A} - \cos(k\xi_l) \quad (\text{E.2})$$

E

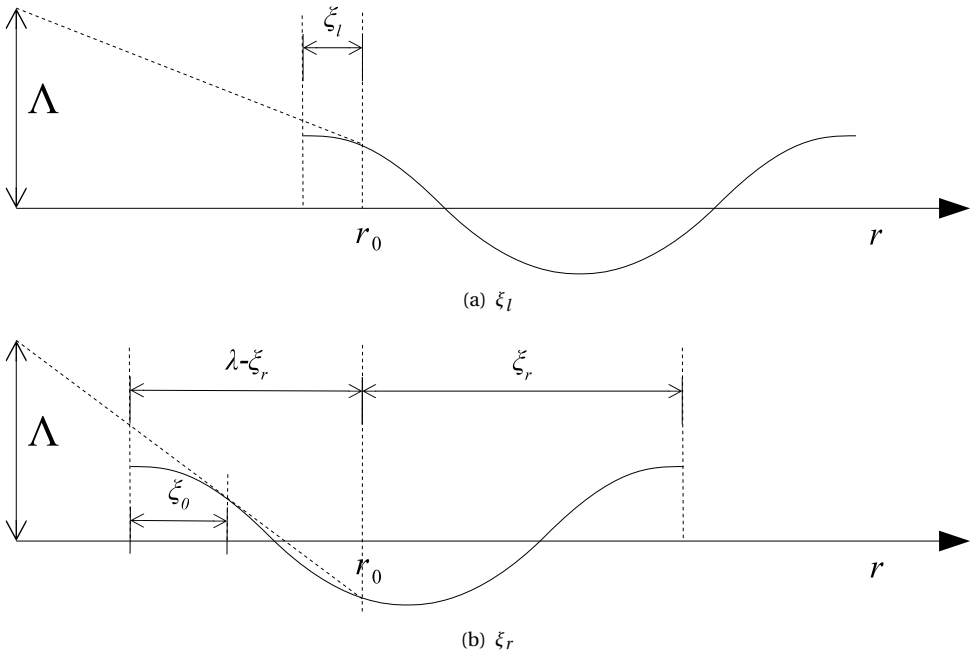


Figure E.1: illustration ξ_l and ξ_r

Shifting the wave profile further to the left, there comes a point, after shifting over length $\xi = \lambda - \xi_r$, where the wave becomes visible again. This will occur when the line of sight towards the surface at r_0 will 'touch' the wave profile at only one point $r = r_0 - \lambda + \xi_r + \xi_0$ where the gradient of the line of sight equals the wave steepness: See figure E.1(b).

This leads to the following two coupled equations for ξ_0 and ξ_r :

$$-k \sin(k\xi_0) = \frac{\cos(k\xi_r) - \cos(k\xi_0)}{\lambda - \xi_r - \xi} \quad (\text{E.3})$$

$$-k \sin(k\xi_0) = \frac{\cos(k\xi_r) - \frac{\Lambda}{Ak}}{r_0} \quad (\text{E.4})$$

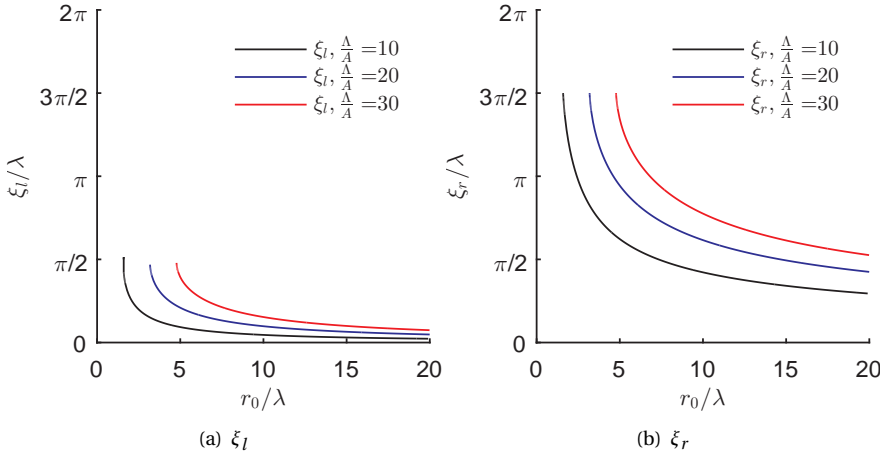


Figure E.2: ξ_l and ξ_r against dimensionless range

Solutions for non-dimensionalized ξ_l and ξ_r are presented against non-dimensional range r_0 in figure E.2 for three different antenna altitude over wave amplitude ratios. Knowing the boundaries of the visible part of the wave profile, the mean and non-dimensional standard deviation over this visible part, $\bar{\eta}_{r,vis}$ and $\sigma_{\eta_r,vis}$ respectively, can be determined:

$$\bar{\eta}_{r,vis} = \frac{1}{\xi_l + \xi_r} \left(\int_0^{\xi_l} (\partial_r \eta) dr + \int_{\lambda - \xi_r}^{\lambda} (\partial_r \eta) dr \right) \quad (\text{E.5})$$

$$\sigma_{\eta_r,vis} = \frac{1}{kA \frac{1}{2} \sqrt{2}} \left(\frac{1}{\xi_l + \xi_r} \left(\int_0^{\xi_l} (\partial_r \eta)^2 dr + \int_{\lambda - \xi_r}^{\lambda} (\partial_r \eta)^2 dr \right) \right)^{0.5} \quad (\text{E.6})$$

(It should be noted that σ is used to indicate standard deviation here, it is not related to its earlier use for (N)RCS.)

In order to consider the effect of shadowing when eliminating the offset of the signal by subtracting a running average (as proposed in eq. 5.6), $\sigma_{\eta_r,vis}^*$ is defined as:

$$\sigma_{\eta_r,vis}^* = \frac{1}{kA\frac{1}{2}\sqrt{2}} \left(\frac{1}{\xi_l + \xi_r} \left(\int_0^{\xi_l} (\partial_r \eta - \bar{\eta}_{r,vis})^2 dr + \int_{\lambda - \xi_r}^{\lambda} (\partial_r \eta - \bar{\eta}_{r,vis})^2 dr \right) \right)^{0.5} \quad (\text{E.7})$$

Figure E.3 presents both $\sigma_{\eta_r,vis}$ and $\sigma_{\eta_r,vis}^*$. The shadowing results in a decrease of $\sigma_{\eta_r,vis}$ with r and this decrease is even more drastic for $\sigma_{\eta_r,vis}^*$. The latter is undesired since it means that correcting for an unknown mean offset of the backscatter, by obtaining this unknown mean offset from the observation and subtracting it from the data (as given by eq. E.7), will finally result in an underestimation of the wave elevation for large r .

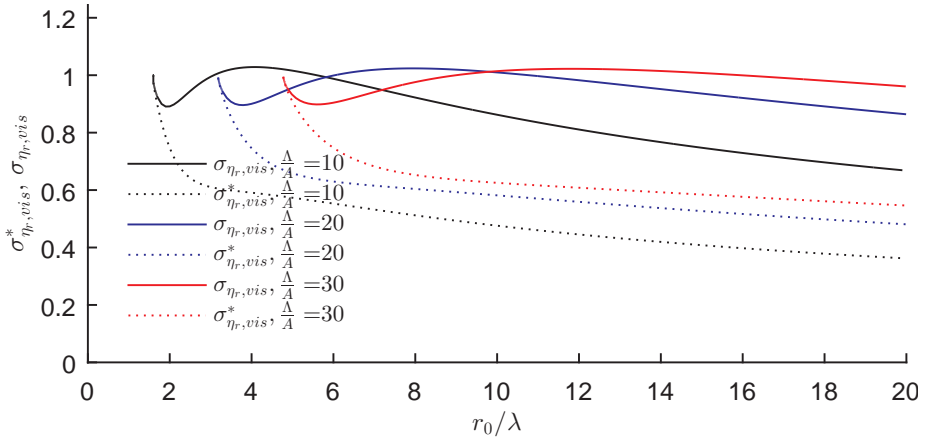


Figure E.3: $\sigma_{\eta_r,vis}$ and $\sigma_{\eta_r,vis}^*$ against dimensionless range

The conclusion from figure E.3 is obvious: shadowing leads to a decreased standard deviation obtained from only the visible part of the observed signal, $\sigma_{\eta_r,vis}$. Correcting the signal for its mean, again determined over its visible part only, will lead to an underestimation of the quantity that we want to derive from the signal (being η_r), an underestimation that increases with increased distance from the antenna.

F

APPENDIX

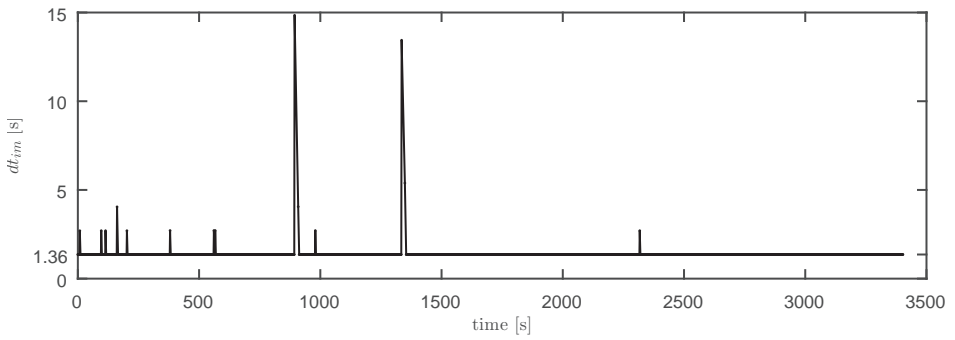
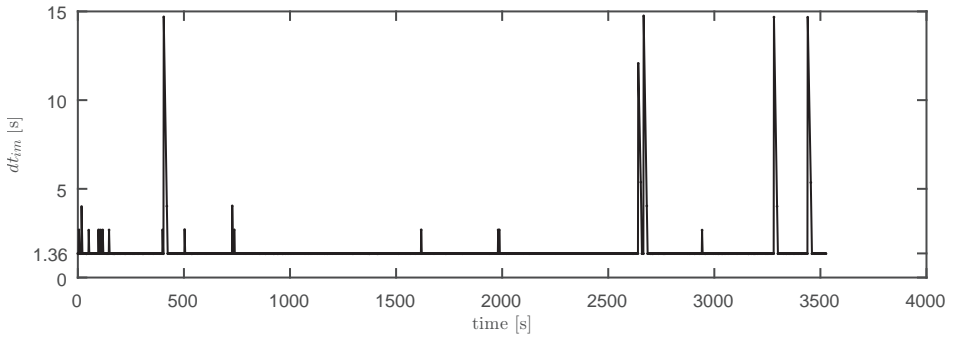
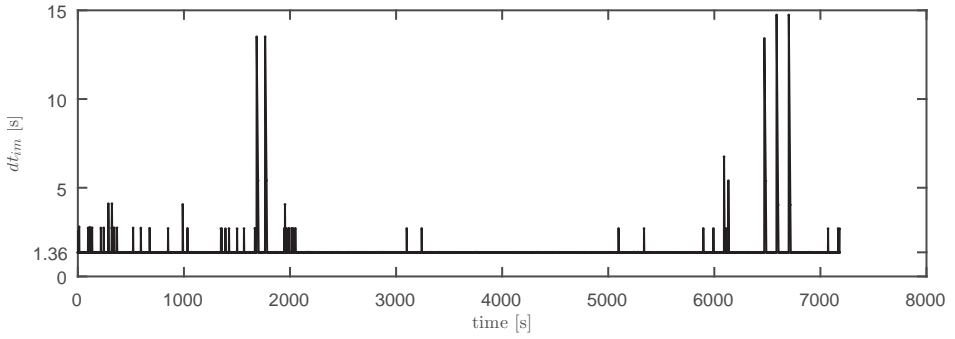


Figure F.1: Subsequent time intervals between acquired radar images

F

G

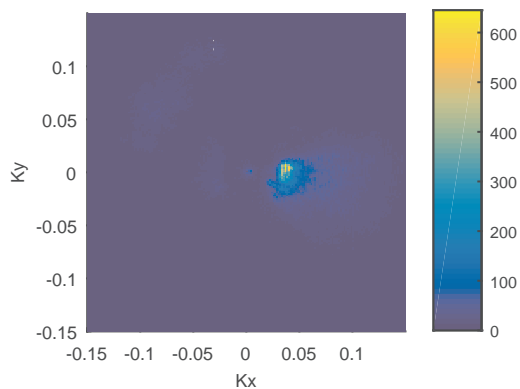
APPENDIX

Output		Orientation performance			
3D orientation (Quaternions/Matrix/Euler angles)					all angles in 3D
3D acceleration					0.05 deg
3D rate-of-turn					<0.5 deg
3D earth-magnetic field (normalized)					<1 deg
Temperature					± deg RMS
Sensor performance		rate of turn	acceleration	magnetic field	temperature
Dimensions		3 axes	3 axes	3 axes	-
Full Scale (standard)		± 300 deg/s	± 17 m/s ²	± 750 mGauss	-55...+125 °C
Linearity		0.1% of FS	0.2% of FS	0.2% of FS	<1% of FS
Bias stability ⁴ (1σ)		5 deg/s	0.02 m/s ²	0.5 mGauss	0.5 °C accuracy
Scale Factor stability ⁴ (1σ)		-	0.05%	0.5%	-
Noise density		0.1 deg/s/√Hz	0.001 m/s ² /√Hz	0.5 mGauss (1σ)	-
Alignment error		0.1 deg	0.1 deg	0.1 deg	-
Bandwidth (standard)		40 Hz	30 Hz	10 Hz	-

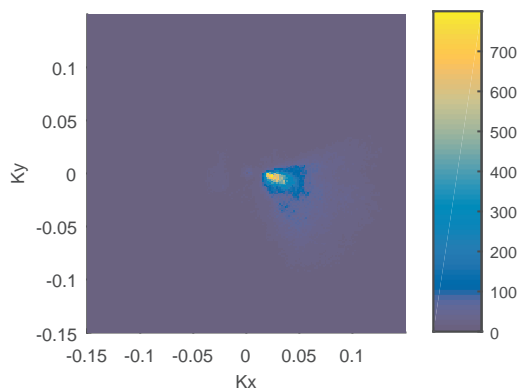
Figure G.1: Specifications of motion sensor Island Frontier

H

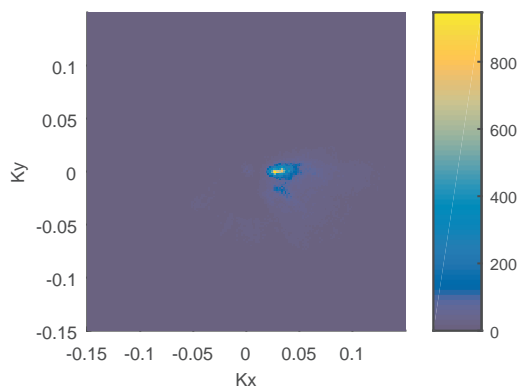
APPENDIX



(a) data set 1



(b) data set 2



(c) data set 3

Figure H.1: Unscaled directional wave spectra obtained by 3D FFT and dispersion filtering

I

APPENDIX

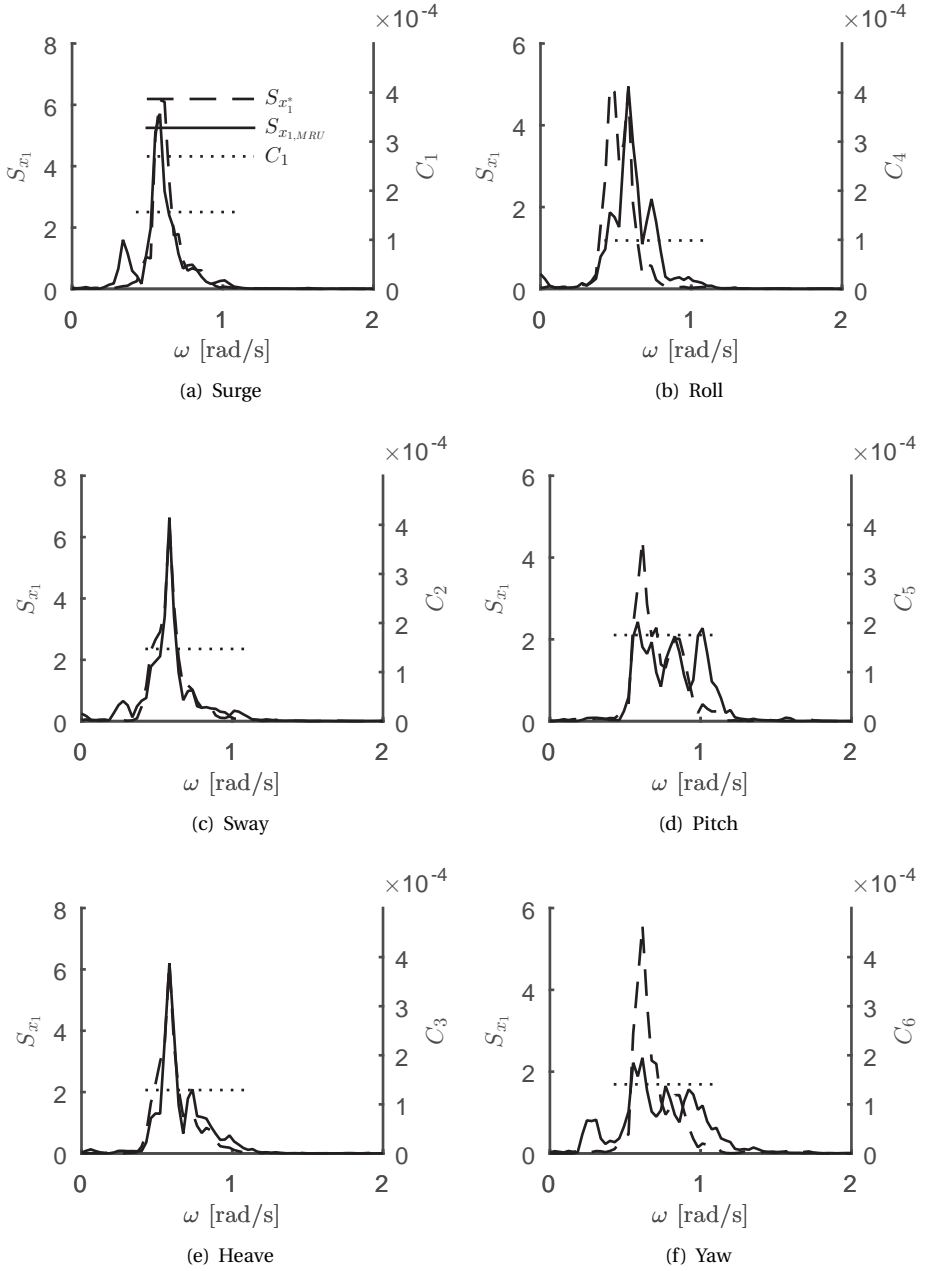


Figure 1.1: Example of 15 minutes spectra of now-cast and MRU measurement (left axes) and scaling factors (right axes), data set 1

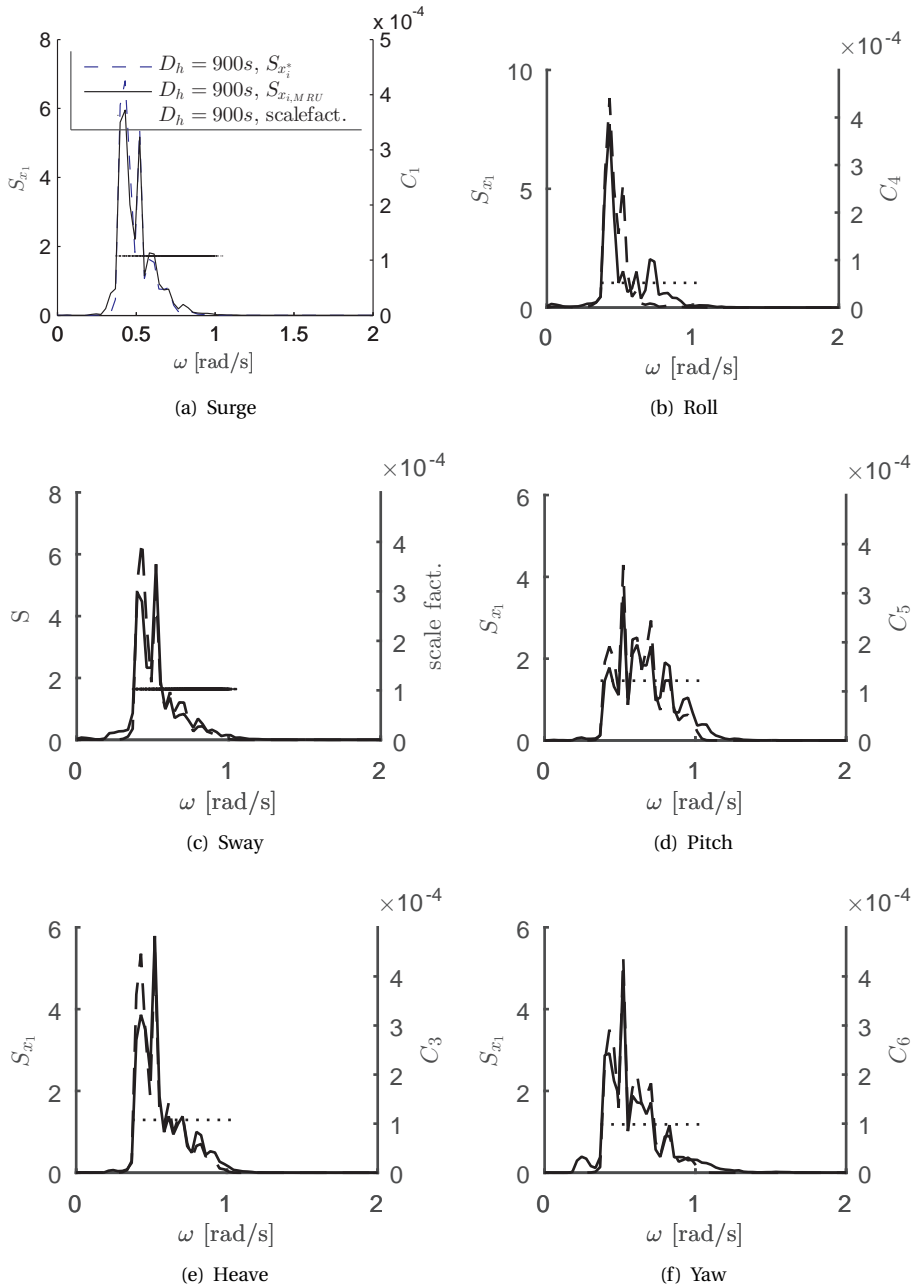


Figure I.2: Example of 15 minutes spectra of now-cast and MRU measurement (left axes) and scaling factors (right axes), data set 2

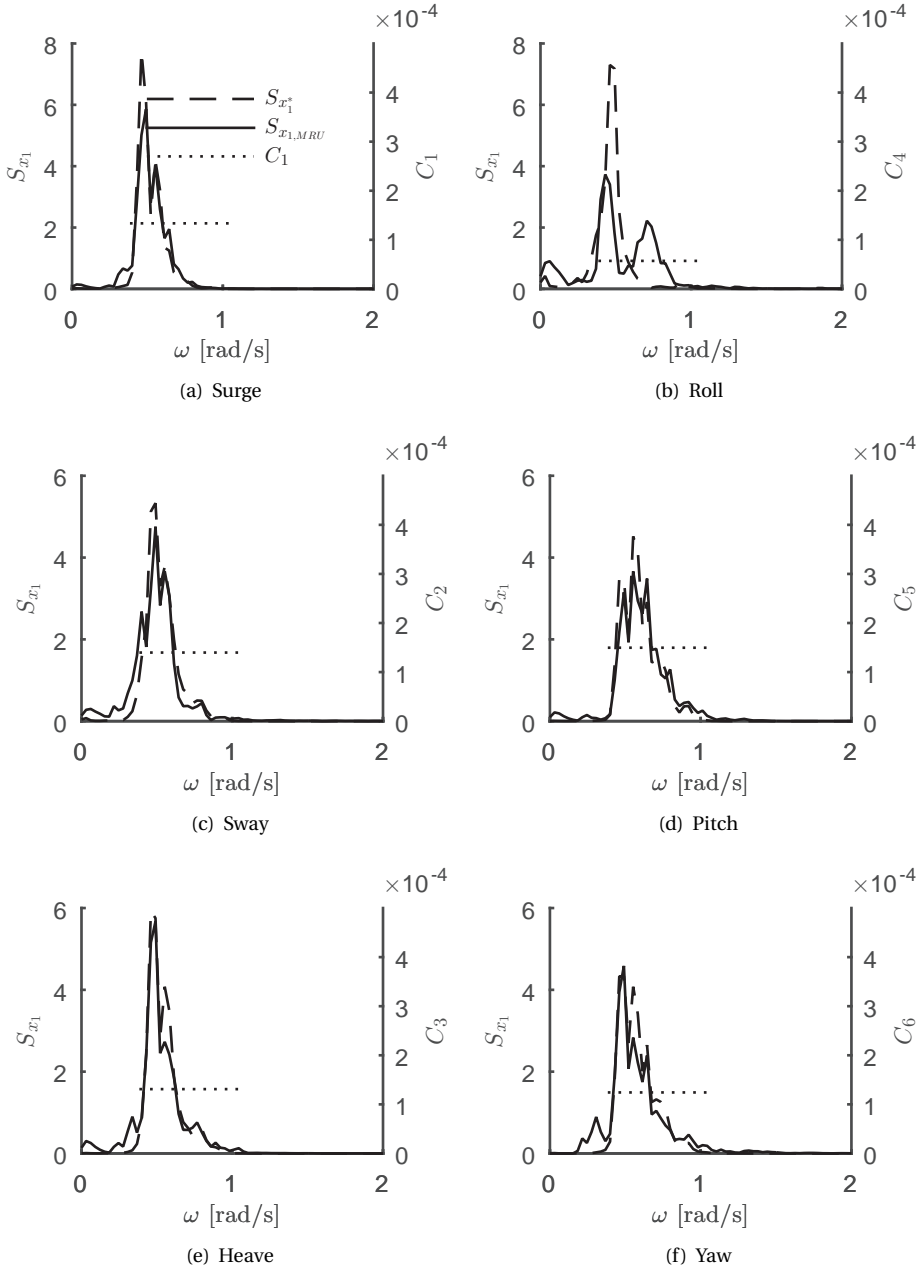


Figure I.3: Example of 15 minutes spectra of now-cast and MRU measurement (left axes) and scaling factors (right axes), data set 3

J

APPENDIX

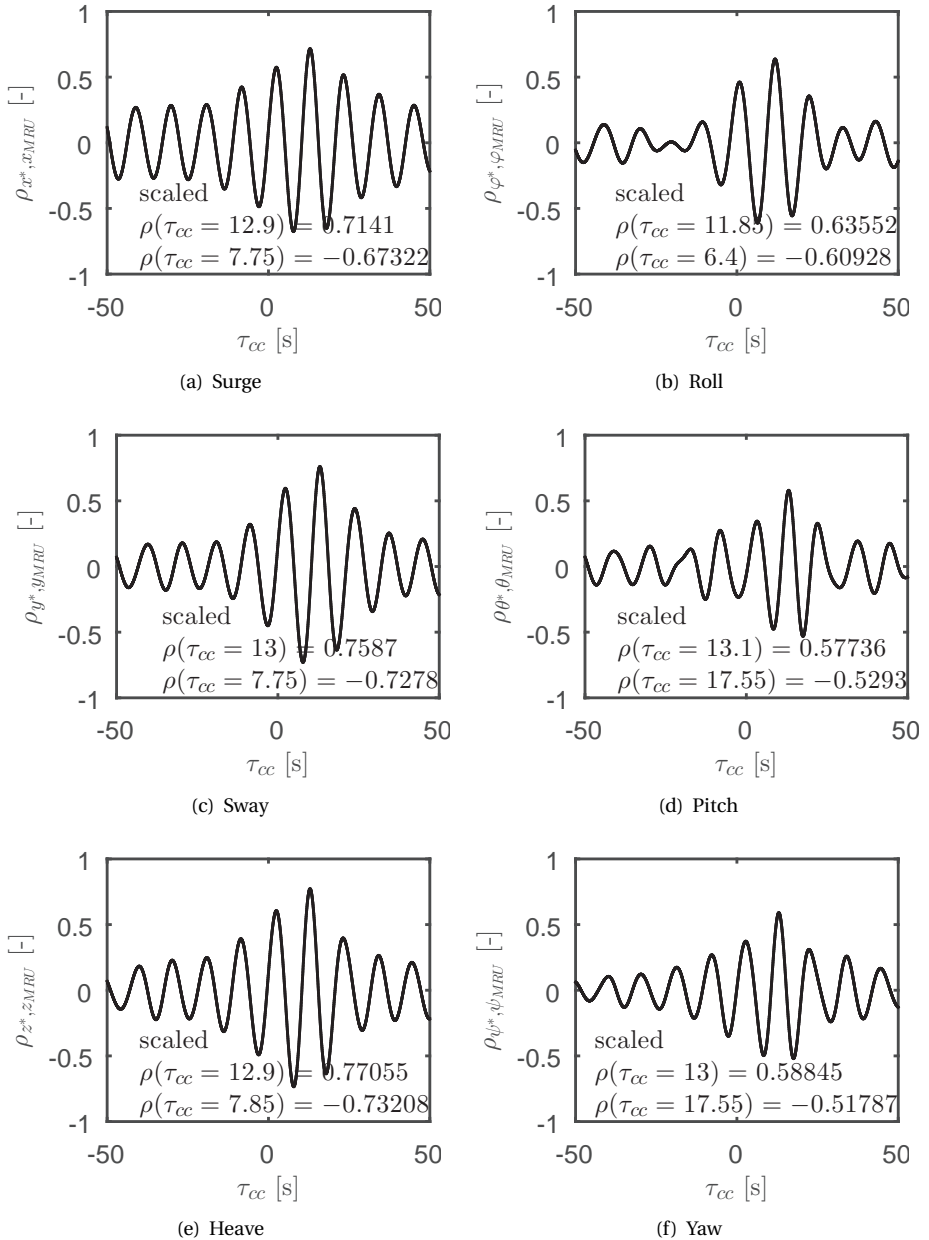


Figure J.1: Cross correlations between motion nowcast and measurement, data set 1 8109

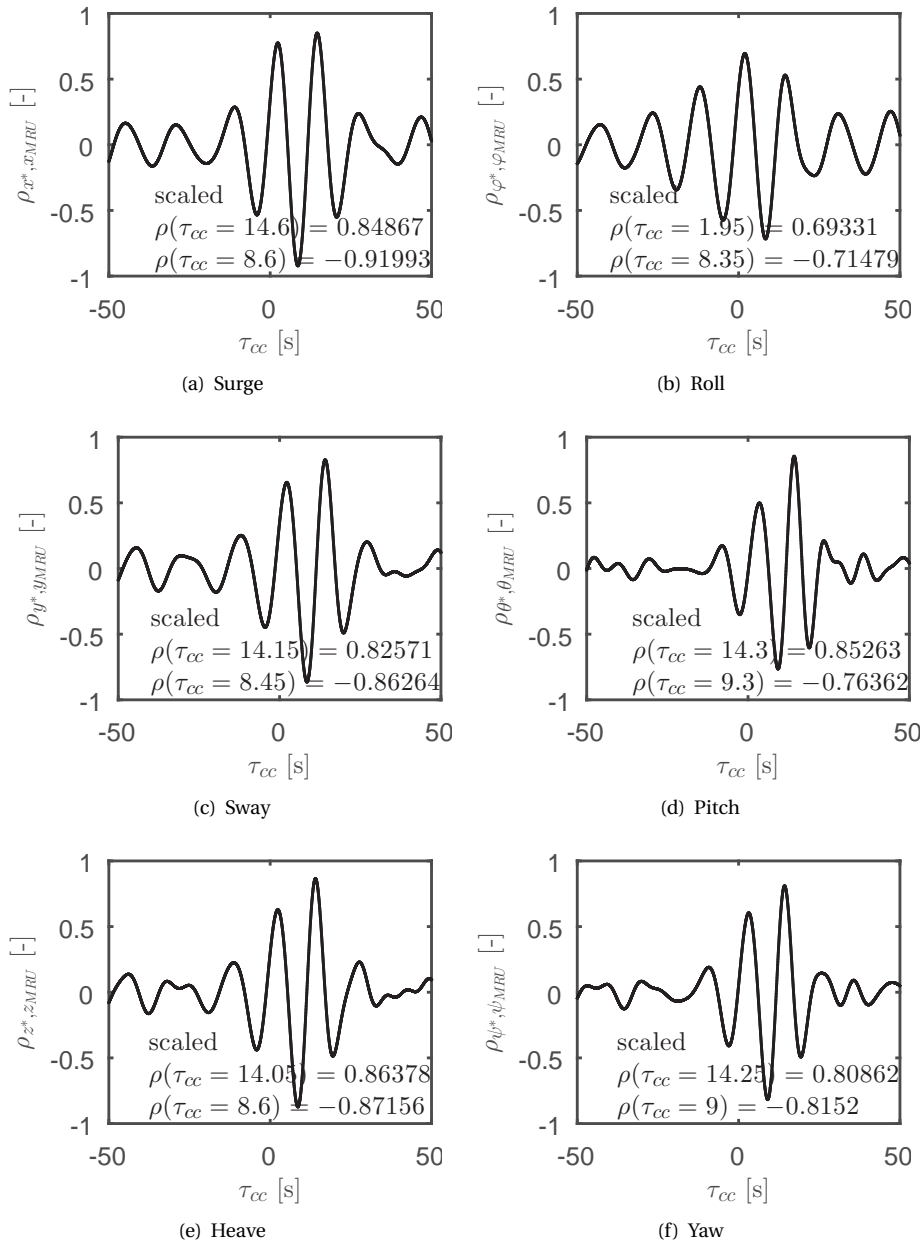


Figure J.2: Cross correlations between motion nowcast and measurement, data set 2 8110

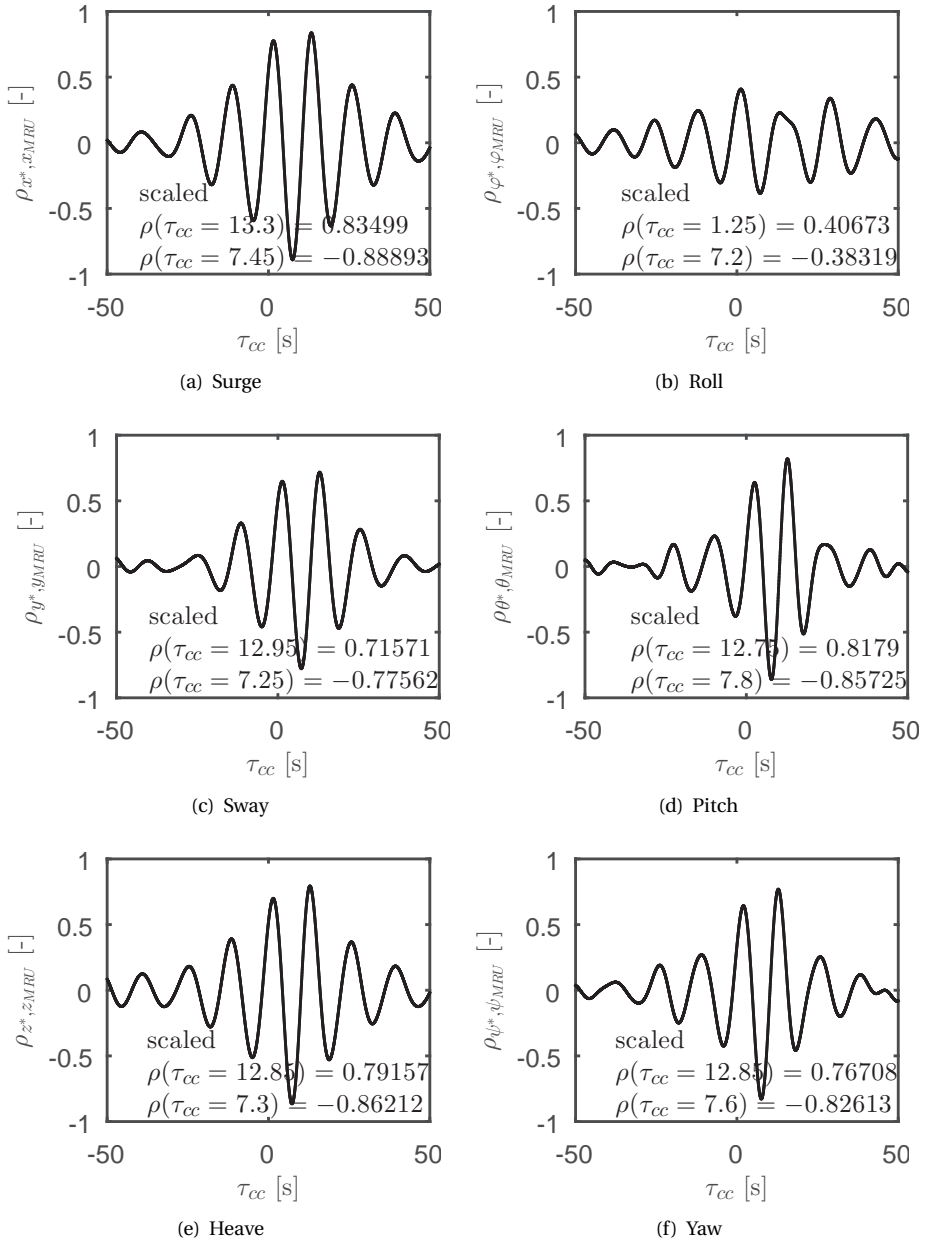


Figure J.3: Cross correlations between motion nowcast and measurement, data set 3 8111

K

APPENDIX

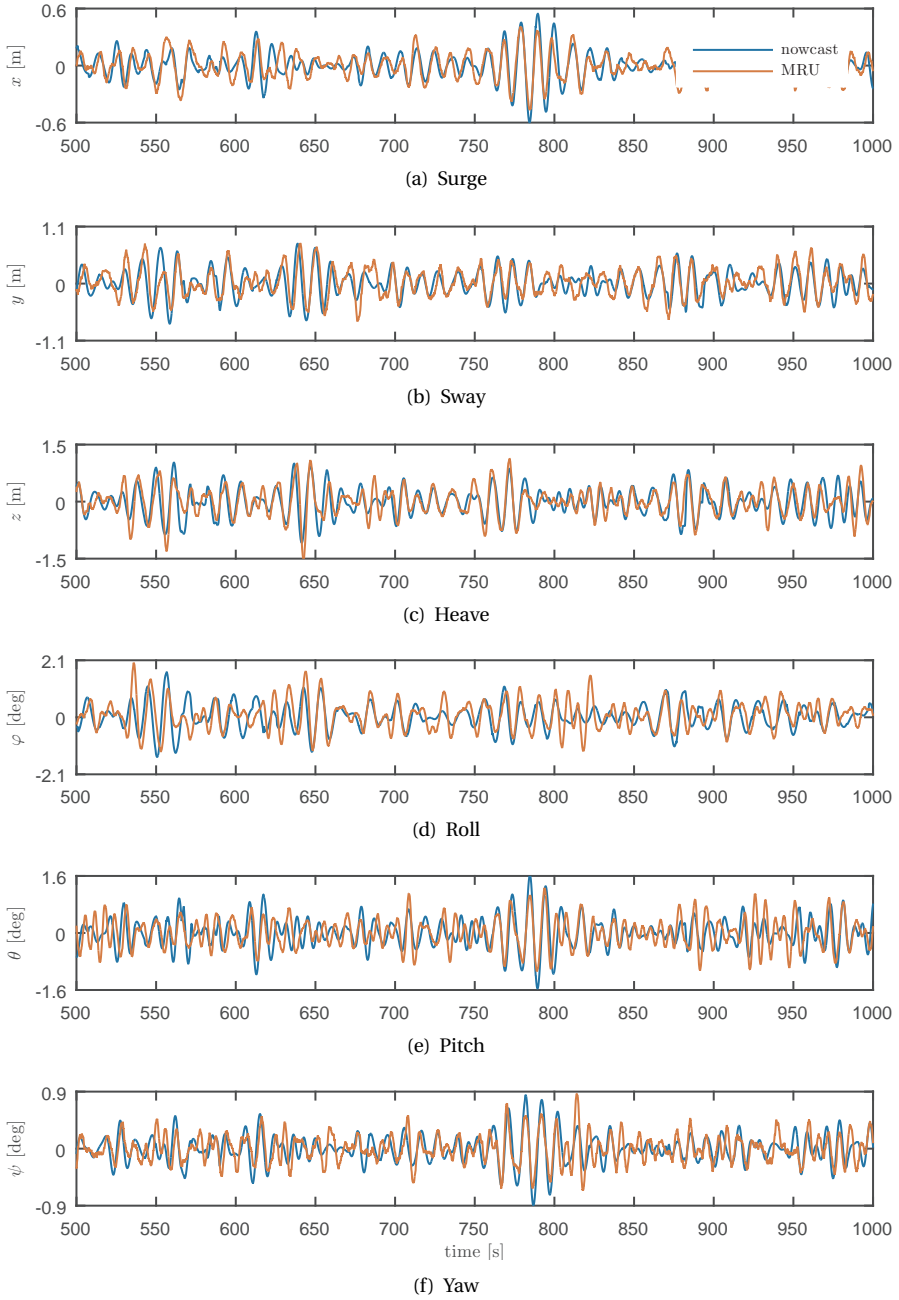


Figure K.1: Sample time traces of motion nowcast, data set 1

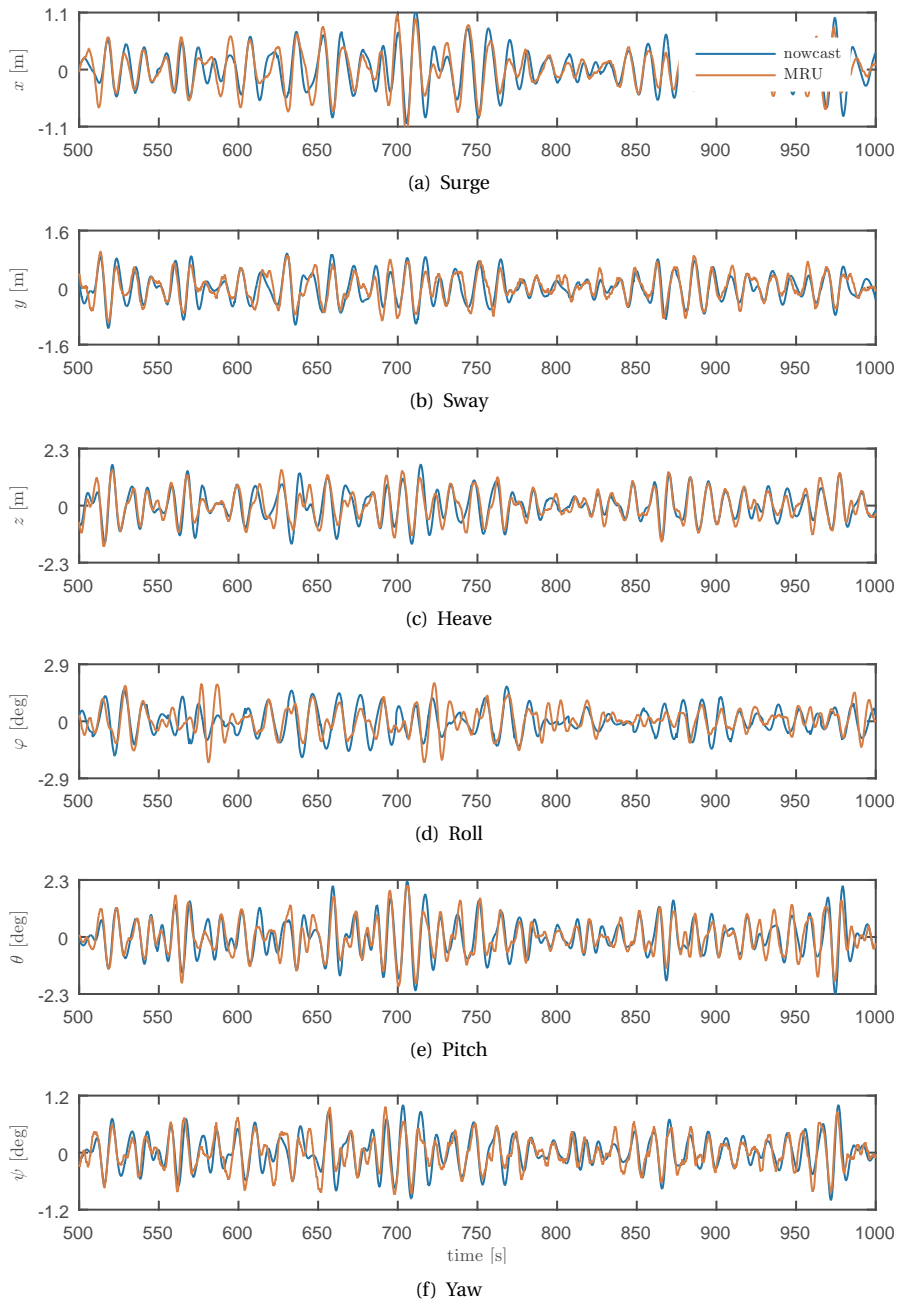


Figure K.2: Sample time traces of motion nowcast, data set 2

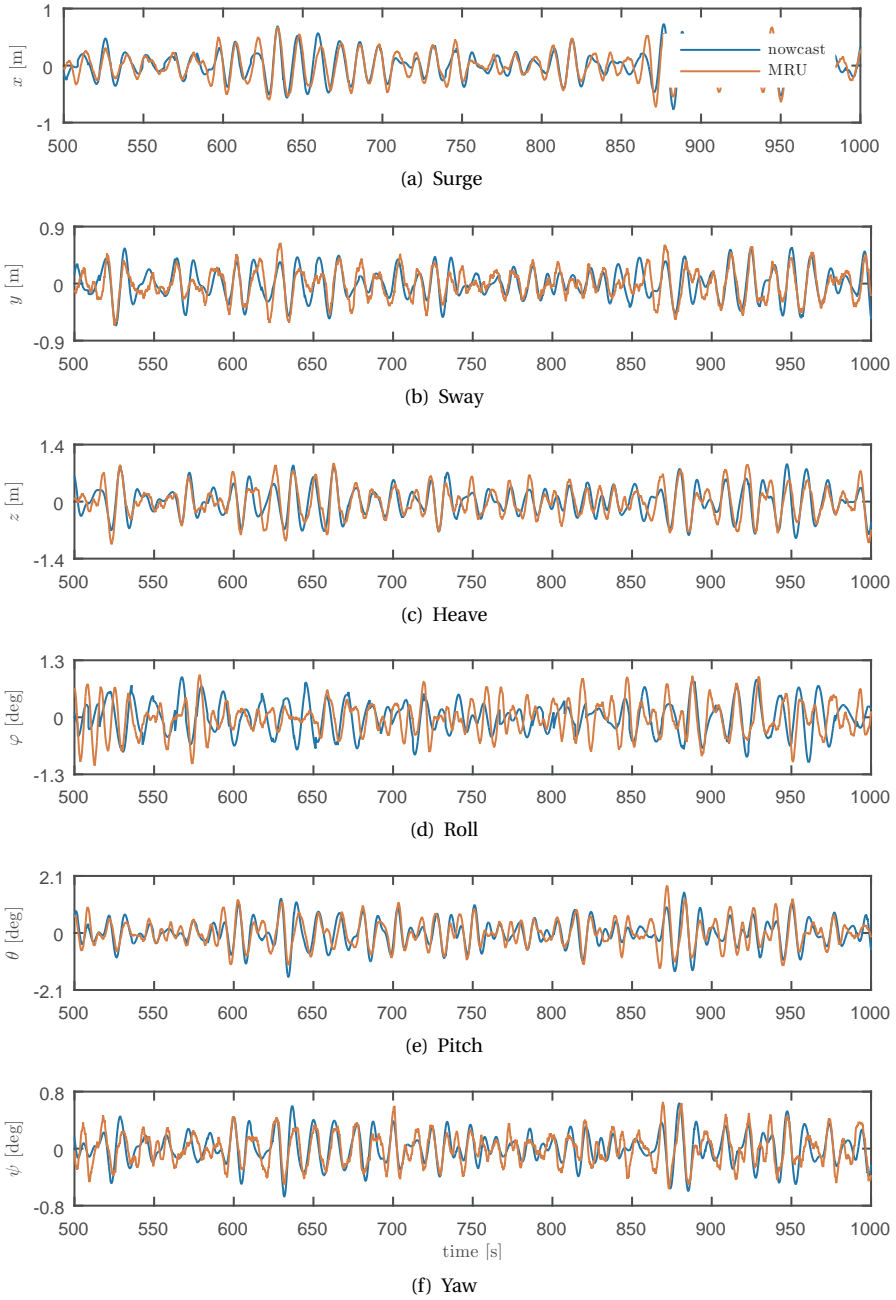


Figure K.3: Sample time traces of motion nowcast, data set 3

L

APPENDIX

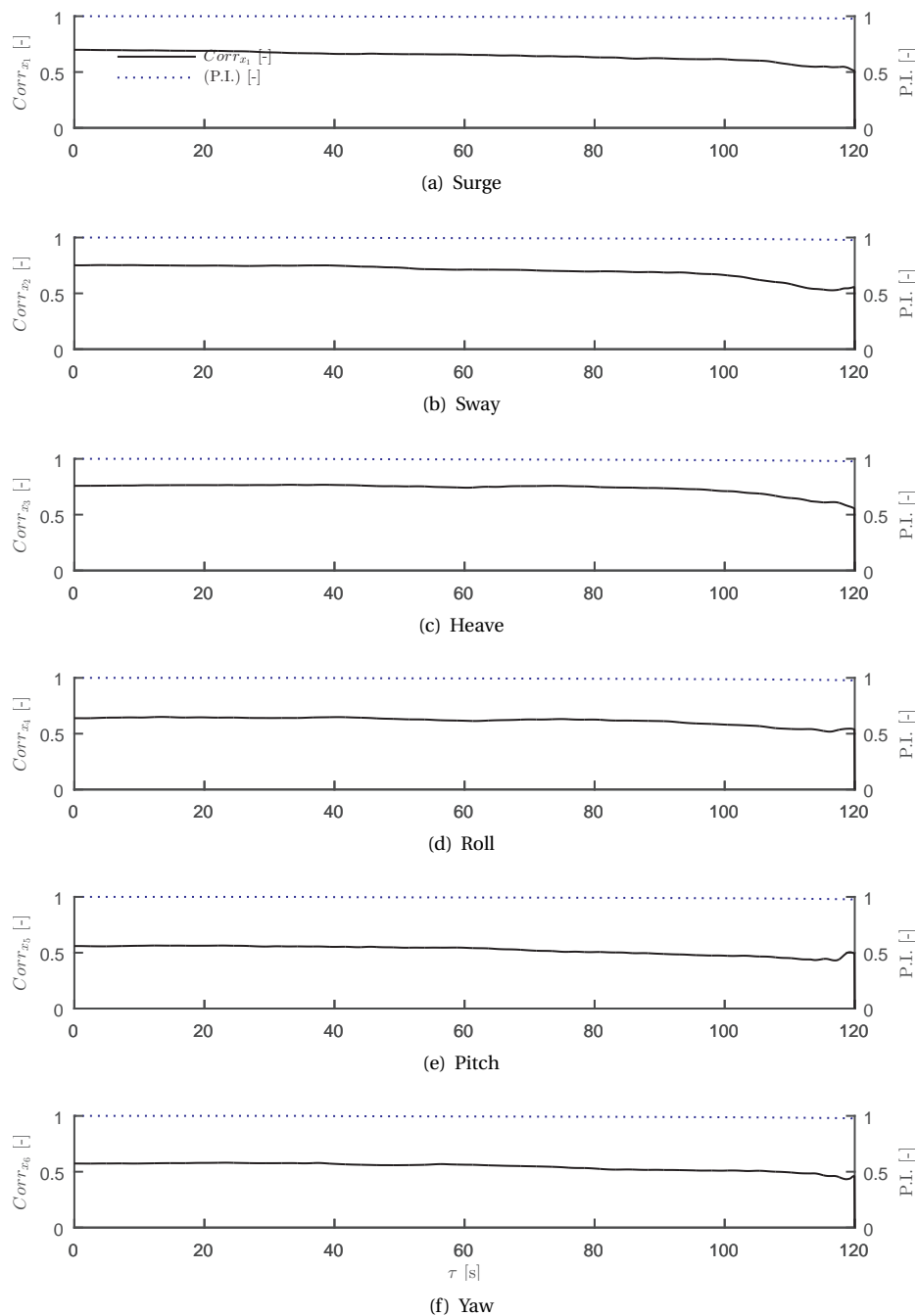


Figure L.1: Prediction correlation data set 1

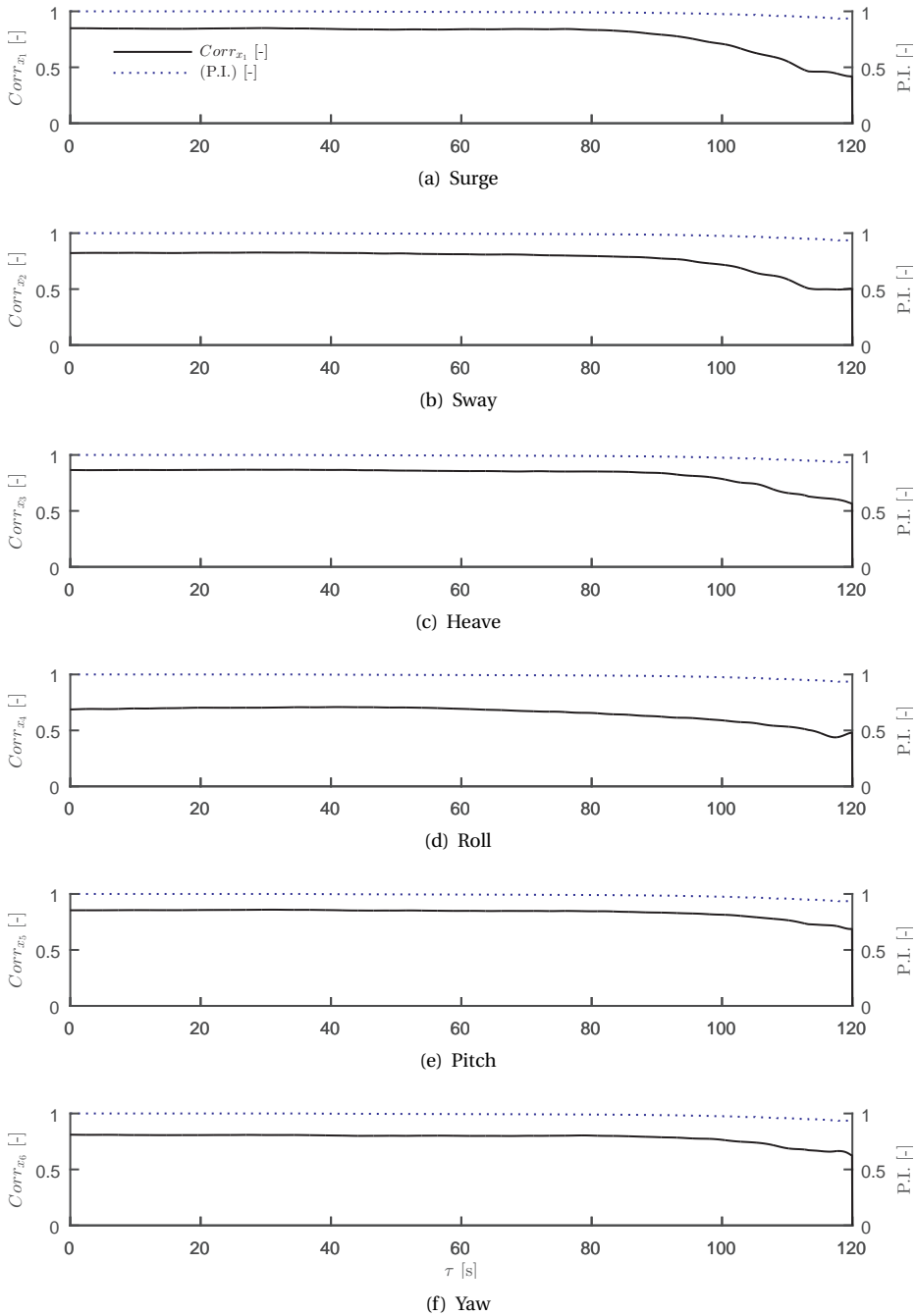


Figure L.2: Prediction correlation data set 2

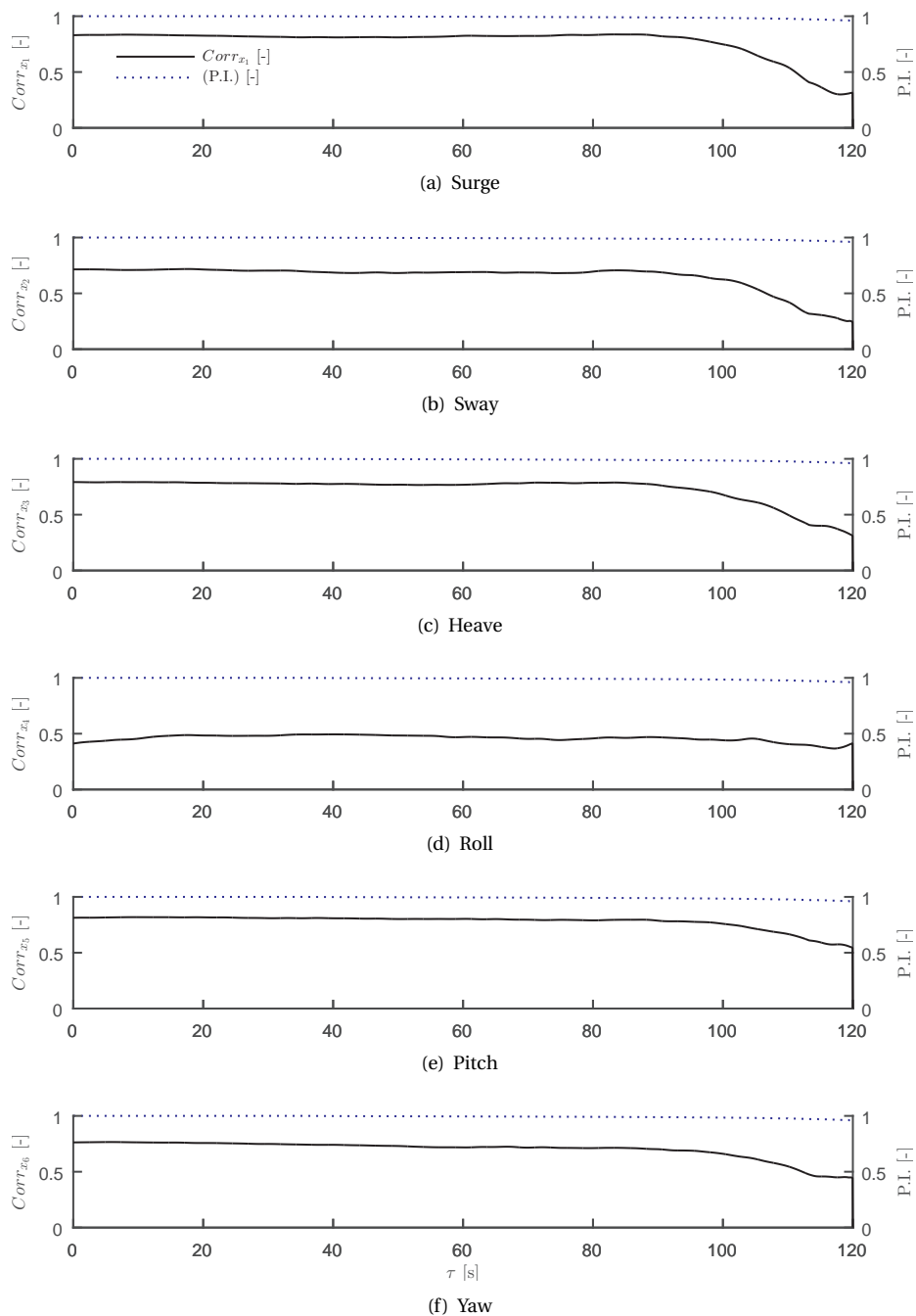


Figure L.3: Prediction correlation data set 3

M

APPENDIX

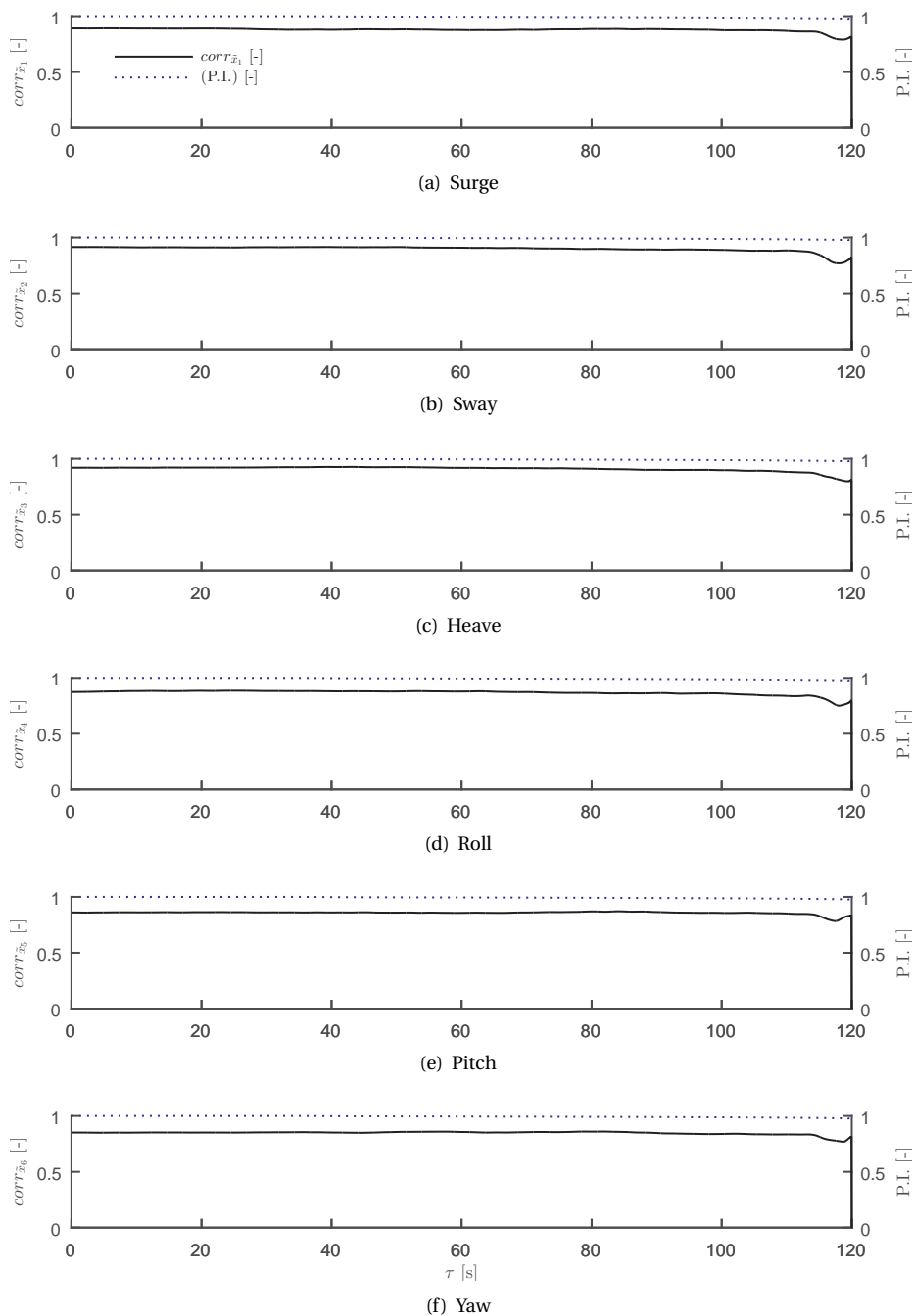


Figure M.1: Envelope prediction correlation data set 1

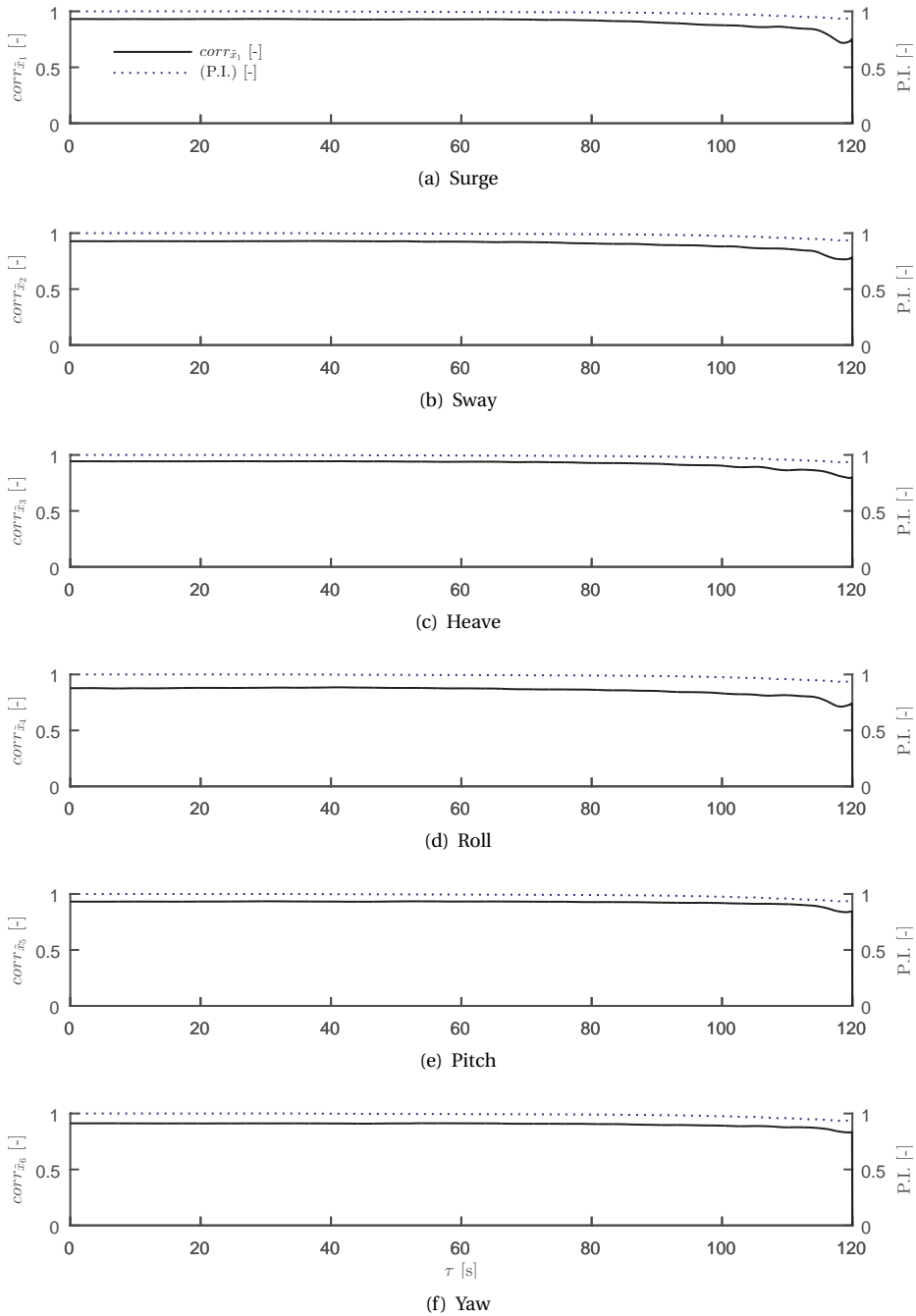


Figure M.2: Envelope prediction correlation data set 2

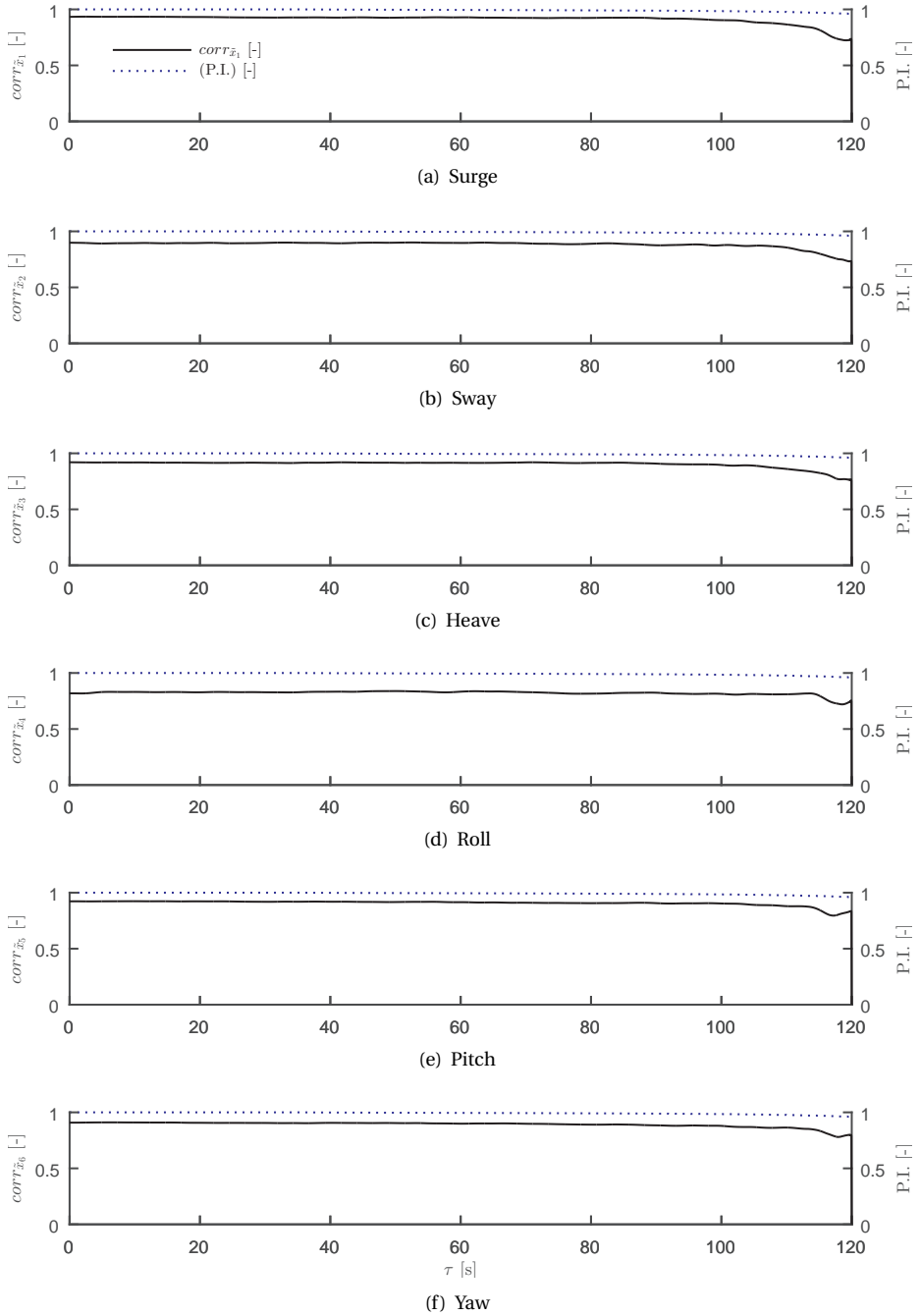


Figure M.3: Envelope prediction correlation data set 3

CURRICULUM VITÆ

Peter NAAIJEN

26-12-1975 Born in Giessen, the Netherlands.

EDUCATION

1994–1998 B.Eng degree in 'Scheepsbouwkunde'
Rotterdam University of Applied Sciences, the Netherlands
Technische Hogeschool Rotterdam (HR&O) , the Netherlands

1998–2002 M.Sc. degree in Maritime Technology
Delft University of Technology

EMPLOYMENT RECORD

2000 Data analyst
MARIN, the Netherlands

2003–present Assistant Professor
Delft University of Technology
Dept. of Maritime and TransportTechnology

2016–present Co-founder
Next Ocean BV

AWARDS

2011 Best Teacher Award of faculty 3ME, Delft University of Technology